Diamond Surfaces: Interactions with Hydrogen and Halogens

Thesis by

M. Susan Melnik

In Partial Fulfillment of the Requirements
for the Degree of
Doctor of Philosophy

California Institute of Technology
Pasadena, California

1997
(Submitted May 21, 1997)

Acknowledgements[1]

Kudos to all my mentors for their incredible dedication to education and science: my co-advisor Prof. William A. Goddard, III, of Caltech, Drs. Satoshi Koizumi and Yoichiro Sato of the National Institute for Research in Inorganic Materials (aka Mukizai-ken) in Japan, Dr. John N. Russell, Jr., of the Naval Research Laboratory (NRL), and Dr. O. Wayne Holland of Oak Ridge National Laboratory (ORNL). I acknowledge my co-advisor Prof. David G. Goodwin for introducing me to the fascinating subject of diamond growth, and I especially thank him for funding my attendance at several conferences. Graduate school is a means to do science and become integrated into the scientific community, and national conferences are absolutely essential to the latter and therefore the former.

I thank the other members of my thesis committee, Profs. Harry A. Atwater and George R. Rossman. I am especially grateful to Prof. Thomas A. Tombrello for his careful reading of the thesis and for asking many tough, good, and fair questions in the thesis exam. TAT, you are an educator in the truest sense of the word. I only wish I had met you sooner in my graduate studies. HAA, thank you for welcoming me into your lab and especially for introducing me to the Materials Research Society. I also thank Prof. Marc-Aulet Nicolet for welcoming me to the pelletron lab and providing me with an office. GRR, thanks for several useful and enjoyable discussions about diamond, IR, and SIMS.

Thanks to all the people who read and critiqued drafts of the thesis: Profs. David G. Goodwin and William A. Goddard, III, Dr. Robert M. Housley, Drs. David B. Poker and David M. Zehner of ORNL, and especially, especially Dr. John N. Russell, Jr., of NRL. JNR, Jr., many thanks for all those hours of telephone conferencing to debug experiments at ORNL and ideas at Caltech.

---

[1] Funding agencies and individuals specific to certain projects are acknowledged at the end of the corresponding chapters and appendices.

I thank the United States and Japanese government laboratories which facilitated the majority of the experiments reported here. Diamond surface science is notoriously expensive and proceeds at a snail's pace relative to silicon without lots of money and spare parts to facilitate it. Except for the handful of universities with enough resources, I believe that government laboratories are the only place to do graduate experiments in diamond surface science. Many diamond theses have benefitted from collaborations with government laboratories, including SLAC, NRL, Lawrence Berkeley, and ORNL, and I heartily recommend them to future students.

I thank Dr. Rodney C. Chin, formerly of Lawrence Berkeley National Laboratory and the University of California at Berkeley, for many useful discussions about each of our diamond projects, and for commiseration through the downside of graduate school. Thanks also to my Caltech officemate, Ms. Ruth Ann Bertsch, and all of the Goddard group for stimulating scientific discussions and mutual support. I could not have done it without you. Thanks to Dr. Dana L. Roth for fielding many questions and providing excellent scientific references.

The production of the manuscript was aided by many friends. Thanks especially to Mrs. Beth Hasler, who became my hands for 3 months when my wrists could no longer stand the strain of typing and grading. Thanks to Ms. Jerri Greene of the Caltech Student Affairs Office for arranging to fund a good deal of her time. Thanks to Mr. Jeremy Kua and Ms. Laurine Tuleja for additional typing. I am grateful to Mr. Gary Holt for many latex and postscript debugging sessions, and for working late into the night to typeset transparencies for the defense. I thank Mr. Glenn C. Smith for technical assistance in producing the central figure of Chapter 3.

Thanks to my undergraduate advisors, Profs. Eli Reshotko and Thomas Eck of Case Western Reserve University, who taught me the love of physics and teaching, and who occaionally served as surrogate advisors in my graduate studies. Although graduate school forced teaching to the back burner, I hope to one day join your ranks at an undergraduate institution. Thanks to Prof. James A. Yorke, of the University of Maryland, for introducing me to the scientific community of nonlinear dynamics and for being the best boss I ever had.

Finally, thanks to God for seeing to it that I never lacked for food, water, and a place to lie my head (though the floor was sometimes harder than I wanted it to be) through even the most dire times of graduate school, and for keeping the government labs open long enough to be there when the experiment needed them. Graduate school did not take anywhere near the course I had originally intended, but God has been there all along and seen me through it. I also thank my parents, Dr. and Mrs. Walter and Martha L. Melnik, for endless encouragement and generous financial support, and the rest of my family for their love.

Abstract

Absolute deuterium coverage on the diamond C(100) surface has been measured under a variety of dosing conditions by nuclear reaction analysis (NRA) using $^{2}D(^{3}He,p)^{4}He$. The (2×1) surface with ~1.0 D per surface C is produced under typical dosing conditions. However, at unusually high filament temperatures *circa* 2000°C, coverages up to 1.34 ± 0.09 D per surface C are observed. Coverage is calibrated by comparing to a standard containing 1.5×10^{18} D/cm^{2}. Signal from subsurface deuterium is estimated to be negligible by comparison to previous scattering experiments and by secondary-ion mass spectroscopy of a homoepitaxial CVD (100) sample. D breakage of surface dimer bonds at high filament temperature is proposed as a mechanism to generate surface dideuterides. The relevance of dimer breakage and dihydride formation to recent experiments on surface degradation is briefly discussed.

Previous models of hydrogen reactions with C(100) are substantially revised to include all types of sites on the reconstructed terrace, and it is shown that saturation coverage determines the ratio of site-averaged abstraction rate to site-averaged recombination rate, k_A/k_R. NRA coverage measurements of 0.95 ± 0.04 D per surface C imply a k_A/k_R of 0.06 ± 0.04 at 1800°C gas temperature and 360°C surface temperature. Results indicate that thermochemical kinetic models overpredict by a factor of ~20 the fraction of sites available for growth during diamond CVD.

In a separate issue, C(110) surface mobility is demonstrated by calculating activation energies for the migrations of H, F, and Cl with quantum chemical methods using hydrocarbon cluster models. The calculations included extensive basis sets with many-body effects at the level of single and double excitations from Hartree-Fock and Complete-Active-Space wavefunctions. Intra-chain migrations of H along $[1\bar{1}0]$ carbon chains and nearest-neighbor F migration are found to be too slow to compete with thermal desorption. However, inter-chain migrations of H and Cl are calculated to be sufficiently fast to compete with thermal desorption under ultrahigh vacuum conditions and with gas-surface reactions under typical diamond growth conditions. This was the first study to consider migration rates as well as barriers, establishing mobility's competitiveness during diamond growth. $D_{[1\bar{1}0]}/D_{[001]}$ is estimated to be $\sim 10^4$. Finally, a kinetic Monte-Carlo algorithm is presented to directly combine mobility with gas-surface reactions in the same iteration step when simulating hydrogen processing of diamond.

Contents

List of Figures

List of Tables

Chapter 1 Introduction

Diamonds have fascinated humans since their discovery near Golconda, India in the 7th Century B.C. The Greco-Romans termed them "adamas," meaning unconquerable, for their ability to withstand blows from a sledgehammer without fracturing.[1] Rarely used as gemstones, and then only by the very wealthy, they often functioned as hard components of cutting and polishing tools, and they were highly valued for their mythical ability to ward off diseases and evil spirits [2]. In the 1870s the diamond market was flooded by the discovery of the prodigious Kimberly mines in South Africa. To preserve the industry, de Beers introduced a centrally-controlled cutting and polishing, sales and distribution system [2, pp. 202–205], and they developed an entirely new market through campaigns to sell diamonds to the masses in the form of jewelry and engagement rings [3].

Recently diamond has attracted a great deal of attention because its unique material properties make it an excellent candidate for high-technology commercial applications such as heat sinks, wear-resistant and low-friction coatings, and electron emitters for flat-panel displays. As a semiconductor with one of the least number of electrons, diamond is also an excellent candidate for theoretical investigations of surface chemistry relavant to low-pressure growth. Despite the commercial and theoretical importance of diamond, very little is currently understood about two of the reactions central to its processing and chemistry: hydrogen recombination with and abstraction from the diamond surface,

$$\mathrm{H}\cdot^{\mathrm{gas}} + \mathrm{C}\cdot^{\mathrm{surf}} \xrightarrow{k_R} \mathrm{C{-}H}^{\mathrm{surf}} + \mathrm{h}\nu_{\mathrm{phonon}} \tag{1.1}$$

$$\mathrm{H}\cdot^{\mathrm{gas}} + \mathrm{C{-}H}^{\mathrm{surf}} \underset{k_{-A}}{\overset{k_A}{\rightleftharpoons}} \mathrm{C}\cdot^{\mathrm{surf}} + \mathrm{H}_2^{\mathrm{gas}}, \tag{1.2}$$

---

[1] Pliny the Elder wrote that the best way to test diamonds is "upon an anvil, and they are so recalcitrant to blows that an iron hammer head may split in two and even the anvil itself be unseated. Indeed the hardness of *adamas* is indescribable." [1]

where $\mathrm{C}\cdot^{\mathrm{surf}}$ represents a radical surface site and $\mathrm{C{-}H}^{\mathrm{surf}}$ represents a hydrogenated surface site.[2]

These reactions determine key parameters in low-pressure diamond growth [4, 5], surface science [6, 7, 8], and tribology [9]. In diamond chemical-vapor deposition (CVD), reactions between the surface and gas-phase atomic hydrogen determine the number of surface sites available for growth.[3] In diamond surface science, the hydrogen coverage determines the number of surface sites available for reconstruction. In tribology, hydrogen recombination with reactive radical sites reduces friction and wear on sliding surfaces [10]. Nevertheless, there is very little data on the rates of these hydrogen reactions with diamond. Diamond growth modelers have found it necessary to estimate gas-surface reaction rates from the data of analogous gas-phase reactions [11]. The lack of rate data limits the accuracy of the growth models as well the understanding of surface reconstruction and wear processes.

Rate data is also quite scarce in the case of adsorbate diffusion on diamond surfaces. Although diffusion plays a key role in determining surface structure in silicon growth, before 1990 diffusion had not been considered possible on diamond [12]. Some studies considered only the activation *barriers* to migrations [12] and growth reactions [13, 14, 15] and often concluded that migrations were negligibly slow due

---

[2] Reactions 1.1 and 1.2 are highly simplified models and do not account for the many types of sites present on a typical diamond surface. Chapter 3 analyzes the (100) surface in detail and shows that these simplified models yield the abstraction and recombination rate constants averaged over all types of surface sites present.

[3] The number of radical surface sites is determined by the rate equations for reactions 1.1 and 1.2.

$$\frac{d[\mathrm{C{-}H}^{\mathrm{surf}}]}{dt} = k_R[\mathrm{C}\cdot^{\mathrm{surf}}][\mathrm{H}\cdot^{\mathrm{gas}}] - k_A[\mathrm{C{-}H}^{\mathrm{surf}}][\mathrm{H}\cdot^{\mathrm{gas}}]. \tag{1.3}$$

In steady state this reduces to $[\mathrm{C{-}H}^{\mathrm{surf}}] = \frac{k_R}{k_A}[\mathrm{C}\cdot^{\mathrm{surf}}]$. For $[\mathrm{C}\cdot^{\mathrm{surf}}] = 1 - [\mathrm{C{-}H}^{\mathrm{surf}}]$ (once again neglecting other types of surface sites; see chapter 3 for a more thorough analysis),

$$[\mathrm{C{-}H}^{\mathrm{surf}}] = \frac{1}{\frac{k_A}{k_R} + 1}. \tag{1.4}$$

Therefore the abstraction and recombination rates determine the coverage of surface radical sites available for growth.

to their high barriers. The study described in chapter 3 [16, 17, 18] compared the migration *rates* to gas-surface reaction rates and was instrumental in demonstrating the competitiveness of diffusion on diamond surfaces.

The present research focuses on understanding diamond surface processes, such as diffusion and hydrogen abstraction, at a microscopic level. Diamond surface science is fundamental to this investigation, and a broad overview of it is presented in section 1.1. The relevance of this investigation to diamond CVD is briefly discussed at several points in the text, and a short introduction to CVD is presented in section 1.2. Finally, section 1.3 gives an overview of the thesis.

1.1 Diamond Surface Science

1.1.1 Structure of the three major faces

The diamond surface is typically formed by cleaving the crystal and then polishing with diamond grit in an olive oil lubricant. On (110) and (111) the dangling bonds produced by cutting the bulk crystal are typically saturated by hydrogen which presumably derives from the olive oil. However, complete saturation is not possible on the (100) surface because the diamond lattice is too tight, i.e., the hydrogen nuclei on neighboring carbon centers would be less than 1 Å apart. Therefore the surface reconstucts to the (2×1):H structure shown in fig. 1.1 [19]. A (3×1) reconstruction is also possible on the (100) surface [20] but has never been observed experimentally. The (111) surface desorbs hydrogen upon heating to about 1000°C and reconstructs to the (2×1) structure [21, 22]. The (100) [23, 24, 25] and (110) [26, 27] surfaces also desorb hydrogen upon heating but no major reconstructions occur.[4]

The foregoing picture is highly oversimplified. In reality, some freshly-polished samples reconstruct upon heating, while as many as 40% do not [21, 24]. Clean, smooth samples are difficult to produce reliably, and reconstruction is sensitive to

---

[4] One group [26] has reported the appearance of faint half-order LEED spots upon heating the (110) surface to 1227°C. This indicates a partial (2×1) reconstruction. The half-order spots were removed by adsorption of approximately 0.1 H per surface C.

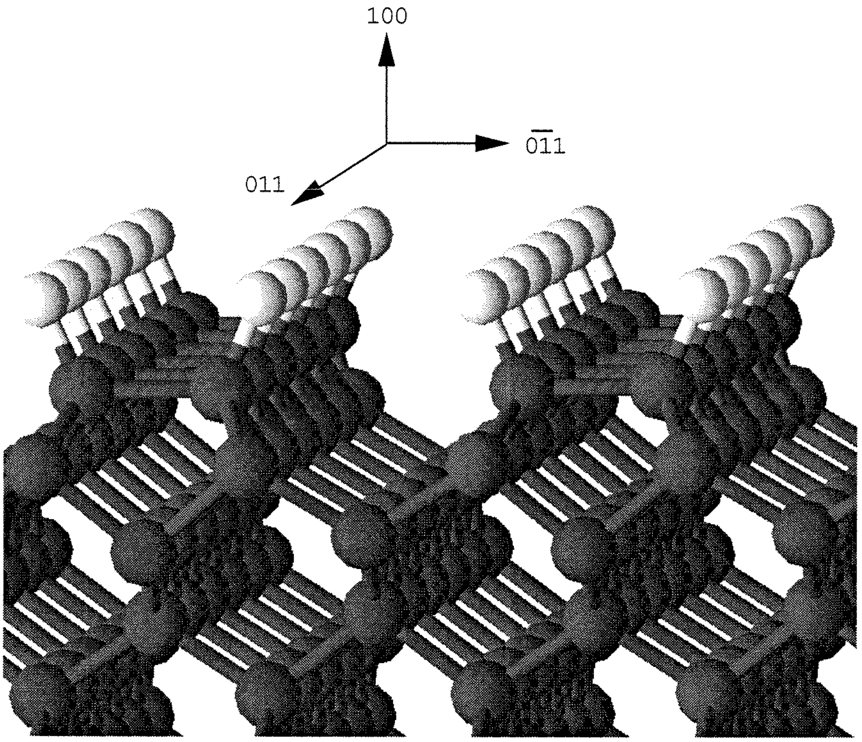

(a) 2 × 1 reconstruction of C(100).

Figure 1.1: Atomic-scale geometry of the diamond (100) (2×1) surface. The large grey spheres represent carbon centers, and the small white spheres represent hydrogen centers. The arrows indicate the crystallographic directions.

surface roughness as well as to small amounts of contamination from the polishing process or the vacuum chamber. Oxygen contamination has been associated with the inability of a (100) surface to reconstruct [24], and exposure to atomic oxygen has been found to destroy the (2×1) LEED pattern on the (100) surface [23]. The mechanism by which oxygen interferes with reconstruction is unknown; however, adsorption of oxygen at a bridge site affects the adjacent surface dimer [28]. Even when parts of the sample are locally reconstructed, oxygenated sites might possibly interfere with long-range reconstruction by allowing uncorrelated surface domains. If the resulting domain size were less than 100 Å, then the local reconstruction would not be detectable by LEED [29].

Surface	A (s^{-1})	E_d (kcal/mol)	Order	Method	Ref.
(100)	10^{13} [a]	72.7	1	TPD	[23]
	10^{13} [a]	79.5	1	TPD	[30]
	10^{13} [a]	71	1	TPD[b]	[31]
	3×10^5	37	1	TPD	[24, 25]
(110)	10^{13} [a]	75	1	TPD[b]	[27]
	$5 \times 10^{13\pm1}$	95 ± 5	1	TPD	[26]
(111)	10^{13} [a]	78	1	TPD[b]	[32]
	$10^{15\pm2}$	92 ± 9	1.3 ± 0.3	SFG	[33]
polycrystalline	$10^{10.5\pm0.9}$	69 ± 6	1	TOF-SARS	[7, 34]
	5×10^7	51	1	TPD[b,c]	[35]

[a] The prefactor was assumed to be 10^{13} s^{-1}.

[b] D_2 desorption from a D-terminated surface.

[c] In addition to D_2, HD and H_2 desorption resulted from background hydrogen present during deuterium exposure. All three species gave the same desorption parameters.

Table 1.1: Kinetic parameters for thermal desorption of hydrogen from various diamond surfaces. TPD is temperature-programmed desorption, SFG is the surface-spectroscopic technique of sum-frequency generation, and TOF-SARS is time-of-flight scattering and recoil-ion spectroscopy.

1.1.2 Thermal desorption

On the three major faces, adsorbed hydrogen desorbs as molecular hydrogen upon heating to ~1000°C in vacuum. The rate of thermal desorption is first order in surface coverage, i.e.,

$$\frac{d\theta_H}{dt} = -A \exp^{-E_d/kT} \theta_H^n, \tag{1.5}$$

where $n = 1$ for first-order desorption and θ_H is the areal density of surface hydrogen. The values for activation barrier, E_d, and the pre-exponential factor, A, vary from experiment to experiment and are summarized in table 1.1.

Although thermal desorption spectra often show a single peak characteristic of a single desorption mode, some spectra exhibit an additional peak at lower temperature [27, 30, 31, 32]. The first peak is attributed to desorption from adjacent monohydride sites. On silicon surfaces the second peak is attributed to the presence of dihydride sites, with a desorption barrier lower than that of monohydrides. In some diamond cases, the second peak does not appear until a series of exposures to several times the amount of H necessary to saturate the surface. Both a mechanical polishing during sample preparation and a slow etching by atomic hydrogen during dosing can cause surface roughness, leading to dihydrides. Therefore surface degradation may generate dihydrides, causing a second thermal desorption peak to develop. All data reported in table 1.1, except that of refs. [30] and [32], were based on spectra with single desorption peaks.

1.1.3 Atomic hydrogen exposure: surface reconstruction and degradation

Exposure to gas-phase atomic hydrogen changes the reconstruction of the (111) surface. Chemisorption of ~0.05 D per surface C onto a bare (111) surface starts to rapidly transform the surface from (2×1) to (1×1) [22, 33], presumably by unzipping the π-bonded chains. The (2×1) reconstruction is restored by thermally desorbing the deuterium upon heating the sample to 1420 K in vacuum. Subsequent exposure to atomic D returns the surface to a (1×1) state. These adsorption-induced phase transitions have been studied by thermal desorption spectroscopy (TDS), X-ray photoemission spectroscopy (XPS), Auger electron spectroscopy (AES), second-harmonic generation (SHG) and LEED [22, 33, 36], and by sum-frequency generation (SFG) [33, 36].

Some experiments have found that cycling the diamond surface through a series of atomic hydrogen exposures followed by desorption (thermal annealing) degrades the sharpness of the (2×1) LEED pattern [21, 24]. However, other experiments found the (2×1) pattern to be completely reproducible when the sample was heated during dosing to 800–850°C [33] or 500°C [36]. Degradation might be caused by surface roughness. Since mechanical polishing likely produces a rougher surface than plasma treatment, Hoffman *et al.* [31] compared polished surfaces to plasma-treated ones. They found that polished C(100) degrades upon cyclic deuterium adsorption and desorption, even for doses performed at surface temperatures up to 800°C. However, no degradation is reported for C(100) samples prepared by hydrogen-plasma treatment [19, 31], even when the sample temperature was as low as 27°C during dosing. The ability of heating during dosing to prevent degradation in some cases, and its inability in other cases, might also be explained by surface roughness. The experiments which found no surface degradation when the sample was heated during dosing [33, 36] were performed on polished C(111), whereas experiments which found surface heating unable to prevent degradation were performed on polished C(100). As a cleavage plane, polished C(111) is likely to be smoother than polished C(100).

Surface roughness has also been proposed to explain the need for ~1000°C annealing to produce the (2×1) LEED pattern on polished surfaces [19]. Whereas plasma-treated C(100) exhibits a sharp (2×1) LEED pattern [19] upon insertion into the vacuum chamber, mechanically-polished samples give a (1×1) pattern [23, 37, 38, 39], though sometimes only after heating to 400–500°C [21, 24]. The (2×1) pattern does not emerge until annealing to 800°C [23], 1200°C [39] or 1227°C [24].

The (1×1) LEED pattern also degrades upon cyclic H exposure and desorption, again possibly due to the roughness of mechanically polished surfaces. Hamza *et al.* [24] found that exposing the polished C(100) surface to large doses of atomic hydrogen at -93°C destroyed even the (1×1) pattern. Although the (1×1) pattern was later restored by annealing to 427°C, heating to 1227°C did not produce a fully reconstructed surface. The (1×1) LEED pattern further degraded upon successive cycling through thermal desorption and atomic hydrogen exposure, necessitating periodic repolishing of the sample.

In some experiments, surface degradation causes a second peak to appear in thermal desorption spectra, possibly by generating dihydride sites, as discussed in section 1.1.2.

In summary, surface degradation is a complex, poorly-understood process. Surface roughness, as caused by mechanical polishing or adsorption-desorption cycling below T_s of 500°C, appears to be a prerequisite for degradation. Cycling the surface above a temperature of 500°C causes negligible degradation, possibly due to self-healing of local roughness by surface migration [40]. The physical mechanism for degradation has yet to be identified, but may involve local graphitization, slow etching of the surface by atomic or molecular hydrogen, or rupture of surface C-C bonds. Carbon-carbon bond breakage is likely a slow process initiated by β-scission through H abstraction [11, 41], or C-C bond breakage may be catalyzed by contamination originating from the atomic hydrogen source [Chapter 2].

1.1.4 Molecular hydrogen exposure

Molecular hydrogen does not dissociatively chemisorb on either bare or hydrogenated diamond surfaces below 400°C [21, 23, 27, 33, 42, 43]. However, hydrogenated diamond powders become fully deuterated after one hour of exposure to D_2 at 700°C [43]. Since the experiment reported in chapter 2 saw desorption above 450°C, desorption may preceed deuteration. If desorption activates the reaction, then holding the surface temperature below 450°C would preclude diamond from reacting with gas-phase D_2. Above 840°C, mass spectroscopic analysis gives evidence for the evolution of small quantities of CD_4 from deuterated diamond [43]. This may indicate local reconstruction of the diamond surface followed by graphitization and subsequent etching by D_2 at elevated temperatures. Annealing of diamond powders above 900°C causes local graphitization, as detected by Raman spectroscopy [44], and heating CH_x-covered C(111) to 1200°C converts part of the CH_x into graphitic carbon, as detected by AES [22]. However, any graphitization is limited below 860°C, as the weight gained by the powders (determined by thermogravimetric analysis) is exactly what would be expected from replacing the surface hydrogens with deuterium [43]. Therefore, any graphitization and subsequent vaporization to CD_4 would be below the detection limit of the gravimetric instrument [43].

1.1.5 Experimental technique

Diamond surface science experiments are limited by the difficulty in preparing reliably clean surfaces [6, 21]. Over the years samples have been prepared by a variety of methods, including polishing with diamond grit lubricated by olive oil, boiling in acids to remove metal contaminants, and ultrasonic rinsing in solvents to remove hydrocarbons. Plasma treatment has arisen as one of the most reliable ways to clean diamond. The hydrogen plasma smooths the (100) surface and causes it to reconstruct to (2x1):H [45], a surface which remains stable even in air. During experiments physisorbed contaminants are eliminated by heating, and surface cleanliness is typically checked via XPS or HREELS. Auger spectroscopy is minimized to avoid surface damage or degradation [31].

Diamond experiments are also challenged by the difficulty in accurate temperature measurement. The emissivity of clear, polished diamond is typically much lower than that of the sample holder material. Therefore, pyrometers measure the temperature of the sample holder, usually rough molybdenum or tantalum, rather than the diamond itself. Since thermocouples do this job just as well without requiring line-of-sight access or viewport corrections, the majority of diamond surface science experiments measure temperature by attaching a thermocouple to the sample holder. However, thermocouples clamped to sample holders can be greater than the actual diamond temperature by as much as 150°C [19] to 200°C [46]. The best accuracy is obtained by positioning the thermocouple inside of a hole laser-drilled into the side of the sample [46]. The graphitized surface of the hole radiates as a black-body, producing good thermal contact, and diamond's high thermal conductivity assures a uniform sample temperature.

One might question why issues such as reliable sample preparation and reproducible results, problems long since solved in the silicon field [47], remain central to diamond experiments. Diamond differs fundamentally from silicon in that it graphitizes upon damage or heating, transforming the sp^3 bonds into sp^2 hybridization. Therefore, a process commonly used to clean silicon surfaces, sputtering and annealing, destroys diamond surfaces [37, 38]. Moreover, the high-pressure process used to grow diamond commercially produces crystals of a much smaller size and higher defect density than the float-zone method of growing silicon crystals. Therefore, the results of diamond experiments are much more sample-dependent than those of silicon.

The extreme physical properties that make diamond an attractive material commercially also make it difficult to investigate scientifically. As the hardest natural material in the world, diamond is difficult to cut and polish smooth crystal faces. As one of the widest-bandgap semiconductors, it is difficult to probe with charged particles. Most surface analysis techniques utilize charged beams, and sample charging becomes a significant problem when one moves from silicon to diamond. Moreover, as a semiconductor which forms one of the strongest bonds with hydrogen and cannot be sputter-cleaned, diamond must be heated to at least 1000°C in vacuum to desorb the surface hydrogen. At such an extreme temperature most materials have intolerably high vapor pressures, and the materials available to fabricate ultrahigh vacuum components for diamond are severely limited compared to those for sputter-cleaned silicon. Diamond sample holders typically consist of molybdenum, which is easier to machine than tungsten and which outgasses orders of magnitude less hydrogen than does tantalum [25]. However, molybdenum is itself difficult to machine, and square corners and intricate grooves must be cut electrochemically to avoid chipping.[5] The myriad of unusual challenges faced by diamond surface experiments makes them more rare and less reproducible than those of silicon.

1.1.6 Rate parameters and dynamics of reactions with H(D)

Since molecular hydrogen has been found to be unreactive with diamond at room temperature [21, 23, 48], reaction rates are typically investigated using atomic hydrogen. Atomic hydrogen is commonly produced by passing H_2 over a hot tungsten filament. The tungsten catalyzes the cracking of H_2 and desorbs atomic hydrogen equilibrated to the temperature of the tungsten, typically 0.1 to 0.2 eV. To minimize tungsten transfer to the sample, hot tungsten capillary sources are shielded by a cooled copper block [49]. Hyperthermal hydrogen has also been produced in the case of silicon experiments by laser photolysis of a pulsed free-jet expansion of HI [50]. However, the interaction of hyperthermal beams with diamond surfaces has yet to be investigated.

---

[5] Moreover, sample manipulator parts which are standard in stainless steel are either unavailable or custom in molybdenum. For example, the sample holder of chapter 2 was electrochemically machined from molybdenum plate and was clamped together with threaded rod and nuts, molybdenum screws being rarely available commercially and prohibitively expensive.

In theory, once atomic hydrogen has been formed, the sticking probability on the various crystal faces can be measured. However, the difficulty in calibrating H flux has thus far prevented this from being accomplished. For a hot tungsten filament source,[6] H flux calibration requires an elaborate differentially-pumped mass spectrometer with careful analysis of a modulated hydrogen beam to account for entrapment of radicals on the vacuum chamber walls [55, 56].

Even though absolute sticking or recombination rates have not been measured, reaction-rate *ratios* may be measured. Two particularly important reactions are hydrogen abstraction from and recombination with the diamond surface. The ratio of the rates of these two reactions, k_A/k_R, determines the fraction of surface sites available for growth during CVD. Two groups have measured k_A/k_R, one by high-resolution electron energy-loss spectroscopy (HREELS) [8] and time-of-flight scattering and recoil spectroscopy (TOF–SARS) [7], and the other by sum-frequency generation (SFG) [33]. The SFG results are inconsistent with the others, and all three disagree with a value commonly used in diamond growth models [11]. Due to the dearth of gas-surface reaction-rate data, diamond growth modelers extract their rates from analogous gas-phase reactions [11, 57]. However, surface reactions differ from gas-phase reactions due to the presence of surface phonons and the strain of the underlying lattice. The models approximate surface effects by taking the high-pressure limit of gas-phase rate constants, and the inconsistencies between the model rate constants and the experimental rate constants may have been due in part to this approximation. Nevertheless, this does not explain the differences between the HREELS and SFG results, and further experiments are necessary to resolve the inconsistencies.

Measuring the reaction rate for a range of gas-phase and surface temperatures

---

[6] Langmuir presents quite an elegant analysis of the degree of dissociation of molecular hydrogen by a hot tungsten filament [51]. However, due to the vacuum practice at the time [52], the initial rates of dissociation he obtained may have been affected by oxygen contamination [53]. Brennan and Fletcher [54] investigated the effect of oxygen contamination and extended the work to cleaner vacuum. They found that on clean W filaments the measured rate of atomization was consistent with atomic and molecular hydrogen desorbing from the W surface in their equilibrium ratio. The equilibrium constant is determined by the temperature of the filament and the pressure of the molecular hydrogen.

gives information about the mechanism by which hydrogen reacts with the diamond surface. It has recently been suggested that hydrogen reacts with diamond via a generalized Eley-Rideal (ER) mechanism [8]. In contrast to the Langmuir-Hinshelwood mechanism, where the reactants fully accomodate to the surface before reacting, in the ER mechanism the gas-phase reactant does not equilibrate with the surface. Instead the incident H provides the energy for surmounting the activation barrier, and the reaction rate depends on the temperature of the incident H rather than on the temperature of the surface. Each diamond experiment to date has investigated only a single gas-phase temperature and the types of samples (single vs. poly-crystalline) have varied across experiments. A single experiment investigating a range of gas-phase and surface temperatures on the same sample would strengthen the evidence for the ER mechanism.

The dynamics of hydrogen reactions with diamonds have yet to be investigated. In the ER mechanism, the majority of the reaction energy is deposited into molecular excitations of the gas-phase products rather than into the surface. For example, in the abstraction of H(D) on D(H)/Cu(111), which has recently been shown to be an ER reaction [58], approximately all of the available reaction energy is deposited into the HD product in the form of translational, vibrational, and rotational excitation. H abstraction of hydrogen and halogens from Si(100) has also been proposed to proceed via a generalized ER mechanism [59, 60], and the lack of sample heating by this process makes it an attractive candidate for low sample-temperature cleaning of semiconductor surfaces [59].

In summary, issues surrounding rate parameters and dynamics of diamond surface reactions with atomic hydrogen have yet to be resolved. A single experiment investigating a range of gas-phase temperatures would resolve inconsistencies in previous rate measurements. Future experiments could extend the data to include abstraction barriers and dynamic effects by investigating reaction rates over a wide range of incident atomic hydrogen energies, from thermal energies relevant to hot-filament CVD to hyperthermal energies relevant to plasma-enhanced deposition [61]. Results will be vital to the development of accurate computer models of surface processing and low-pressure diamond growth as well as to the development of theoretical understanding of radical-surface reaction dynamics.

1.2 Diamond Growth Experiments

Attempts to grow diamonds artificially date back to the early 1800s. In 1796, Smithson Tennant, building on the research of Sir Isaac Newton and Antoine-Laurent Lavoisier, discovered that diamonds consisted of the same material as charcoal (carbon) [62]. Growth methods then focused on hydrocarbon feedstocks. Early workers tried a variety of methods to grow diamond including crystallizing it out of carbon-rich aqueous solutions [63][7] and producing electrical discharges across carbonaceous materials [65, 66]. In the 1870s researchers realized that diamonds were made in volcanoes[8] and created various types of ovens and explosions to mimic their high-temperature, high-pressure conditions. This yielded large quantities of soot and some small stones rumored to be diamond [2]. The technology at the time did not allow high pressures to be sustained for long enough to grow significant amounts of diamond, and before the advent of Raman spectroscopy it was difficult to establish growth by distinguishing between polycrystalline diamond and amorphous carbon. Researchers refined their growth technique and in the 1950s developed a method to produce diamond at high pressure using Fe or Ni as a catalyst [67].

Attempts to grow diamond from low-pressure reacting gases began as early as 1911, when J. W. Hershey experimented with an oxy-acetylene blowtorch [68]. Although his attempts were unsuccessful, in 1988 researchers succeeded in growing diamond films from blow torches [69, 70].

---

[7] Due to the lack of high-pressure conditions, it is unlikely that the few crystals produced in 1828 [63] actually consisted of diamond. Recently, Zhao *et al.* [64] succeeded in growing diamond from seed crystals in a solution of nickel and glassy carbon in water. However, their growth occured at 1.4 kbar and 800°C, vastly higher pressures and temperatures than the atmospheric conditions used in 1828.

[8] Before the 1860s, diamonds were panned from rivers or found scattered on beaches. Water had washed these diamonds from their sources, volcanic ducts, so long ago that the sources were no longer evident. In the 1860s, the first primary source of diamonds, the Kimberly mines in South Africa, were discovered, and researchers realized that diamonds were made in volcanoes. [2, p. 199]

In the 1960s, Eversole [71] patented a method to grow diamond at low pressure and high temperature by passing methyl-containing gas over diamond powder at ~1000°C. Under these conditions black carbon grew along with diamond, and Eversole found it necessary to interrupt the growth periodically and clean off the amorphous carbon by heating the powder in hydrogen gas at about 50 atmospheres. In the past two decades researchers have combined the cleaning and growth steps by diluting the hydrocarbon gas in H_2 [4, 72, 73, 74]. To eliminate the need for high pressure, the gas is activated by cracking hydrogen over a hot tungsten filament [75] or in a microwave plasma discharge [76]. The atomic hydrogen in turn activates the hydrocarbon gas and the growing surface by abstracting hydrogen from them to produce radical sites. Methyl radicals in the gas grow the diamond by recombining with surface radical sites [4, 11, 57]. A series of abstractions and rearrangements subsequently bond the methyl carbon to the other carbons in the diamond lattice. Similar reaction mechanisms have been proposed for diamond growth from acetylene [77, 78].

In low-pressure CVD reactors, feedgas composition is typically 1% methane or acetylene and 99% hydrogen. Higher methane fractions give rougher growth surfaces [79] and codeposition of amorphous carbon. Diborane and phosphine have also been included in the feedgas at the ppm level to p- or n-dope the diamond either for electronic applications or to simply increase the conductivity to allow ex-situ SEM observation [80]. However, n-doping has not yet been reported to be sucessful. Substrate temperature is typically 700–1000°C during growth. Reducing the substrate temperature from 700°C to 400°C decreases the growth rate from 0.1 μm/hr to 0.006 μm/hr [81].

1.2.1 Experimental challenges

In-situ growth monitoring is difficult; high temperature and atomic hydrogen are not particularly welcoming to many probe materials. Non-intrusive optical techniques such as REMPI [82] have been the most successful at gaining information about the gas-phase growth environment. The gas composition at the growing surface has been measured quite elegantly, by drilling into the substrate an entrance hole to a molecular-beam mass spectrometer [83]. McMaster *et al.* have built upon this technique to measure the gas-phase concentrations of H, CH_3, CH_4 and C_2H_2 in MWCVD [84] and HFCVD [85] reactors.

One of the challenges in growth experiments is temperature measurement. The diamond temperature is usually measured by optical pyrometers or thermocouples. There is a temperature gradient over the substrate, and quoted growth temperatures are often averages over the substrate area, in the case of pyrometric measurement, or the thermocouple locations, in the case of thermocouple measurement.[9] Thermocouple measurements are complicated by thermal gradients between the sample and junction. Gradients can be minimized by inserting the junction directly into a hole drilled in the diamond [46]. However, typical diamond samples are too small to contain holes for thermocouple junctions, and thermocouples are usually located on the sample holder. Optical pyrometric measurements are complicated by diamond's low emissivity. The emissivity is so low that most of the radiative flux impinging on the pyrometer originates from the material directly behind the substrate. Typically the emissivity of the sample holder is assumed to be constant, neglecting the variation with temperature, chemical state and roughness of the surface.

In practice temperatures are measured to ensure repeatable results between growth runs rather than to identify the exact surface temperature. For example, in Kamo-type reactors there is no temperature control independent of the plasma, and the microwave power and cavity length are adjusted during the run to produce the desired temperature. This is an important point to keep in mind when comparing theoretical predictions to experimental data.

Measurement questions aside, growth experiments are time-consuming. Unlike silicon, where huge market forces have reduced sample preparation to a fine art, diamond sample preparation is generally done by "cut and try." Moreover, investigating the effect of growth conditions on growth rate or film quality requires a large num-

---

[9] For example, in MWCVD experiments performed by the author at the National Institute for Research in Inorganic Materials, temperatures typically varied by 30°C over the area of the 6 mm×6 mm substrate. Temperatures were measured pyrometrically assuming a constant emissivity of 0.5.

ber of runs to span the huge parameter space of temperature, pressure, flow rate, and gas-phase composition. The difficulty of preparing samples and optimizing the growth experimentally motivated the development of diamond growth models [4, 11].

1.3 Thesis Overview

The present research addresses some of the challenges in diamond surface science and uncovers new ones. In chapter 2, measurements of absolute deuterium coverage on C(100) by nuclear reaction analysis (NRA) are reported. This is the first time absolute coverage has been measured on a (2x1) surface with LEED characterization, confirming the (2x1):D reconstruction. Previous models of hydrogen reactions with C(100) are substantially revised to include all types of sites on the reconstructed surface, and it is shown that steady-state coverage measurements give the ratio of site-averaged abstraction rate to site-averaged recombination rate, k_A/k_R. The coverage measurements are analyzed to determine k_A/k_R at 1800°C filament temperature and 360°C surface temperature. Absolute deuterium coverage is also reported under a variety of dosing and annealing conditions. However, high filament temperature during dose produced unexpectedly high coverage, and D breakage of surface dimer bonds is proposed as a mechanism to increase coverage. The relevance of dimer breakage and dihydride formation to recent experiments on surface degradation are briefly discussed. All NRA measurements reported in Chapter 2 were completed at the Oak Ridge National Laboratory in Oak Ridge, Tennessee.

Issues related to the NRA measurements are addressed in the appendices. In appendix A, the question of subsurface signal in the NRA spectra is addressed by measurements of subsurface deuterium content via secondary-ion mass spectroscopy(SIMS). To prevent charging during SIMS, boron-doped samples were grown by microwave-plasma CVD. Sample growth and SIMS measurements took place at the National Institute for Research in Inorganic Materials, Tsukuba, Japan. In appendix B, a summary is given of the design and development of an ultrahigh vacuum endstation to perform measurements equivalent to NRA in the Caltech Pelletron.

The question of surface mobility at growth temperatures is addressed in chapter 3. Mobility is demonstrated by calculating activation energies for the migrations of H, F, and Cl on the C(110) surface by quantum chemical methods using hydrocarbon cluster models. The calculations included extensive basis sets with many-body effects at the level of single and double excitations from Hartree-Fock and Complete-Active-Space wavefunctions. The calculated activation barriers for the (1,2) migrations of H, F and Cl and the (1,3) migration of H indicate that such migrations are too slow to compete with thermal desorption. The (1,4) migration of F is also slow. However, the (1,4) migrations of both H and Cl are calculated to be sufficiently fast to compete with thermal desorption under ultrahigh vacuum conditions and with gas-surface reactions under typical diamond growth conditions. Previous studies had considered only the activation *barriers* to migrations [12] and growth reactions [13, 14, 15] and often concluded that migrations were negligibly slow due to their high barriers. This was the first study to consider the migration *rates* and establish that they were sufficiently fast to compete with gas-surface reactions during growth [16, 17, 18]. Implications of mobility for thermal desorption and diamond growth are briefly discussed. In appendix C, a kinetic Monte-Carlo algorithm is presented which incorporates mobility into diamond surface reaction models. The algorithm cuts in half the number of required integrations by addressing migration in the same iteration step as gas-surface reactions and developing a general scheme to weight reaction probabilities accordingly.

Bibliography

[1] Gaius Plinius Secundus (commonly referred to as Pliny the Elder), *Natural History*. Heinemann, London (1962). Translated by H. Rackham (Books 1 and 2, 1949) and D. E. Eichholz (Books 36 and 37, 1962), and quoted in G. Davies, *Diamond*, Adam Hilger Ltd., Bristol (1984) 5.

[2] G. Davies, *Diamond*. Adam Hilger Ltd., Bristol (1984).

[3] "The Diamond Empire." Frontline Documentary produced by Andre Singer, Steve Hewlett, Laurie Flynn, Robin Parmelee, WGBH, Boston (1994).

[4] D. G. Goodwin and J. E. Butler, "Theory of diamond chemical vapor deposition." In *Handbook of Industrial Diamond and Diamond Films*, edited by M. Prelas, G. Popovici and L. K. Bigelow, Marcel Dekker, Inc. (in press).

[5] J. E. Butler and R. L. Woodin, "Thin–film diamond growth mechanisms." Phil. Trans. R. Soc. London Ser. A **342**, 209 (1993).

[6] V. S. Smentkowski, H. Jänsch, M. A. Henderson and J. T. Yates, Jr., "Deuterium atom interaction with diamond (100) studied by X-ray photoelectron spectroscopy." Surf. Sci. **330**, 207–226 (1995).

[7] D. D. Koleske, S. M. Gates, B. D. Thoms, J. N. Russell, Jr. and J. E. Butler, "Hydrogen on polycrystalline diamond films—studies of isothermal desorption and atomic deuterium abstraction." J. Chem. Phys. **102**, 992–1002 (1995).

[8] B. D. Thoms, J. N. Russell, Jr., P. E. Pehrsson and J. E. Butler, "Adsorption and abstraction of hydrogen on polycrystalline diamond." J. Chem. Phys. **100**, 8425–8431 (1994).

[9] H. Zaidi, T. Lehuu and D. Paulmier, "Tribological behavior of hard carbon coatings deposited on steel substrates by plasma-assisted chemical-vapor-deposition." Diam. Rel. Mat. **3**, 787–790 (1994).

[10] M. N. Gardos, "Surface chemistry-controlled tribological behavior of silicon and diamond." Tribol. Lett. **2**, 173–187 (1996).

[11] S. J. Harris and D. G. Goodwin, "Growth on the reconstructed diamond (100) surface." J. Phys. Chem. **97**, 23–28 (1993).

[12] J. P. Lopez and W. H. Fink, "Ab-initio model cluster calculations of hydrogen atom diffusive motion across the (100) face of diamond." J. Phys. Chem. **86**, 2850–2853 (1982).

[13] M. Tsuda, M. Nakajima and S. Oikawa, "Epitaxial growth mechanism of diamond crystal in CH_4-H_2 plasma." J. Am. Chem. Soc. **108**, 5780–5783 (1986).

[14] S. P. Mehandru and A. B. Anderson, "Adsorption of H, CH_3, CH_2 and C_2H_2 on (2×1) restructured diamond (100)—Theoretical study of structures, bonding, and migration." Surf. Sci. **248**, 369–381 (1991).

[15] D. Huang and M. Frenklach, "Energetics of surface reactions on (100) diamond plane." J. Phys. Chem. **96**, 1868–1875 (1992).

[16] M. S. Melnik, D. G. Goodwin and W. A. Goddard, III, "Hydrogen migration on the diamond (110) surface." In *Adventures in Solid-State Research*, edited by F. Grunthaner, Southern California American Vacuum Society Symposium, Pasadena, CA (1992).

[17] M. S. Melnik and D. G. Goodwin, "Chlorine and fluorine migration on the diamond (110) surface." Bull. Am. Phys. Soc. **38**, 573 (March 1993).

[18] M. S. Melnik, D. G. Goodwin and W. A. Goddard, III, "*Ab initio* quantum chemical studies of hydrogen and halogen migration on the diamond (110) surface." Mat. Res. Soc. Symp. Proc. **317**, 349–354 (1994). The hydrogen migration

calculations were first published in the 1991 Annual Report of the Materials and Molecular Simulation Center, California Institute of Technology (1992), pp. 163–164.

[19] B. D. Thoms and J. E. Butler, "HREELS and LEED of H/C(100): the 2×1 monohydride dimer row reconstruction." Surf. Sci. **328**, 291–301 (1995).

[20] Y. L. Yang and M. P. D'Evelyn, "Theoretical studies of clean and hydrogenated diamond (100) by molecular mechanics." J. Vac. Sci. Technol. A **10**, 978–984 (1992).

[21] B. B. Pate, "The diamond surface: Atomic and electronic structure." Surf. Sci. **165**, 83–142 (1986).

[22] Y. Mitsuda, T. Yamada, T. J. Chuang, H. Seki, R. P. Chin, J. Y. Huang and Y. R. Shen, "Interactions of deuterium and hydrocarbon species with the diamond C(111) surface." Surf. Sci. **257**, L633–L641 (1991).

[23] R. E. Thomas, R. A. Rudder and R. J. Markunas, "Thermal desorption from hydrogenated and oxygenated diamond (100) surfaces." J. Vac. Sci. Technol. A **10**, 2451–2457 (1992).

[24] A. V. Hamza, G. D. Kubiak and R. H. Stulen, "Hydrogen chemisorption and the structure of the diamond C(100)-(2x1) surface." Surf. Sci. **237**, 35–52 (1990).

[25] G. D. Kubiak, "Correction to hydrogen chemisorption and the structure of the diamond C(100)-(2x1) surface." Surf. Sci. **237**, 42 (1992).

[26] C. A. Fox, G. D. Kubiak, M. T. Schulberg and S. Hagstrom, "Kinetics of hydrogen desorption from the diamond (110) surface." In *Proceedings of the Third International Symposium on Diamond Materials*, edited by J. P. Dismukes and K. V. Ravi, Electrochemical Society, Pennington, NJ (1993), pp. 64–70.

[27] J. E. Butler, B. D. Thoms, M. McGonigal, J. N. Russell, Jr. and P. E. Pehrsson, "Hydrogen chemistry on diamond surfaces." In *Wide Band Gap Electronic Mate-*

rials, edited by M. A. Prelas *et al.*, Kluwer Academic Publishers, the Netherlands (1995), pp. 105–114.

[28] J. L. Whitten, P. Cremaschi, R. E. Thomas, R. A. Rudder and R. J. Markunas, "Effects of oxygen on surface reconstruction of carbon." Appl. Surf. Sci. **75**, 45–50 (1994).

[29] G. A. Somorjai, *Introduction to surface chemistry and catalysis.* Wiley, New York (1994).

[30] Y. L. Yang, L. M. Struck, L. F. Sutcu and M. P. D'Evelyn, "Chemistry of hydrogen on diamond (100)." Thin Sol. Films **225**, 203–211 (1993).

[31] A. Hoffman, K. Bobrov, B. Fisgeer, H. Shechter and M. Folman, "Effects of deuterium adsorption–desorption on the state of diamond: surface degradation and stabilization of sp^3 bonded carbon." Diam. Rel. Mat. **5**, 977–983 (1996).

[32] C. A. Fox, S. Hagstrom, M. T. Schulberg and G. D. Kubiak, "Hydrogen desorption kinetics from low-index diamond surfaces." Extended Abstracts of the 183rd Electrochemical Society Meeting **93–1**, 601 (1993).

[33] R. P. Chin, J. Y. Huang, Y. R. Shen, T. J. Chuang and H. Seki, "Interaction of atomic hydrogen with the diamond C(111) surface studied by infrared-visible sum-frequency-generation spectroscopy." Phys. Rev. B **52**, 5985–5995 (1995).

[34] D. D. Koleske, S. M. Gates, B. D. Thoms, J. N. Russell, Jr. and J. E. Butler, "Isothermal desorption of hydrogen from polycrystalline diamond films." Surf. Sci. **320**, L105–L111 (1994).

[35] M. T. Schulberg, G. D. Kubiak and R. H. Stulen, "Temperature programmed desorption of hydrogen and deuterium from CVD diamond samples." Mat. Res. Soc. Symp. Proc. **207**, 401–406 (1992).

[36] T. Yamada, T. J. Chuang, H. Seki and Y. Mitsuda, "Chemisorption of fluorine, hydrogen and hydrocarbon species on the diamond C(111) surface." Mol. Phys. **76**, 887–908 (1992).

[37] J. B. Marsh and H. E. Farnsworth, "Low-energy electron diffraction studies of (100) and (111) surfaces of semiconducting diamond." Surf. Sci. **1**, 3–21 (1964).

[38] P. G. Lurie and J. M. Wilson, "The diamond surface I. The structure of the clean surface and the interaction with gases and metals." Surf. Sci. **65**, 453–475 (1977).

[39] S.-T. Lee and G. Apai, "Surface phonons and CH vibrational modes of diamond C(110) and C(111) surfaces." Phys. Rev. B **48**, 2684–2693 (1993).

[40] S. Skokov, B. Weiner and M. Frenklach, "Chemistry of acetylene on diamond (100) surfaces." J. Phys. Chem. **99**, 5616–5625 (1995).

[41] B. J. Garrison, E. J. Dawnkaski, D. Srivastava and D. W. Brenner, "Molecular dynamics simulation of dimer opening on a diamond (100) (2×1) surface." Science **255**, 835 (1992).

[42] B. D. Thoms, P. E. Pehrsson and J. E. Butler, "A vibrational study of the adsorption and desorption of hydrogen on polycrystalline diamond." J. Appl. Phys. **75**, 1804–1810 (1994).

[43] T. Ando, M. Ishii, M. Kamo and Y. Sato, "H–D exchange reaction on diamond surfaces studied by diffuse reflectance Fourier transform IR spectroscopy." Diam. and Rel. Materials **4**, 607–611 (1995).

[44] T. Ando, M. Ishii, M. Kamo and Y. Sato, "Thermal hydrogenation of diamond surfaces studied by diffuse reflectance Fourier transform infrared spectroscopy, temperature-programmed desorption and laser Raman spectroscopy." J. Chem. Soc., Faraday Trans. **89**, 1783–1789 (1993).

[45] B. D. Thoms, M. S. Owens, J. E. Butler and C. Spiro, "Production and characterization of smooth, hydrogen-terminated diamond C(100)." Appl. Phys. Lett. **65**, 2957–2959 (1994).

[46] V. S. Smentkowski and J. T. Yates, Jr., "Temperature control and measurement for diamond single crystals in ultrahigh vacuum." J. Vac. Sci. Tech. A **11**, 3002–3006 (1993).

[47] M. J. Bozack, L. Muehlhoff, J. N. Russell, Jr., W. J. Choyke and J. T. Yates, Jr., "Methods in semiconductor surface chemistry." J. Vac. Sci. Tech. A **5**, 1–8 (1987).

[48] R. P. Chin, *Nonlinear optical spectroscopy of diamond surfaces.* Ph.D. thesis, University of California, Berkeley, Berkeley, CA (1995). Also available as Lawrence Berkeley Laboratory Report no. LBL-37110.

[49] U. Bischler and E. Bertel, "Simple source of atomic hydrogen for ultrahigh-vacuum applications." J. Vac. Sci. Tech. A **11**, 458–460 (1993).

[50] S. A. Buntin, "Hyperthermal H atom interactions with D/Si(100) - effects of incident H atom kinetic-energy on the removal of adsorbed D." J. Chem. Phys. **105**, 2066–2075 (1996).

[51] I. Langmuir, "The dissociation of hydrogen into atoms: Calculation of the degree of dissociation and the heat of formation." J. Am. Chem. Soc. **36**, 417–458 (1914).

[52] I. Langmuir and G. M. J. Mackay, "The dissociation of hydrogen into atoms: Part I. Experimental." J. Am. Chem. Soc. **36**, 1708 (1914).

[53] I. Langmuir. J. Chem. Soc. **1**, 511 (1940).

[54] D. Brennan and P. C. Fletcher, "The atomization of hydrogen on tungsten." Proc. Roy. Soc. London A **250**, 389–408 (1959).

[55] J. N. Smith, Jr. and W. L. Fite, "Reflection and dissociation of H_2 on tungsten." J. Chem. Phys. **37**, 898–904 (1962).

[56] G. Ehrlich, "Molecular dissociation and reconstitution on solids." J. Chem. Phys. **31**, 1111–1126 (1959).

[57] S. J. Harris, "Mechanism for diamond growth from methyl radicals." Appl. Phys. Lett. **56**, 2298–2300 (1990).

[58] C. T. Rettner and D. J. Auerbach, "Dynamics of the formation of HD from D(H) atoms colliding with H(D)/Cu(111)—a model study of an Eley–Rideal reaction." Surf. Sci. **357–358**, 602–608 (1996).

[59] C. C. Cheng, S. R. Lucas, H. Gutleben, W. J. Choyke and J. T. Yates, Jr., "Atomic hydrogen driven halogen extraction from Si(100) —Eley–Rideal surface kinetics." J. Am. Chem. Soc. **114**, 1249 (1992).

[60] D. D. Koleske, S. M. Gates and J. A. Schultz, "Facile abstraction of chemisorbed-D on Si(100) by atomic-H." J. Chem. Phys. **99**, 5619 (1993).

[61] F. Akatsuka, Y. Hirose and K. Komaki, "Rapid growth of diamond films by arc discharge plasma CVD." Jap. J. Appl. Phys. **27**, L1600–L1602 (1988).

[62] S. Tennant, "On the nature of the diamond." Phil. Trans. R. Soc. London **87**, 97–99, 123 (1797).

[63] J. N. Gannal, "Sur l'action du phosphore mis en contact avec le carbure de soufre pour en séparer le carbone pur ou le diamant." J. Chim. Med. **4**, 582–584 (1828).

[64] X. Z. Zhao, R. Roy, K. A. Cherian and A. Badzian, "Hydrothermal growth of diamond in metal-C-H_2O systems." Nature **385**, 513–515 (1997).

[65] C. Despretz. C. R. Acad. Sci. Paris **25**, 81 (1847). Cited in G. Davies, *Diamond*, Adam Hilger Ltd., Bristol (1984).

[66] H. Moissan, *The Electric Furnace*. Edward Arnold, London (1904). Cited in G. Davies, *Diamond*, Adam Hilger Ltd., Bristol (1984).

[67] R. H. Wentorf, Jr., "Diamond synthesis." In *Advances in Chemical Physics Volume IX*, edited by I. Prigogine (1965), pp. 365–404.

[68] J. W. Hershey, *The book of diamonds.* Hearthside Press, New York (1940).

[69] Y. Matsui, A. Yuuki, M. Sahara and Y. Hirose, "Flame structure and diamond growth mechanism of acetylene torch." Jap. J. Appl. Phys. Part 1. **28**, 1718–1724 (1989). See also Y. Hirose, Abstracts of 1st Intl. Conf. on New Diamond Sci. and Tech., Japan New Diamond Forum, Tokyo (1988) 38; Y. Hirose and N. Kondoh, Extended Abstracts of the 35th Spring Meeting of the Japan Society of Applied Physics and of Related Societies, Tokyo (March 1988) 29a-T-1; L. M. Hanssen, W. A. Carrington, J. E. Butler and K. A. Snail, "Diamond synthesis using an oxygen-acetylene torch." Matls. Ltrs. **7** (1988) 289–292.

[70] Y. Tzeng, C. Cutshaw, R. Phillips, T. Srivinyunon, A. Ibrahim and B. H. Loo, "Growth of diamond films on silicon from an oxygen–acetylene flame." Appl. Phys. Lett. **56**, 134–136 (1990).

[71] W. G. Eversole, "Synthesis of diamond." U.S. Patent 3030188 (1962).

[72] J. C. Angus and C. C. Hayman, "Low pressure metastable growth of diamond and 'diamondlike' phases." Science **241**, 913–921 (1988).

[73] F. G. Celii and J. E. Butler, "Diamond chemical vapor deposition." Ann. Rev. Phys. Chem. **42**, 643–684 (1991).

[74] Y. Sato and M. Kamo. In *The Properties of Natural and Synthetic Diamond*, edited by J. E. Field, Academic Press, London (1992), p. 424.

[75] D. W. Kweon, J. Y. Lee and D. H. Kim, "The growth kinetics of diamond films deposited by hot-filament chemical vapor deposition." J. Appl. Phys. **69**, 8329–8335 (1991).

[76] M. Kamo, Y. Sato, S. Matsumoto and N. Setaka, "Diamond synthesis from gas phase in microwave plasma." J. Crystal Growth **62**, 642–644 (1983).

[77] M. Frenklach and K. E. Spear, "Growth of vapor-deposited diamond." J. Mat. Res. **3**, 133–140 (1988).

[78] D. N. Belton and S. J. Harris, "A mechanism for growth on diamond (110) from acetylene." J. Chem. Phys. **96**, 2371–2377 (1992).

[79] M. S. Melnik, S. Koizumi, T. Ando, M. Nishitani, M. Kamo and Y. Sato. Unpublished (1995).

[80] T. Ando, S. Koizumi, M. Nishitani, M. Kamo and Y. Sato. Private communication (1995).

[81] M. Kamo and Y. Sato, "Diamond synthesized by the microwave plasma CVD method." In *Proceedings of the Second International Symposium on Diamond Materials*, edited by A. J. Purdes, J. C. Angus, R. F. Davis, B. M. Meyerson, K. E. Spear and M. Yoder, The Electrochemical Society Inc., Pennington, NJ (1991), pp. 20–30.

[82] E. J. Corat and D. G. Goodwin, "Temperature dependence of species concentrations near the substrate during diamond chemical vapor deposition." J. Appl. Phys. **74**, 2021–2029 (1993).

[83] W. L. Hsu and D. M. Tung, "Application of molecular-beam mass-spectrometry to chemical-vapor-deposition studies." Rev. Sci. Instr. **63**, 4138–4148 (1992).

[84] M. C. McMaster, W. L. Hsu, M. E. Coltrin, D. S. Dandy and C. Fox, "Dependence of the gas composition in a microwave plasma-assisted diamond chemical-vapor-deposition reactor on the inlet carbon source—CH_4 versus C_2H_2." Diam. Rel. Mat. **4**, 1000–1008 (1995).

[85] M. C. McMaster, W. L. Hsu, M. E. Coltrin and D. S. Dandy, "Experimental measurements and numerical simulations of the gas composition in a hot-filament-assisted diamond chemical-vapor-deposition reactor." J. Appl. Phys. **76**, 7567–7577 (1994).

Chapter 2 Deuterium Reaction with C(100): Ion-Beam Scattering Experiment

2.1 Introduction

Diamond surface experiments have attracted attention in recent years [1], fueled by the relevance to models of low-pressure diamond thin-film growth [2, 3, 4] for electronic and industrial applications. Although the experiments have increased our understanding of diamond surface processes, several issues remain unresolved. These include absolute hydrogen coverage on C(100) and the rates of abstraction and recombination with gas-phase atomic hydrogen. Absolute coverage is an important parameter in diamond surface models, and predictions for the (100) face range from 0 to 1.33 hydrogen per surface carbon [5, fig. 4]. A coverage of two hydrogen per surface carbon has also been proposed, but has been found to be unstable due to the steric crowding of the hydrogens [5, 6]. Reaction rate constants are intimately related to coverage, in that they determine the saturation coverage under typical hydrogen dosing conditions and the fraction of sites available for growth during thin-film deposition. Issues relating to hydrogen coverage are reviewed in section 2.1.1, and reaction-rate research is discussed in section 2.1.2. Section 2.1.3 concludes with an overview of the chapter.

2.1.1 Hydrogen coverage

Measurements of absolute hydrogen coverage are rare. Relative coverages may be measured by intergrating peaks generated by surface spectroscopies or temperature-programmed desorption (TPD), but the normalization factors are difficult to calibrate. In contrast, ion-beam scattering techniques are easily calibrated by comparison to ion-implanted standards, and nuclear sensitivity assures that the measurement integrates equally over all bonding configurations. Derry *et al.* [7] measured coverage on polished C(100) by nuclear reaction analysis and found 2 H per surface C. However, the sample was unheated and may have contained physisorbed hydrocarbons. Yagi *et al.* [8] found 3–4 H per surface C on MWCVD homoepitaxial C(100) by elastic-recoil spectrometry. Their samples were also unheated. Dollinger *et al.* [9] found a coverage of 1 H per surface C on plasma-treated C(100) by medium-energy ion-scattering (MEIS). The exact value of hydrogen coverage on C(100) remains unresolved.

The coverage is modified when diamond is dosed with atomic hydrogen gas, due to abstraction and recombination reactions. The absolute saturation coverage from dosing has not been measured but may be estimated from reaction-rate ratios implied by relative coverage measurements. Thoms *et al.* [10] obtained a ratio implying 0.95 ± 0.01 D per surface C on polycrystalline diamond by high-resolution electron-energy loss spectroscopy (HREELS). The gas-phase temperature was equal to the filament temperature, 1800°C, and the surface temperature was 80°C in one set of experiments and 600°C in another. Both surface temperatures implied the same coverage. Koleske *et al.* [11] obtained a ratio implying 0.97 ± 0.01 D per surface C at a filament temperature of 1560°C from time-of-flight scattering and recoil-ion spectroscopy (TOF-SARS). However, Chin *et al.* [12, 13] measured a ratio implying 0.83 H per surface C from sum-frequency generation (SFG) spectroscopy of hydrogen-dosed diamond (111). Chin's filament was at 1800°C during dosing, and his surface temperature varied from room temperature to 200°C due to radiative heating by the hot filament. The saturation coverage may vary with filament temperature, surface temperature, hydrogen isotope and crystallographic orientation of the surface. Full characterization of the effect of dosing parameters on absolute coverage has yet to be accomplished.

Monohydride vs. dihydride production by dosing

Although the (100):(2×1) surface contains up to 1 H per surface C, hydrogen coverage can be greater than 1 due to the presence of dihydrides. The (100) crystal plane cuts

2 bonds for each carbon, leaving enough unpaired electrons to form up to two CH bonds, or 2 H per surface C. However, the steric crowding of neighboring hydrogen centers makes this surface unstable to reconstruction to a (2×1) structure, with up to 1 H per surface C, or a (3×1) structure, with up to 1.33 H per surface C [5, fig. 4]. The carbon centers on the (2×1) surface form rows of dimer bonds with monohydride termination, and those of the (3×1) surface form rows of dimer bonds alternating with undimerized dihydrides. Low-energy electron diffraction (LEED) distinguishes between the (2×1) and (3×1) structures. However, for small surface domains less than ~100Å across, LEED shows only the (1×1) pattern of the underlying bulk atoms. Reported LEED patterns of C(100) include both the (1×1) [14, 15, 16, 17, 18], consistent with disordered dihydrides or monohydrides, and (2×1) [17, 18, 19, 20], consistent with ordered monohydrides. Sample preparation [16, 19], surface roughness [12], and surface temperature during hydrogen dosing [13] have all been found to affect reconstruction and surface quality. The existence of dihydrides cannot be established by LEED, and conditions which generate dihydrides remain controversial.

Infrared spectroscopy is able to distinguish between mono- and di-hydrides and has the advantage of good resolution, ~6-20 cm^{-1}. Infrared sum-frequency generation (SFG), a nonlinear optical effect, is symmetry-forbidden in the bulk and therefore has excellent surface sensitivity. Chin [12] found peaks with shoulders in the CH stretch region on polished C(100) by SFG. However, he was unable to observe bending modes, and he interpreted the spectra as indicating monohydrides with two different bonding arrangements. Fourier-transform infrared spectroscopy (FTIR) has good resolution but poor surface sensitivity. Surface sensitivity is increased by performing multiple-internal-reflection FTIR (MIRIRS). Yang *et al.* [5] found a CD deformation mode at 901 cm^{-1} on polished C(100) by MIRIRS following exposure to atomic deuterium. However, they were unable to distinguish surface CH stretches from background due to hydrocarbon impurities.

HREELS identifies hydrides by assigning loss peaks to CH and CH_x stretch and deformation modes. However, peak assignment is rendered difficult by poor resolution, typically 60–100 cm^{-1} [21]. For a surface with a mixture of mono- and dihydrides, CH_2 symmetric and antisymmetric stretches may be indistinguishable from the CH stretch peak. Spectral deconvolution and off-specular collection are two of the most powerful tools in interpreting spectra. However, specular deconvolution which assumes dipole selection rules is invalid on C(100), and impact scattering selection rules are difficult to apply [22]. When dipole scattering dominates, on-specular collection gives sensitivity to modes with dynamic-dipole moments perpendicular to the surface, namely CH stretch and CH_2 symmetric stretch. However, in off-specular collection, impact scattering increases relative sensitivity to CH_2 antisymmetric stretch. Therefore, dihydrides may be identified by a splitting in the CH stretch peak as the collection moves from on-specular through off-specular angles.

HREELS experiments show evidence for both mono- and di-hydrides. Lee and Apai [17] performed spectral deconvolution on data from polished C(100) and concluded that the (1×1) surface contained mono-, di- and tri-hydrides. However, the assumption of dipole selection rules may be inaccurate [22]. Heating the sample to 1200°C produced a (2×1) surface which was concluded to be totally free of hydrogen from the lack of any CH stretch modes near 2900 cm^{-1}. Dosing the sample with atomic hydrogen reproduced the (1×1) pattern and the original spectra with multiple-hydride modes. Results were completely reproducible upon repeated dosing–annealing (adsorption–desorption) cycles. Aizawa *et al.* [23] found no splitting of the CH stretch peak at off-specular angles and concluded that the surface contained only monohydrides. Their sample was grown by microwave-plasma CVD on a (100) substrate. Sun *et al.* [24] assigned modes to the features in their specular HREEL spectra and concluded that the surface contained dihydrides. However, the assumption of dipole selection rules may again be inaccurate. The sample was facetted (100) grown by hot-filament CVD on a silicon substrate. Thoms *et al.* [19] detected no CH peak split at off-specular angles and concluded that their sample was terminated by monohydrides. The sample was hydrogen-plasma treated C(100). The sample remained (2×1) even upon hydrogen dosing, and spectra were completely reproducible upon repeated adsorption–desorption cycles.

Evidence for mono- and di-hydrides has been found by temperature-programmed desorption (TPD) and electron-stimulated desorption (ESD). TPD spectra from C(100) typically show a single peak near 900°C assigned to H_2 desorption from monohydride sites [20]. However, Yang *et al.* [5] observed a low-temperature shoulder in the desorption peak from polished C(100) and suggested dihydrides as a cause by analogy with Si(100).[1] Hoffman *et al.* [27] found two desorption peaks from C(100):(1×1).[2] Double desorption peaks appeared after repeated adsorption–desorption cycles, coupled with electron bombardment, which may indicate dihydride generation. Hamza *et al.* [18] observed two H^+ peaks in time-of-flight ESD on polished C(100):(1×1) and assigned the fast peak to dihydrides. Upon annealing to 900°C the fast H^+ peak disappeared, the surface displayed a (2×1) LEED pattern, and the remaining peak was assigned to monohydrides. Dosing the sample with atomic hydrogen returned the surface to a (1×1) structure and reproduced the original ESD peaks. After repeated adsorption–desorption cycles, the (2×1) pattern was no longer generated.

Clearly, both monohydrides and dihydrides exist on the C(100) surface, and the conditions to generate dihydrides remain unclear. The greater roughness of polished surface increases the probability of dihydrides. However, even a smoother H-plasma treated samples can exhibit double TPD peaks upon repeated adsorption–desorption cycling (coupled with electron-beam irradiation) [27]. Conditions under which dihydrides appear upon adsorption–desorption cycling have yet to be understood.

2.1.2 Abstraction and recombination reaction rates

The ratio of the rate constant for hydrogen abstraction (k_A) to that for recombination (k_R), when averaged over all surface sites, is important in both diamond surface science and diamond growth experiments. In diamond surface science it determines the maximum surface coverage attainable by typical hydrogen dosing conditions, and in diamond chemical-vapor deposition (CVD) it determines the fraction of surface

---

[1] Butler *et al.* [25] also published desorption peaks with distinct shoulders from C(110), and Hagstrom *et al.* [26] found double desorption peaks from C(111).

[2] Hoffman [28] recently found low and high-temperature desorption peaks from C(111) and assigned them to desorption from dihydride dimers at steps and monohydride sites on terraces, respectively.

sites available for growth.

Recently several groups have measured the ratio, k_A/k_R. The results are not directly comparable across experiments due to variations in crystallographic orientation of the sample surface, hydrogen gas temperature and hydrogen isotope. However, all experiments disagree by an order of magnitude with a ratio commonly used in diamond growth models. Thoms *et al.* [10] inferred a k_A/k_R of 0.05 ± 0.01 from HREELS of deuterium-dosed polycrystalline diamond. Due to the low pressure in the reaction chamber, the gas-phase temperature was equal to the filament temperature, 1800°C, and the surface temperature was 80°C in one set of experiments and 600°C in another. Both surface temperatures gave the same k_A/k_R. Koleske *et al.* [11] obtained a similar reaction-rate ratio of 0.03 ± 0.01 at a filament temperature of 1560°C from TOF-SARS. However, Chin *et al.* [12, 13] obtained a ratio of 0.2 from SFG spectroscopy of hydrogen-dosed diamond (111). Chin's filament was at 1800°C during dosing, and his surface temperature varied from room temperature to 200°C due to radiative heating by the hot filament. On the other hand, reaction rates typically used in thermochemical kinetic diamond growth models [29, 30] give a ratio of 2.14 at 1800°C. These rate constants were estimated from gas-phase data, where the hydrogen temperature is the same as that of the alkane modeling the surface.

Due to the dearth of gas-surface reaction-rate data, diamond growth modelers extract their rates from analogous gas-phase reactions [29, 31]. However, surface reactions differ from gas-phase reactions due in part to steric hindrance from surrounding surface atoms and the strain of the underlying lattice. Surface effects are approximated by taking the high-pressure limit of gas-phase rate constants [29, 31], and errors are introduced by the inadequacy of this approximation. Moreover, due to the exponential dependence on temperature and the variation across experiments, many gas-phase rate constants are not known to better than a factor of five. Therefore the ratio of rate constants taken from gas-phase data may be in error by an order of magnitude. Directly measuring the *ratio* of recombination to abstraction rate constants on a diamond surface would improve the accuracy of growth models.

Nevertheless, reaction rates measured by surface-science experiments are difficult to apply to CVD conditions. Surface-sensitive techniques such as HREELS, TOF-SARS, and SFG require low pressure to minimize beam attenuation and ultra-low pressure to avoid surface contamination. At such low pressures the mean free path of the gas molecules is much larger than the size of the vacuum chamber itself. Although this gives surface-science experiments the unique ability to separately control gas and surface temperatures, the large difference between gas and surface temperature make the data difficult to apply to continuum reactions. To date all experiments have fixed the gas temperature and most have investigated only one or two surface temperatures. Only the TOF-SARS experiment has measured reaction rate for a series of surface temperatures and found an apparent activation barrier of 0.8 ± 0.2 kcal/mol, suggesting a direct (Eley-Rideal) reaction upon impact with the surface, with an early transition state. In contrast, in a Langmuir-Hinshelwood mechanism the gaseous species equilibrates with the surface before reacting, and the rate is determined by the surface temperature, T_s. Measuring k_A/k_R for a series of gas and surface temperatures would tell which mechanism is active or whether both participate to a degree, e.g., $\frac{k_A}{k_R} = A \exp \frac{-E_g}{k_B T_g} \exp \frac{-E_s}{k_B T_s}$. It would also clarify the relevance of low-pressure data, where $T_g \neq T_s$, to diamond growth, where $T_g = T_s$.

The effect of isotope on reaction rate is unknown. Some experiments exposed a deuterated diamond surface to hydrogen gas while others exposed a hydrogenated diamond to deuterium gas. Most groups assume $k_H = k_D$ when reducing their data, and in some cases the isotopic effect has been investigated and found to be small.[3] In SFG experiments Chin *et al.* [13] found the rate of reaction of gas-phase H with C(111) to be similar to that of gas-phase D. However, Koleske *et al.* [11] measured the rate of D(g) abstraction of surface-bonded H to be 2–4 times the rate of H(g) abstraction of D on polycrystalline diamond. They suggest that on C(111)-like sites, D(g) is more efficient at abstraction because its higher momentum allows it to impart a greater displacement to the surface carbon, establishing a weak π-bond between the surface and neighboring carbon atoms. It has yet to be determined whether the isotopic effect

---

[3] In the case of a surface-surface reaction, thermal desorption, Schulberg *et al.* [32] observed no isotopic effect on desorption of H_2, HD and D_2 from polycrystalline CVD diamond.

varies with crystallographic orientation. On a surface analogous to C(100), Si(100), Sinniah *et al.* [33] found an isotopic effect opposite to that on polycrystalline diamond: the rate for D(g) abstraction of surface-bonded H was only 0.2 times the rate for H(g) abstraction of D. Thus, the isotopic effect on diamond surface reactions remains unresolved, and its dependence on surface orientation requires further investigation.

2.1.3 Chapter overview

The issues of absolute coverage on C(100), its dependence on dosing conditions, and the reaction-rate ratio k_A/k_R are addressed by measuring the amount of deuterium on the diamond surface by nuclear reaction analysis (NRA). Absolute deuterium coverage is reported under a variety of sample annealing and atomic deuterium dosing conditions. The experimental procedure is described in section 2.2, and results are reported in section 2.3. Coverage is measured for dosing at 1800°C filament temperature and 360°C surface temperature. However, an attempt to identify the effect of gas and surface temperatures on reaction rates revealed unexpectedly high coverages at high filament temperature. A generic mechanism to generate high coverage at high filament temperature is proposed in section 2.4.5 and compared to the results of previous dosing experiments. In section 2.5 previous models of hydrogen reactions with C(100) are substantially revised to include all types of sites on the reconstructed terrace, and it is shown that steady-state coverage measurements give the ratio of site-averaged abstraction rate to site-averaged recombination rate, k_A/k_R. Section 2.5 discusses the relevance of the results to chemical kinetics models of diamond growth. Finally, section 2.6 summarizes the conclusions.

2.2 Experimental procedure

Unless otherwise noted, all experiments were performed at the Surface Modification and Characterization (SMAC) Research Center of Oak Ridge National Laboratory in Oak Ridge, Tennessee.

2.2.1 Sample preparation

The sample was a type IIA natural diamond cut along (100) ± 3° by Harris Diamond Corporation. In a prior experiment at Caltech, the sample had been bombarded with 1.9 MeV $^4He^+$ at 5nA for ~50 minutes to obtain RBS and ERS spectra. The bombardment produced some lattice damage and turned the sample from colorless to light grey.

To clean the surface for the NRA experiment, the sample was hydrogen-plasma treated in an Astex reactor at the Gas/Surface Dynamics Section of the Naval Research Laboratory. Hydrogen plasma treatment is one of the most reliable methods to prepare diamond samples. Plasma treatment smooths the (100) surface and causes it to reconstruct to (2x1):H [34]. Prior to treatment the sample was boiled for 15 minutes in a solution of 3 parts HCl to 1 part HNO_3 aqua regia, followed by boiling for 18 minutes in a solution of 3 parts H_2SO_4 to 2 parts HNO_3. The sample was then hydrogen-plasma treated at 750°C and 10 torr for 20 minutes. The microwave power was 600 W, and the hydrogen flow rate was 500 sccm. The temperature was measured by a thermocouple located behind the substrate heater; the actual diamond surface temperature was estimated to be 800°C. The reactor contained a CVD-diamond-coated substrate holder to minimize sample contamination. Finally, the back side of the sample was also plasma treated.

2.2.2 Deuterium dosing

The sample was mounted on an all-molybdenum holder and installed in a stainless steel ultrahigh vacuum chamber (fig. 2.1). The chamber was pumped by turbomolecular and ion pumps. The base pressure was 2.0×10^{-10} torr, and the dosing pressure was 5.0×10^{-6} torr. During sample annealing, the pressure momentarily rose to $\sim 2 \times 10^{-8}$ torr, presumably due to outgassing of D_2 from the ceramic beads insulating the thermocouple leads. The sample was heated by electron bombardment of the back of the molybdenum holder. The sample temperature was measured by an E-type thermocouple clamped to the front of the sample holder about 3 mm from the

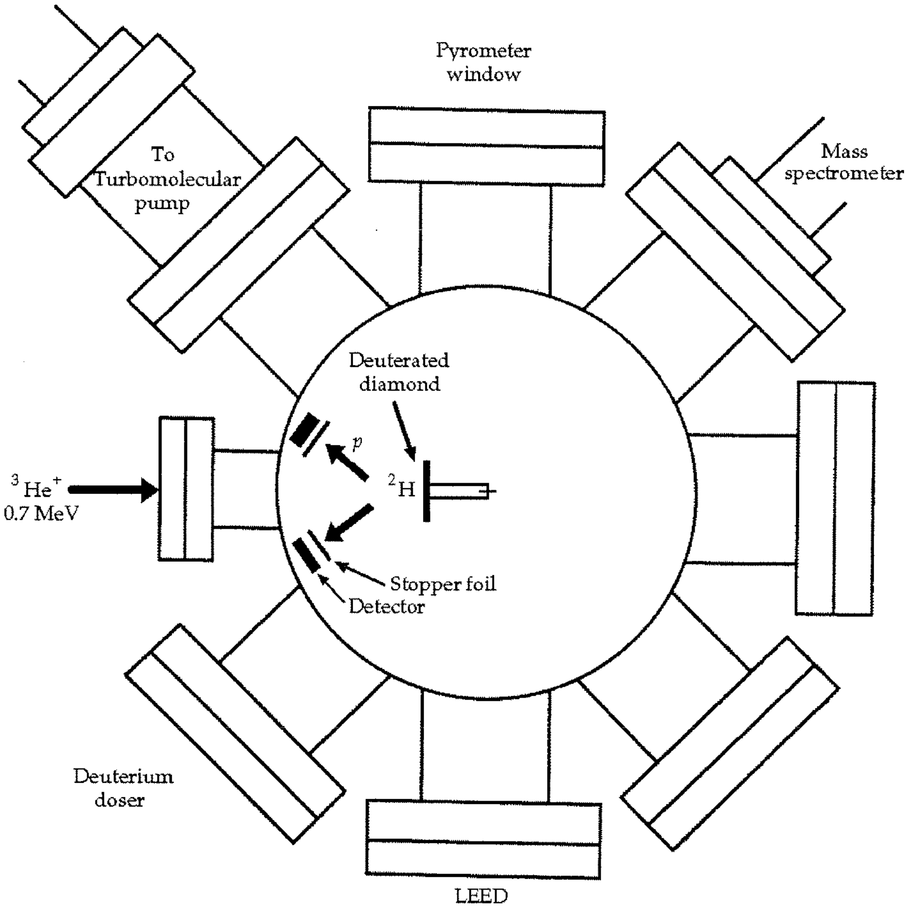

Figure 2.1: NRA set-up.

sample. The filament's brightness temperature was measured via optical pyrometry, and values were converted to absolute temperature [35, p. 10-283] without correcting for viewport bias. The sample temperature during bake-out was similar to that of the rest of the chamber, and the sample surface and doser filament were annealed prior to each dose. The ion pump was valved-off during dosing, to extend its life, and during annealing, to minimize the partial pressure of D_2.

Prior to each dose, the sample and doser filament were annealed simultaneously to avoid cross-contamination. Before annealing the sample was positioned to face $\sim$180° away from the doser. Then the doser filament was outgassed at 2220°C for 2 minutes in order to desorb any tungsten oxide [36, 37]. After 2 minutes, the sample was flashed to 990°C and held between that and $\sim$1050°C for about 2 minutes to desorb the surface hydrogen. (Thoms *et al.* [19] conclude from their HREEL spectra that C(100) is free of adsorbed hydrogen upon heating to 1050°C for approximately one minute.) Then the heater bias voltage was turned off, and the hot filament was decreased to ~50°C above the filament dosing temperature. Once the sample had cooled to a few degrees above the surface dosing temperature, the filament temperature was decreased to its dosing value, and the D_2 leak valve was opened. After the pressure had stabilized to 5.0×10^{-6} torr, the sample was quickly rotated into the dosing position. About 3 seconds were required to rotate the sample into position, and exposures were not corrected for the rotation time. In the dosing position, the distance between the sample surface and doser filament was about 4 cm. Throughout dosing the sample temperature was maintained to within 3°C of the desired surface dosing temperature by radiative heating from behind. Upon completion of dosing, the sample was quickly rotated to face ~180° away from the doser, the leak valve was simultaneously closed, and then the doser filament amperage was turned off.

During exposure the surface temperature was either 80° ± 3°C or 360° ± 3°C, and the filament temperature was 1735° ± 20°C, 1800° ± 20°C, 1975° ± 20°C, or 2025° ± 20°C. The true filament temperature is higher than the measured value by about 50°C due to viewport bias [38].

2.2.3 Coverage measurement and calibration

The total deuterium coverage, θ_D, was measured by counting the protons produced by the nuclear reaction ${}^2\mathrm{D}({}^3\mathrm{He}, \mathrm{p}){}^4\mathrm{He}$. The incident ${}^3\mathrm{He}^+$ beam energy was 0.7 ± 0.003 MeV, the current was typically 1 nA, and the beam spot diameter at the sample was 2 mm. Collection time for each spectrum was about 100 seconds. Relative beam dose was measured by accumulating backscattered ions from a gold-plated beam chopper rotating at ~10 Hz. The beam was incident normal to the sample, and the proton spectra were collected by four solid-state detectors located about 2 cm in front of the sample. Stopper foils of 25.4 μm thick nickel were placed in front of the four detectors to filter out backscattered ${}^3\mathrm{He}^+$ ions and pass the ~13 MeV protons [39, p. 238]. The deuterium doser filament, which was located a few cm from the four detectors, was turned off during NRA to keep the spectrum's proton peak well-separated from the thermal noise peak.

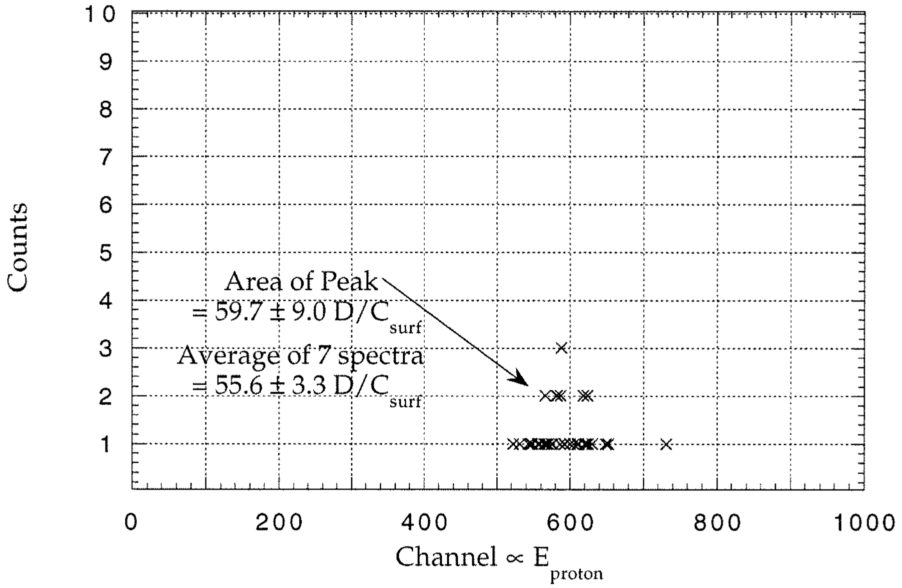

Figure 2.2: NRA spectrum of D-terminated C(100). The quoted errors represent the resolution in the measurement due to the finite number of events counted. For example, a total of 44 events were detected in this spectrum. The spectrum was collected subsequent to 1500L exposure at a filament temperature of 1800°C and a surface temperature of 360°C, followed by a series of anneals to 800°C and 630°C.

The sample was aligned with respect to the beam spot by scanning in the two directions perpendicular to the beam, y and z, and by rotating the sample about the z axis. Coverage values peaked on the sample and decreased when the beam was scanned off the sample onto the holder. After alignment, spectra were typically collected at two to four locations completely on the sample, and often more than one spectrum was taken at any one location. The spatial deuterium distribution was uniform over the sample to within the scatter from spectrum to spectrum at any one location. The coverage is assigned to be the average value of all the spectra taken at the two to four locations. The resolution in the coverage measurement is taken to be $\frac{\theta_D}{\sqrt{N}}$, where θ_D is the measured coverage, and N is the total number of events counted.

Deuterium coverage was calibrated by comparing the total counts from the sample

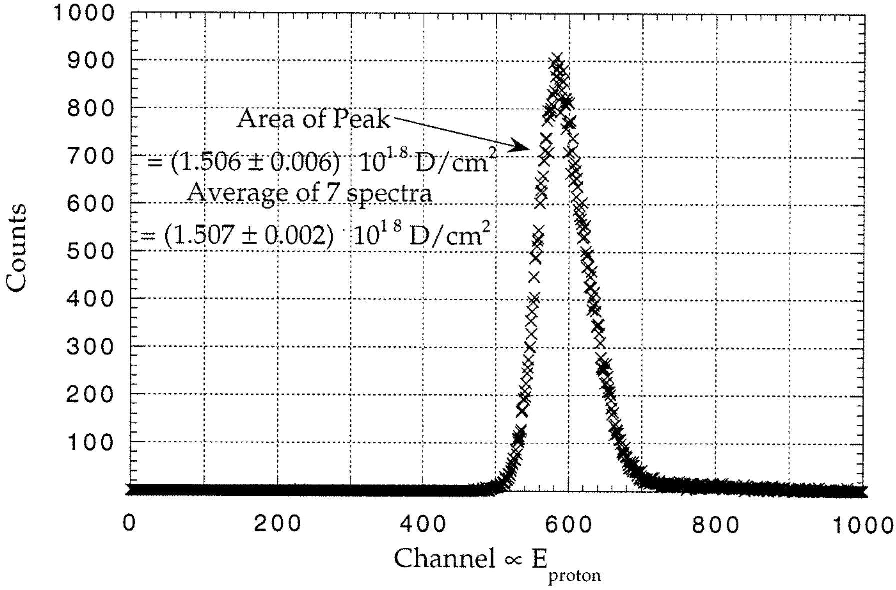

Figure 2.3: NRA spectrum of calibration standard. The quoted errors represent the resolution in the measurement due to the finite number of events counted. A total of 70873 events were detected in this spectrum.

to the total counts from a secondary standard. The secondary standard was an *a*-C film chemically vapor-deposited in deuterium atmosphere on a Si substrate. In a prior experiment the D incorporation in the film was measured to be $(1.5 \pm 0.01) \times 10^{18}$ D/cm^2 by comparison to a primary (ion-implanted) *a*-C standard. In the NRA experiment, the (secondary) standard was first located with respect to the beam spot by scanning in the y and z directions. Spectra were then collected at four locations on the standard, and the resulting deuterium distribution was uniform to within 3%. The average of the total counts in the four spectra was taken to be equivalent to 1.5×10^{18} D/cm^2. Calibration spectra were collected several times over the course of the experiment, and the average value varied by only about ~1%. The error in the calibration factor is taken to be 1%. Sample NRA spectra are shown in figs. 2.2 and 2.3.

Deuterium coverages are reported in units of D per surface C, where the areal density of surface carbons is assumed to be that of an ideal (100) surface, 1.566×10^{15}/cm^2.

The lower detection limit of NRA is determined by the background cosmic radiation incident on the detectors. For spectral collection times typical to this experiment, the spectrum for no incident helium ions consisted of one count, implying a lower detection limit of 0.02×10^{15}D/cm^2 or 0.013 D per surface C.

2.3 Results

2.3.1 Surface reconstruction

Due to the hydrogen-plasma pretreatment, the sample surface was reconstructed upon insertion into the vacuum chamber [34]. The (2x1) reconstruction remained even after several thousand langmuirs (L) of deuterium dosing. After about 10^4 L of exposure, the surface reconstruction was characterized via LEED at ~115 V, and a (2x1) pattern was clearly evident. During LEED the sample was heated to ~100°C to avoid charging.

2.3.2 Coverage at 1800°C

Figure 2.4 shows deuterium coverage after dosing at a filament temperature of 1800°C and a surface temperature of 360°. Coverages are reported in units of monolayers, where one monolayer is one D per surface C, and the atomic density is taken to be that of the ideal (100) surface, 1.57×10^{15}C/cm^2. An exposure of 2500L appears to be sufficient to reach saturation coverage. The saturation coverage of 0.95 ± 0.04 agrees with the coverage of 0.95 ± 0.01 implied by Thoms *et al.*'s [10] analysis of their HREELS data.[4] The saturation coverage differs from the value of 0.83 implied by Chin *et al.*'s [12, 13] data for C(111), and the significance of the difference is discussed in section 2.5.3. Table 2.1 compares the saturation coverages implied by previous experiments to that obtained by NRA.

---

[4] During NRA the sample was cooling subsequent to exposure, and the sample temperature was decreasing between 285° and 40°C.

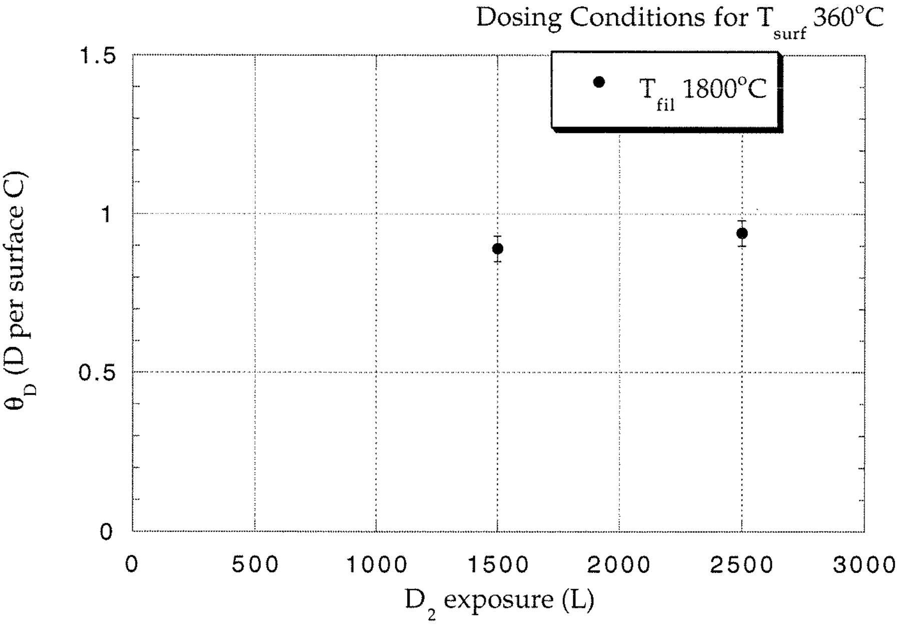

Figure 2.4: Deuterium coverage as a function of exposure at a filament temperature of 1800°C and a surface temperature of 360°C. Each point represents an independent experiment. The sample was not annealed after exposure. The error bars represent the resolution in the coverage measurement. For example, a total of 697 events were detected in the 2500L case. The error due to the number of events counted was greater than the error in the calibration factor.

Reference	Surface	$T_{surface}$	$T_{filament}$	k_A/k_R	Saturation coverage	
Koleske [11]	poly	500°C	1560°C	0.03 ± 0.01	0.97 ± 0.01	D/surf C
Thoms [10]	poly	80–600	1800	0.05 ± 0.01	0.95 ± 0.01	
NRA	(100)	360	1800	0.06 ± 0.04	0.95 ± 0.04	
Chin [13]	(111)	25–200	1800	$0.20 \pm ?$	$0.83 \pm ?$	H/surf C

Table 2.1: Comparison to coverages implied by previous experiments. The reaction-rate ratios measured by previous experiments were converted into coverages via eq. 2.27.

Thermal desorption

The sample was heated subsequent to dose, and coverages were measured as a function of heating temperature. Results are shown in fig. 2.5. For heating temperatures under 200°C, the sample was heated at a rate of ~10°C/sec and held at the annealing temperature for about 2-5 minutes. Below 200°C the annealing time did not affect coverage. For temperatures over 200°C, the sample was flashed to a temperature of T_{flash} at a rate of ~10°C/sec, and heating was turned off within seconds of attaining T_{flash}. The amount of deuterium desorbed between 470°C and 800°C in fig. 2.5 implies a desorption barrier of 3.0 eV, assuming first-order desorption with a pre-exponential factor of 10^{13}/sec and a heating rate of 10°C/sec. The desorption barrier of 3.0 eV agrees with the barrier of 3.08 eV implied by the temperature-programmed desorption data of Hoffman *et al.* [27] for D_2 desorption and Thomas *et al.* [20] for H_2 desorption. However, any rate parameters calculated from the NRA flashing results are less reliable than those of TPD experiments because the NRA heating rate was not carefully controlled.

Note that 10%±7% of a monolayer desorbs upon heating to ~600–620°C, whereas a negligible amount of deuterium desorbs at temperatures below 450°C. Hoffman *et al.* [27] also detected desorption at 600°C from a plasma-pretreated, undegraded C(100):D sample. Thomas *et al.* [20] found desorption from C(100) at 600°C after ~1000 L hydrogen exposure. However, Thoms *et al.* [10] found negligible desorption at 600°C from polycrystalline diamond. The reason for the discrepancy is unknown. The lower limit of the NRA desorption value, 3% ML, may be within the experimental uncertainty of the HREELS measurement. The HREELS coverages were uncalibrated, and no error bars were reported.[5] It is also possible that the (100) samples contain a small fraction of dihydride sites, yielding low-temperature des-

---

[5] Temperature measurements across experiments using different sample holders and different thermocouple locations are not directly comparable. Other experiments have found imperfect thermal contact to cause temperature variations between a diamond and the sample holder where the thermocouple was located. Smentkowski *et al.* [40] found that a thermocouple attached to the the sample heater registered a temperature up to 200°C greater than one inserted into the diamond sample. In a separate experiment, Thoms *et al.* [19] found thermocouple measurements to be 100–150°C greater than pyrometric measurements at sample temperatures above 1000°C.

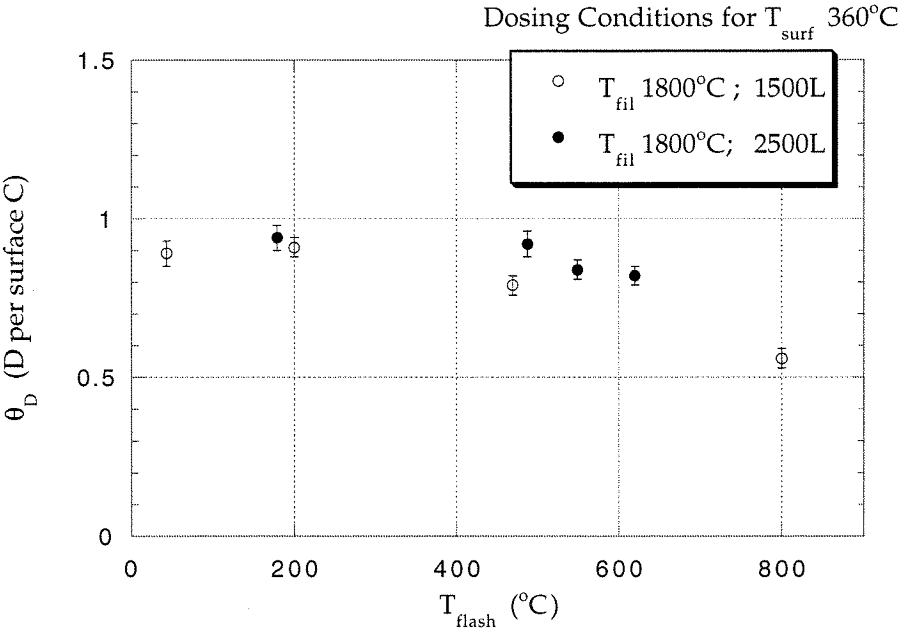

Figure 2.5: Deuterium coverage as a function of flashing temperature subsequent to exposure at a surface temperature of 360°C. The heating rate was appproximately 10°C/sec. The error bars represent the resolution in the coverage measurement.

orption. *Ex-situ* AFM found an upper bound to the surface roughness of the NRA sample, indicating a maximum macroscopic step coverage of ~4%. However, even with 4% dihydride sites, the D coverage of monohydride sites would still lie within the error bars of the measurement, 0.95 ± 0.04 D per dimerized carbon.

2.3.3 Coverage at low surface temperature

Figure 2.6 shows deuterium coverages resulting from dosing at a surface temperature of 80°C and a filament temperature of 1800°C. An exposure of 1500L appears to be sufficient to reach saturation coverage. The coverages at 1500L and 2500L are within the error bars of the corresponding coverages obtained by dosing at a surface temperature of 360°C. Since both of these surface temperatures are low enough for migration and desorption to be inactive, coverage is expected to be insensitive to surface temperature. The HREELS data of Thoms *et al.* [10] also indicate little difference in k_A/k_R between a surface temperature of 80°C and one of 600°C, implying little difference in saturation coverage.

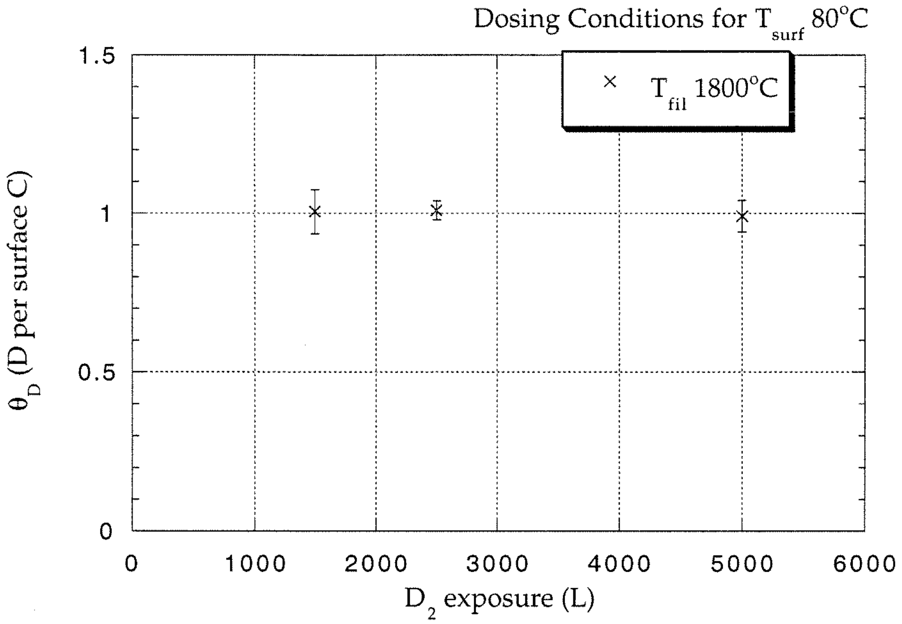

Figure 2.6: Deuterium coverage as a function of exposure at a filament temperature of 1800°C and a surface temperature of 80°C. Each point represents an independent dosing experiment. The sample was annealed at up to 200°C after exposure. The coverages reported are averages of the annealed values. The error bars represent the resolution in the coverage measurement.

One major difference between the 360°C amd 80°C exposures is that the cooling time *prior* to dose is an order of magnitude longer for the latter. The majority of the cooling time is spent between the temperatures of 360°C and 80°C, and during this time the sample is exposed to ~0.9 L of total background gas, based on ion-gauge pressure. Thoms *et al.* [19, 41] cleaned their samples by a similar annealing procedure and found that after cooling to 80°C a small amount of hydrogen was evident on the surface, possibly due to readsorption from the background gas during cooling. However, any hydrogen would be replaced by deuterium during dosing, and the steady-state NRA coverages are not expected to be affected by small initial coverages of hydrogen.[6]

---

[6] If anything, the error bars of the 80°C D coverages fall slightly above the error bars of the 360°C data, indicating no interference to D adsorption by any potential surface-bonded H.

Thermal desorption

After deuterium dosing, the UHV chamber with base pressure of 2×10^{-10} torr was opened to the NRA beamline, whose pressure was about 8×10^{-8} torr. During NRA the sample was sometimes cooled with ℓN_2, and at sample temperatures below ~30°C the deuterium coverage was found to rise. Since the coverage would subsequently decrease upon heating to temperatures less than 200°C, the rise was presumably due to physisorption of D_2O from the gas in the beamline.[7] Derry *et al.* [7] also used a ℓN_2 dewar in their vacuum chamber and sometimes found coverages greater than one D per surface C. The high coverages might also have been caused by physisorption of water.

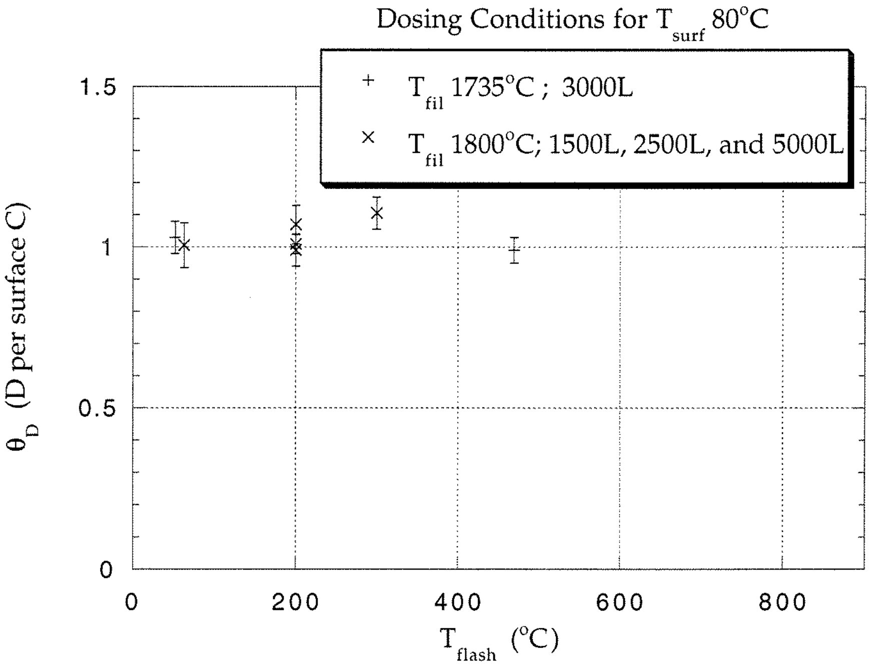

Figure 2.7: Deuterium coverage as a function of flashing temperature subsequent to exposure at a surface temperature of 80°C. The error bars represent the resolution in the coverage measurement due to the limited number of events counted.

To avoid surface contamination subsequent to dose, the sample was heated and coverages were measured as a function of heating temperature. Results are shown

---

[7] Russell [42] has found water to physisorb on diamond at ℓN_2 temperatures and desorb above -93°C.

in fig. 2.7 for heating subsequent to exposures at a surface temperature of 80°C. For heating temperatures under 200°C, the sample was heated at a rate of ~10°C/sec and held at the annealing temperature for about 2-5 minutes. For temperatures over 200°C, the sample was flashed to a temperature of T_{flash} at a rate of ~10°C/sec. Annealing up to 200° did not significantly change coverage, except in cases where the sample was annealed after ℓN_2 cooling. Therefore, little or no D_2O contamination is expected to be physisorbed on the surface in the uncooled cases or in the low-temperature annealed cases, and all data reported herein are for such cases.

2.3.4 Coverage at high filament temperature

Saturation coverages at filament temperatures above 1800°C ranged up to 1.34 ± 0.09 D per surface C. The high coverages might have been caused by surface dihydrides, such as those present on a disordered surface or an ordered (3×1) reconstruction.[8] Since NRA is a nuclear-sensitive technique, it cannot distinguish between mono- and di-hydrides. Although Thoms *et al.* [19] saw no HREELS evidence for dihydrides on C(100) after dosing at a filament temperature of 1800°C, dihydrides may be produced through an activated process at higher filament temperatures. Sakurai and Hagstrum [43] proposed that adsorption of H onto a Si(100) (2×1):H surface breaks the silicon dimer bonds, and Si dimer-bond breakage and etching by exposure to atomic hydrogen have been widely supported by other studies [44, 45]. It is possible that atomic D also breaks carbon dimer bonds on diamond (100). Although bond breakage may be too slow to detect at typical filament temperatures of 1500–1800°C, elevated temperatures may activate the process.

Other possible causes of high deuterium coverage are considered to be less likely. The deuterium doser contains a molybdenum collimation tube behind the hot filament, and radiative heating of the tube increases as the fourth power of the filament temperature. Elements such as C and O are present at the 0.01% (atomic) level in bulk molybdenum [46], and at elevated temperatures C and O can diffuse to the

---

[8] A (3×1) reconstruction cannot be established because no LEED was performed after the high-temperature exposures.

molybdenum surface and desorb as CO. Surface dihydrides may then be produced on the diamond by CO activation of surface dimer bonds. Although very high filament temperatures may activate CO desorption from the molybdenum tube, the flux of CO reaching the sample is negligible. For example, even at a molybdenum temperature of 500°C, less than 0.006 ML of C would desorb from the molybdenum and directly impinge on the sample during the longest dosing times. A previous experiment in the same set-up confirmed negligible oxygen production by the doser by mass-spectroscopic analysis. Outgassing of O (or CO) was detected only after the filament had been heated for several hours at ~2000°C [47]. In the present experiment, all high temperature exposure times were less than 0.2 hr, and O and CO outgassing are expected to be negligible.

Elemental tungsten is also generated at too low of a rate to accumulate in significant amounts on the sample. The vapor pressure of elemental tungsten is greater than 10^{-10} torr above 1900°C, implying a total evaporation at the filament of 0.3 L during the 1975°C exposure and 0.45 L during the 2025°C exposure. However, the flux of tungsten decreases with the square of the distance from the filament. The shape factor describes the decrease in radiative flux from the filament to the diamond, and an upper bound is estimated in section 2.4.3. It is shown that total direct exposure to elemental tungsten is less than 0.0002 monolayers during both deuterium dosing and filament outgassing. Therefore, contamination by elemental tungsten is negligible.

Another possible cause of high deuterium coverage is the presence of molybdenum or tungsten-deuteride on the sample. However, hydrogen has not been reported to etch tungsten [48]. Moreover, *ex-situ* XPS of the sample performed at Caltech subsequent to the NRA experiment showed no evidence for the presence of molybdenum or tungsten. The detection limit was ~0.1% (atomic) W.[9] Therefore, if the sample were in fact contaminated by molybdenum or tungsten-deuteride, any contaminant must have desorbed upon the final 700°C anneal prior to removal from the NRA chamber.

---

[9] The only elements detected on the diamond surface were C (90.97%±0.10%), O (7.16%±0.10%) and Si (1.87%±0.10%). The composition was calculated from the area of the C(1s), O(1s) and Si(2p) peaks. The source of the oxygen may have been contamination received in transit from the NRA to XPS chambers, and the source of the silicon may have been pump oil in the XPS chamber. The sample was not heated to desorb physisorbed contaminants prior to XPS.

A fourth possible cause of high coverage, macroscopic surface roughness, is precluded by *ex-situ* atomic-force microscopy (AFM). Detected roughness levels were too low to produce excess coverages of 0.3 D per surface C. Fig. 2.8 shows AFM images of regular grooves spaced approximately 330 Å apart and about 4 Å high. These measurements were performed at room temperature in contact mode in an atmospheric AFM (Digital Instruments Nanoscope® III). The AFM measurements were taken at Caltech subsequent to the NRA experiment.

Fig. 2.9 shows a flat surface of mica scanned at the same rate (5 Hz) as the diamond sample. No smoothing was performed on either image. The fact that the local roughness (or noise) in the mica image is similar to the roughness in the diamond image demonstrates that the atomic-scale roughness of the diamond is below the detection limit of the AFM. The absence of regular grooves in the mica image demonstrates that the diamond grooves are not an artifact of the imaging process. Diamond grooves were found at all scan rates used and at all locations scanned. The spacing of the grooves ranged between 330 and 450 Å, and the apparent peak-to-valley height ranged up to 14 Å at the highest scan rate.

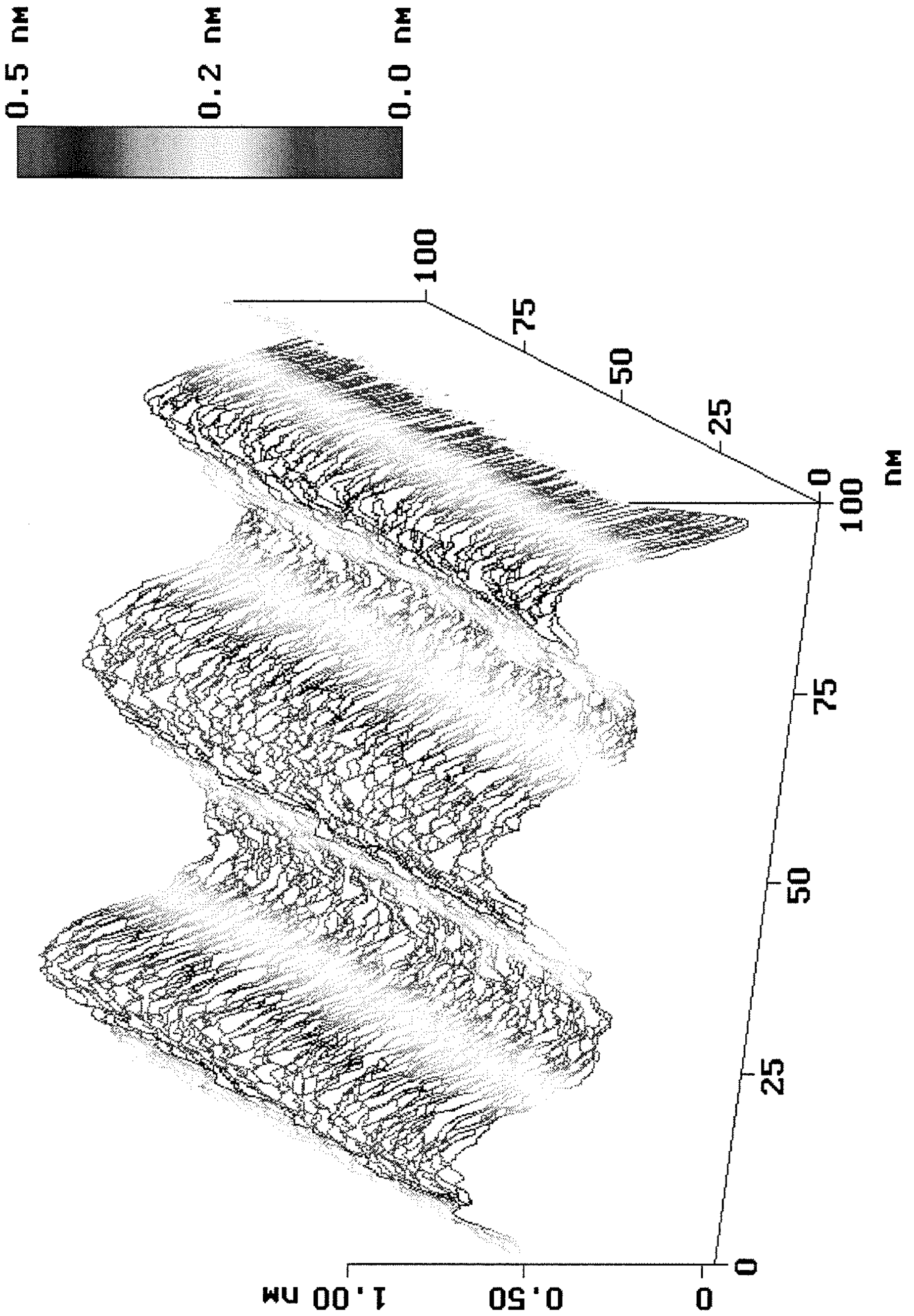

Figure 2.8: AFM image of diamond sample subsequent to NRA experiment. The image is slightly distorted between x = 75 and 100 nm due to the reversal of the tip's direction of travel during the scan(fig. 2.9).

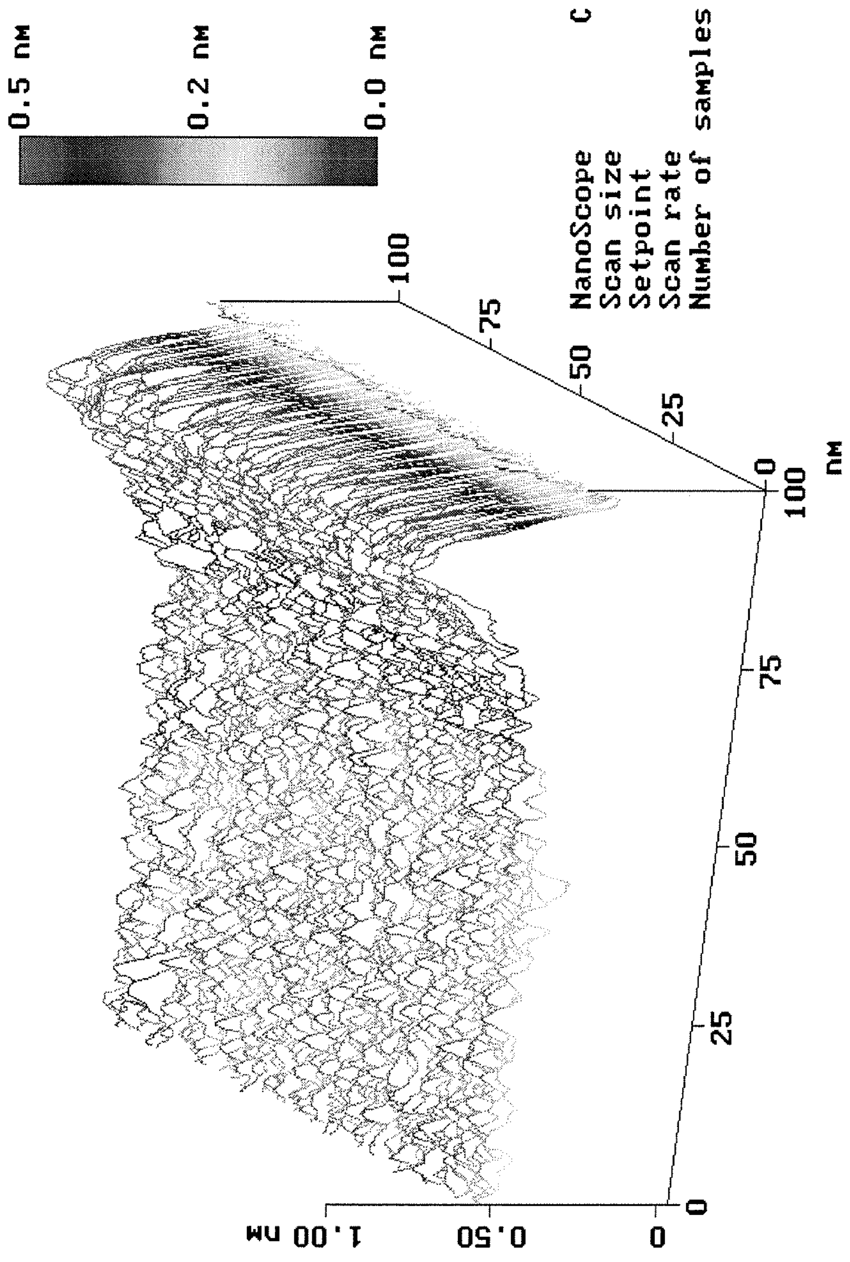

Figure 2.9: AFM image of mica. The absence of regular grooves in the mica image demonstrates that the grooves in the diamond image are not an artifact of the scanning process. The bump at the end of the mica scan is an artifact of reversing the tip's direction of travel during the scan. The location of the bump changes with the location of the end of the scan. The actual mica sample is flat between x = 75 and 100 nm.

Thermal desorption

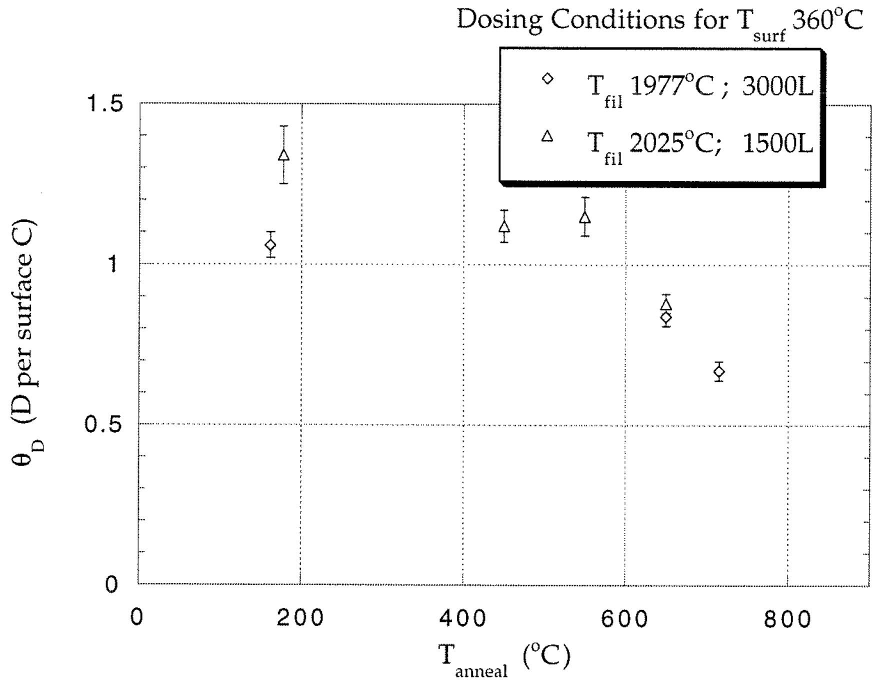

Figure 2.10: Deuterium coverage as a function of annealing temperature subsequent to exposure at a surface temperature of 360°C. The error bars represent the resolution in the coverage measurement.

Fig. 2.10 shows coverage as a function of annealing temperature subsequent to dose. The sample was heated at a rate of approximately 10°C/sec, and to minimize the effect of variations in heating rate, the sample was held at the annealing temperature for 2-2.5 minutes. Holding the sample at the annealing temperature allows better equilibration between the thermocouple and the sample and more accurate measurement of temperature-time history. Therefore, these desorption measurements are more reliable than those performed by flashing the sample in section 2.3.2. The highest three anneals imply an average activation barrier of 2.9 eV, assuming first order desorption and a preexponential factor of 10^{13}/sec. The barrier does not differ significantly from the value of 3.0 eV implied by the exposures at T_{fil} of 1800°C, where the barrier calculation is less accurate due to the shorter anneal times (~1 sec).

2.4 Analysis of deuterium coverage

2.4.1 Subsurface deuterium signal

Since the resonance producing the nuclear reaction is broad [49, fig. A11.23, p. 568], NRA suffers from large sampling depth. The incident ^{3}He$^+$ energy drops from 0.70 to 0.37 MeV before the nuclear-reaction cross section drops to half its peak value. Taking an average stopping power of 37 eV/(10^{15} atoms/cm^2) [50], the ion travels 6750 Å through the diamond before losing 0.33 MeV. Therefore, in addition to the surface deuterium, the spectra integrate over the top 6750 Å of bulk deuterium. A rough upper bound for the subsurface deuterium content in natural diamond may be estimated from the measurements of Sellschop *et al.* [51]. Although their technique suffers from poor depth resolution, their results imply an upper bound of about 31 monolayers of bulk hydrogen in the top 6750 Å. The upper bound for the deuterium content is then 31 times the isotopic abundance of 1.5×10^{-4} [52], or about 0.005 D per surface C.

Subsequent experiments on CVD diamond gave a more exact estimate of subsurface deuterium content. In the case of homoepitaxial diamond (100), the experiment of Appendix A estimated the H content to be 0.30 H per surface C in the top 6750 Å. The deuterium content in the top 6750 Å was estimated to be 0.003 D per surface C. In the case of polycrystalline CVD diamond, Dollinger *et al.* [9] detected less than 10^{-3} hydrogen content below the top 10-20 Å, with a depth resolution of 10 Å. Therefore, the hydrogen content in the first layers below the surface may be approximated to be the same as that in the bulk. The total subsurface deuterium content in the top 6750 Å of the Dollinger sample is then less than 7.6 monolayers times the isotopic abundance [52], or 0.0011 D per surface C. Therefore, the total contribution of subsurface deuterium to the NRA spectra is taken to be 0.0011 D per surface C.

The lower detection limit of the NRA system is determined by the background cosmic radiation incident on the detectors. For beam parameters typical to this experiment, our lower detection limit is 0.013 D per surface C. When compared to the lower detection limit, subsurface deuterium contributes negligibly to the surface deuterium spectrum.

2.4.2 Subsurface deuterium diffusion

NRA spectra showed negligible increases in D coverage between 1500 and 5000L exposures, indicating negligible diffusion or incorporation into the subsurface region during exposure. At filament temperatures below 1975°C, coverages were close to 1.0 D per surface C, consistent with the (2×1):D structure and no subsurface deuterium content. At filament temperatures above 1975°C, coverages ranged up to 1.34 ± 0.09 D per surfcace C, consistent with the (3×1):1.33D structure and no subsurface deuterium content. Therefore, all coverage measurements are consistent with negligible D diffusion from the surface to the subsurface region, and no such diffusion is expected. Smentkowski *et al.* [40] recently suggested deuterium penetration into the subsurface region as one possible cause of sharpening of the C1s transition in XPS data. However, the NRA measurements show no direct evidence for subsurface diffusion.

2.4.3 Negligibility of elemental tungsten exposure

Although the vapor pressure of W becomes significant ($> 1\times10^{-10}$torr) above 1900°C, the flux of W at the sample is negligible. Figure 2.11 shows an upper bound for the direct W exposure at the sample during outgassing prior to dosing, and fig. 2.12 shows the estimated direct W exposure during dosing. Exposures were estimated via the equation

$$\varepsilon_{\mathrm{W}} = \Gamma_{\mathrm{W}@dia} t = \frac{\frac{A_{fil}}{A_{dia}} F_{fd} P_{\mathrm{W}}(T_f)}{\sqrt{2\pi m_{\mathrm{W}} k T_f}} t, \tag{2.1}$$

where ε_{W} is the total elemental W exposure, $\Gamma_{\mathrm{W}@dia}$ is the elemental W flux at the diamond, t is the exposure time,[10] A_{fil} and A_{dia} are the tungsten and diamond surface areas, respectively, F_{fd} is the shape factor, $P_{\mathrm{W}}(T_f)$ is the vapor pressure of elemental

---

[10] Exposure times prior to dosing are taken to be 1020 s, the maximum sample cooling time between flashing and dosing, below the filament outgassing temperature (T_f = 2200°C) and 360 s, the maximum filament outgassing time, at the outgassing temperature. Exposure times during dosing are the maximum dose times: 600 s at 1735°C, 1000 s at 1800°C, 600 s at 1977°C, and 300 s at 2025°C.

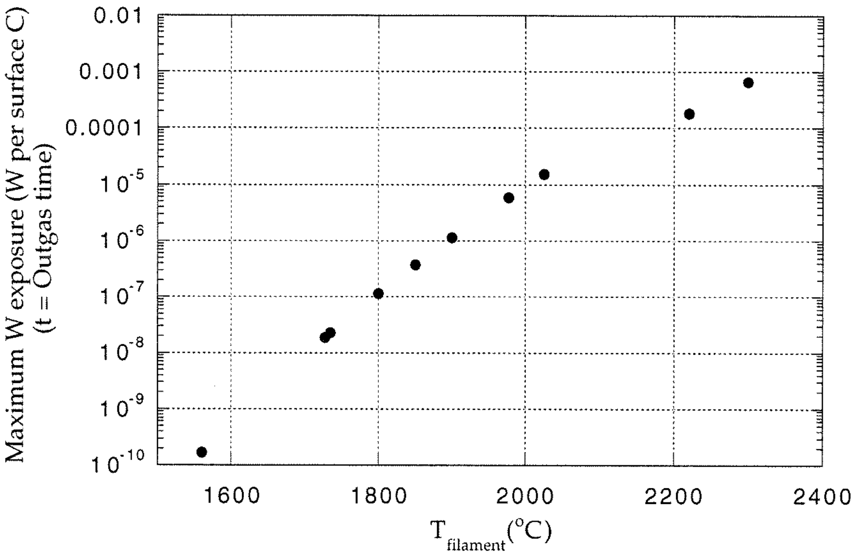

Figure 2.11: Estimated direct elemental W exposure of *back* side of sample prior to dosing. The front side of the sample was out of line-of-sight of the doser, and thus received an even lower exposure.

tungsten at filament temperature T_f, m_{W} is the mass of W, and k is the Boltzmann constant.

The factor $\frac{A_{fil}}{A_{dia}}F_{fd}$ accounts for the decrease in direct radiative flux from the filament surface to the diamond location. The exact shape factor is difficult to calculate for the case of the NRA doser, with a pancake, spiral-wound filament. However, an upper bound is obtained by treating the filament as a disk of diameter 0.635 cm, the diameter of the doser collimation tube behind the filament. The diamond is treated as a disk 0.5 cm in diameter, parallel to the plane of the filament and 4 cm away for the dosing exposures and 20 cm away for the outgassing exposures. F_{fd} is then 0.0039 for dosing and 0.00016 for outgassing [53, p. 32]. These shape factors are upper bounds for F_{fd}. The actual shape factors may be lower due to the fact that the hot part of the filament occupies less area than the exit of the collimation tube.

W exposures of the back side of the sample during outgas (fig. 2.11) are less than 0.0007 W per surface C, and those of the front side during dose (fig. 2.12) are less than 0.00012 W per surface C. Figure 2.11 shows the exposure of the *back* side of

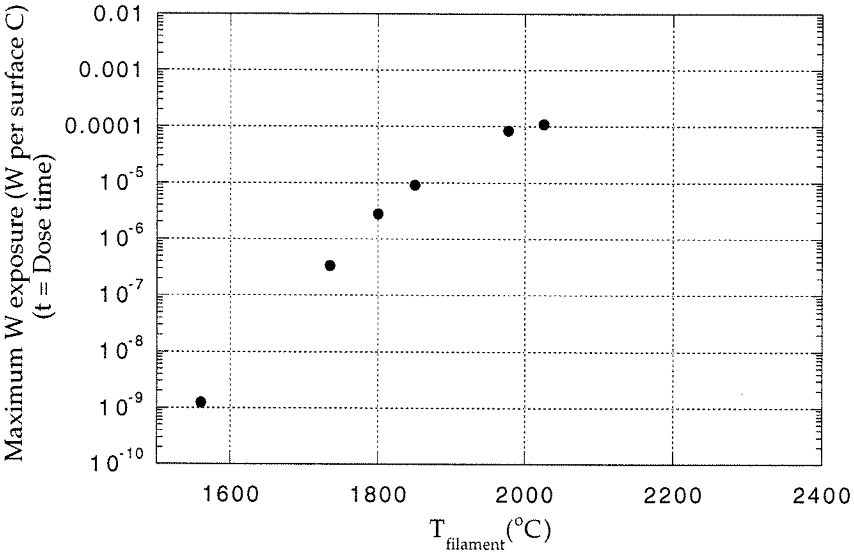

Figure 2.12: Estimated direct elemental W exposure of the sample during dose.

the sample during outgas. The exposure of the front side of the sample is far less. Assuming a C-WD_5 surface moiety, direct W contamination during dose accounts for less than 0.0006 D per surface C. Therefore, contamination by elemental tungsten is negligible during both outgassing and dosing.

2.4.4 Estimated atomic deuterium flux during dosing

The atomic deuterium flux incident on the sample was not measured. In the absence of a calibration, a very rough estimate may be obtained by considering the flux at the filament surface. The flux of atomic deuterium out of the filament is given by

$$\Gamma_{\mathrm{D_{out@fil}}} = 2 s_m P_a \Gamma_{\mathrm{D_{2inc@fil}}} , \tag{2.2}$$

where s_m is the sticking coefficient of D_2 on the tungsten, P_a is the atomization probability, and $\Gamma_{\mathrm{D_{2inc@fil}}}$ is the flux of D_2 incident on the filament.

In steady-state mass flow, the flux of D_2 out of the filament is determined by the difference between the incident D_2 flux and the outgoing D flux,

$$\Gamma_{\mathrm{D}_{2\mathrm{out@fil}}} = s_m \Gamma_{\mathrm{D}_{2\mathrm{inc@fil}}} - \tfrac{1}{2}\Gamma_{\mathrm{D}_{\mathrm{out@fil}}} \tag{2.3}$$

Atomic and molecular deuterium desorb from the filament in their equilibrium ratio given by eq. 2.37,

$$\frac{\Gamma_{\mathrm{D}_{\mathrm{out@fil}}}}{\Gamma_{\mathrm{D}_{2\mathrm{out@fil}}}} = \sqrt{\frac{m_D}{m_{D_2}}} \frac{\sqrt{1+4\frac{P}{P_0K}}-1}{2\frac{P}{P_0K}-\sqrt{1+4\frac{P}{P_0K}}+1}. \tag{2.4}$$

Combining these three equations, one obtains

$$\Gamma_{\mathrm{D}_{\mathrm{out@fil}}} = s_m \frac{\sqrt{\frac{m_{D_2}}{m_D}}}{\left(4/\sqrt{(\frac{P_0}{P}K)^2+4\frac{P_0}{P}K}-\frac{P_0}{P}K\right)+\sqrt{\frac{m_{D_2}}{m_D}}-2} \times \frac{P}{\sqrt{2\pi m_{D_2} k T_{\mathrm{inc@fil}}}}, \tag{2.5}$$

where $T_{\mathrm{inc@fil}}$ is the temperature of the deuterium incident on the filament, 25°C. The sticking coefficient, s_m, is estimated to be 0.3 at 2300°C [54] and is assumed to be temperature-independent [55].

The deuterium flux directly incident at the diamond is lower than that emitted at the filament by the shape factor, F_{fd}, and the exposed area ratio, A_{fil}/A_{dia},

$$\Gamma_{\mathrm{D}_{\mathrm{inc@dia}}} = \frac{A_{fil}}{A_{dia}} F_{fd} \Gamma_{\mathrm{D}_{\mathrm{out@fil}}}. \tag{2.6}$$

The shape factor may be roughly estimated, as in section 2.4.3, by treating the filament as a disk of 0.635 cm diameter and the diamond as a disk 0.5 cm in diameter, parallel to the filament and 4 cm away. F_{fd} is then approximately 0.004 [53, p. 32].

Table 2.2 estimates $\Gamma_{\mathrm{D}_{\mathrm{inc@dia}}}$ from the shape factor and eqs. 2.5 and 2.6. All exposures are on the order of 10 D per surface C, indicating a D flux sufficient to obtain monolayer coverages with a reasonable sticking coefficient of atomic deuterium on bare diamond. The D exposures given in table 2.2 are intended to check the sufficiency of dosing and should in no way be taken as an accurate estimate of the actual D exposure. Accurate D flux can be measured by installing a differentially-

Rough order-of-magnitude estimates for D flux and exposure

$P_{D_{2inc@fil}}$ [a] torr	T_{fil} °C	$\Gamma_{D_{inc@dia}}$ ML/s	$t_{exposure}$ s	$D_{exposure}$ ML
1×10^{-5}	1735	2.40×10^{-2}	600	14
	1800	2.41	1000	24
	1975	2.42	600	15
	2025	2.42	300	7

[a] Pressure of D_2 at room temperature incident on filament, corrected for an ion gauge sensitivity to D_2 of 0.5 [56]. Ion gauge pressure was 5×10^{-6} torr.

Table 2.2: Very rough estimate of D exposure. One monolayer (ML) is defined to be 1 D per surface C, or 1.566×10^{15}D/cm^2.

pumped mass spectrometer at the location of the diamond, with a beam chopper to distinguish between deuterium desorbing directly from the filament and background deuterium bouncing off the chamber walls.

2.4.5 Proposed effect of dosing on dihydrides and degradation

Coverages up to 1.34±0.09 D per surface C were found at filament temperatures *circa* 2000°C, indicating the possibility of surface dihydride generation. Surface dihydrides are proposed to form at high filament temperature through breakage of dimer bonds by hot atomic deuterium. Sakurai and Hagstrum [43] proposed that adsorption of H onto a Si(100) (2×1):H surface breaks the silicon dimer bonds, and dimer bond breakage and etching of silicon surfaces by atomic hydrogen has been supported by many studies [44, 45]. Although bond breakage may be slow at typical filament temperatures of 1500–1800°C, elevated temperatures may activate the process.

The results of several previous experiments are consistent with dimer-bond breakage during dosing. Lee and Apai [17] found that a polished (100) (2×1) surface converted to a (1×1) structure upon atomic hydrogen dosing.[11] Heating the sample

---

[11] The filament temperature was not reported, and the sample temperature during dosing was not specified.

to ~1200°C desorbed hydrogen and restored the (2×1) pattern, and the adsorption–desorption process was completely reversible. To destroy the (2×1) reconstruction, it is necessary to break carbon–carbon bonds, and on terraces, dimer bonds, being the most strained, are likely to be among the first to be broken. Lee and Apai suggested the conversion of C–C bonds to C–H bonds, eventually leading to CH_4. Sun *et al.* [57] dosed a (100)-facetted polycrystalline sample at 2000°C filament temperature in 10^{-6} torr D_2. They interpreted their on-specular HREEL spectra to indicate surface monohydrides and dihydrides and suggested H breakage of dimer bonds. However, dipole selection rules were used when interpreting the spectra, and Thoms *et al.* [22] later demonstrated that dipoe selection rules are not applicable on the smooth C(100):H surface.

Hamza *et al.* [18] also found that a polished C(100) (2×1) surface converted to a (1×1) structure upon dosing. Again, this can be caused by dimer-bond breakage. The filament temperature and dosing time were not reported. Pate found atomic hydrogen dosing to convert the (2×1) surface to a (1×1) structure at a filament temperature of 1800°C. Subsequent annealing did not restore the (2×1) LEED pattern, and Pate suggested etching or roughening of the surface by the single adsorption–desorption cycle. Dimer-bond breakage is consistent with all of these findings.

Filament temperature is not the only factor determining whether evidence of C–C bond scission will be seen. Once broken by adsorption of hydrogen, dimer bonds may be subsequently restored by thermal desorption of the hydrogen, freeing the carbon electrons to re-pair. Since surface temperature determines desorption rate, it is a second factor affecting whether C–C scission is detected. Although Pate saw indications of bond breakage on C(111) at 1800°C, Chin *et al.* [13] found no such indications when dosing at the same filament temperature. However, Pate's surface temperature was $\leq$ 100°C, and Chin *et al.*'s was 800–850°C during dose. In a separate experiment, Chin *et al.* [13] found surface CH_3 species to desorb upon annealing to 400°C. It is possible that Pate's low surface temperature stabilized di- and trihydrides, preventing reformation of C–C bonds after scission. At surface temperatures below 200°C, Chin *et al.* found repeated adsorption–desorption cycles to degrade the surface. The CH stretch peaks in the SFG spectra broadened, and other (unspecified) hydrocarbon features appeared in the spectra, consistent with C–C bond scission and the stabilization of broken bonds by formation of di- or tri-hydrides. Dosing at 800–850°C was found to completely regenerate the surface, consistent with the desorption of di- and tri-hydrides and destabilization of broken C–C bonds. Since surface temperature determines desorption rate, it must be considered in addition to filament temperature when searching for evidence of dihydride formation through dimer-bond scission.

Indications of thermal desorption from dihydride sites on the C(100) surface have been found by TPD. Yang *et al.* [5] found a low-temperature shoulder in the thermal desorption peak and suggested desorption from dihydride sites by analogy with Si(100). Hoffman *et al.* [27] found a peak at 710°C and one at 900°C. Therefore, dihydride desorption may occur when dosing the sample at medium surface temperature, restoring broken C–C bonds.

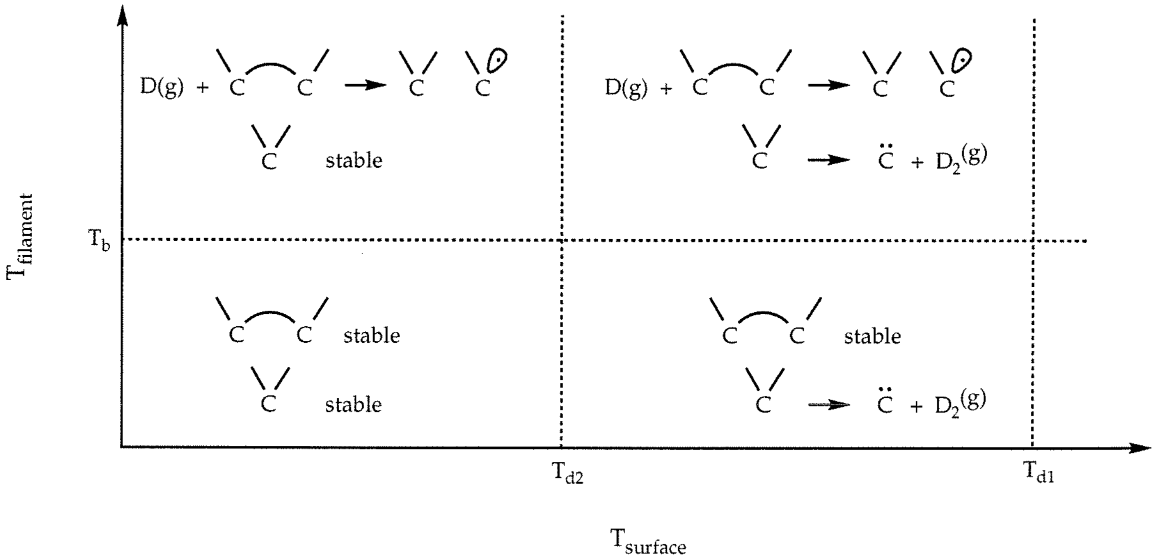

Figure 2.13: Proposed effect of $T_{filament}$ and $T_{surface}$ on dimer breakage and hydrogen desorption from dihydride sites.

Figure 2.13 shows the proposed effect of the filament and sample temperatures on surface sites during dosing. The reactions of abstraction and recombination with unsaturated sites are omitted for clarity. Four temperature regimes are shown, with T_{d1} and T_{d2} being the temperatures at which H_2 desorbs from monohydride and dihydride sites, respectively. Significant thermal desorption begins when the dosing time reaches the characteristic thermal desorption time, i. e.,

$$t_{dose}^{-1} = A_{d2} e^{-E_{d2}/kT_{surf}}, \tag{2.7}$$

where t_{dose} is the dosing time, T_{surf} is the surface temperature during dosing, and A_{d2} and E_{d2} are the pre-exponential factor and barrier, respectively, to thermal desorption from dihydride sites. Dihydride desorption parameters have not been measured on (100), but parameters have recently been caculated for a low-temperature peak on C(111) [28]. For a dosing time of 1000 sec, these give a T_{d2} of ~630°C.

The filament temperature at which dimer-bond breakage becomes active, T_b, is determined by the dosing time and hydrogen flux. Assuming dimer bond breakage proceeds via

$$\mathrm{D}^{\mathrm{gas}} + \mathrm{DC{-}CD}^{\mathrm{surf}} \xrightarrow{k_b} \mathrm{CD}_2^{\mathrm{surf}} + \cdot\mathrm{CD}^{\mathrm{surf}}, \tag{2.8}$$

the rate of change of dimer coverage is given by

$$\frac{d\theta_{DC-CD}}{dt} = -\sigma_b \Gamma_{\mathrm{D}} \theta_{DC-CD}. \tag{2.9}$$

Here θ_{DC-CD} is the number of monohydride dimerized surface carbons per surface C, σ_b is the total dimer-scission reaction cross-section, and Γ_{D} is the flux of atomic deuterium incident on the surface. The number of dimer breakage events during dose becomes significant when the dosing time is equal to the characteristic time, $t_{dose} = 1/(\sigma_b \Gamma_{\mathrm{D}})$.[12] Higher filament temperatures will give higher σ_b and Γ_{D} and therefore shorter dosing times to dimer breakage. Therefore, two experiments using

---

[12] Assuming $k_b = A_b e^{-E_b/kT_{fil}}$, the characteristic temperature, T_b, is determined by the transcen-

the same filament and surface temperatures may obtain conflicting results if one of them is dosing for long enough or at a high enough flux to break a significant number of dimer bonds while the other is not.

Surface roughness also affects the time to attain significant dimer breakage. Polished surfaces typically have smaller terrace domains than hydrogen-plasma treated samples, and therefore fewer dimer bonds must be broken in order to have a significant effect on the LEED pattern. However, polishing roughness can be compensated for by decreasing the filament temperature. Thomas *et al.* [20] found polished (100) to remain in the (2×1) state even after 4×10^4 L exposure to H_2. The filament temperature was 1500°C, and the rate of dimer breakage at this temperature may be too slow to affect the LEED pattern within the dosing time. Polishing roughness can also be compensated for by increasing the surface temperature during dose. Employing dosing parameters within the (medium surface temperature, low filament temperature) region of fig. 2.13 allows surface dihydrides to desorb faster than they are formed by dimer breakage.

Hydrogen-plasma pretreatment is recommended for studying dimerized monohydride sites. Thoms *et al.* [19] saw no HREELS evidence for dihydride production on C(100) (2×1) after dosing at a filament temperature of 1800°C. Spectral interpretation was reliable in that it did not assume any dipole selection rules. The rate of dimer production is therefore small at 1800°C for their dosing flux.

Hydrogen reactions with dimerized sites may be characterized by choosing dosing parameters in the lower left quadrant of fig. 2.13. However, long dosing times bring T_b down and eventually result in dimer scission. Dosing at higher surface temperatures, in the lower right quadrant, is recommended for dynamically restoring broken bonds by desorbing from dihydrides. Dosing in the upper left quadrant is recommended for studying dimer breakage, as this preserves evidence of C–C bond scission by precluding desorption from dihydrides. Dosing above the monodydride desorption

---

dental equation

$$e^{E_b/k\mathrm{T}_b} = \sqrt{\frac{2\pi m_D}{kT_b}}\,\Gamma_{\mathrm{D}} A_b t_{dose}. \tag{2.10}$$

temperature may allow a disordered surface to be restored to a (2×1) reconstruction by reorganizing the dimer rows. These hypotheses may be tested by performing SFG on C(100) under various dosing conditions and observing the effect on CH_2 symmetric and antisymmetric and CH stretch signals. SFG has the resolution to distinguish these peaks, and because it is based on a process that is symmetry-forbidden in the bulk, SFG has excellent surface sensitivity.

In summary, the following interpretation of degradation is suggested. Degradation is the result of a dynamic competition between two processes: C–C bond breakage by insertion of atomic hydrogen from the gas phase, and C–C bond restoration initialized by desorption of molecular hydrogen from the dihydride C. If the rate of dimer bond breakage exceeds the rate of reformation, then the surface degrades and the (2×1) LEED pattern is eventually destroyed. The rate of dimer bond breakage is expected to depend mainly on filament temperature, flux of atomic hydrogen to the surface, and coverage of DC–CD sites. The rate of dimer bond reformation is expected to be limited by the rate of hydrogen desorption from the dihydride site, controlled by surface temperature. This interpretation is consistent with the NRA measurements of high deuterium coverage at high filament temperature, the findings of Lee and Apai [17] that the (2×1) LEED pattern can be destroyed by exposure to atomic hydrogen, the findings of Chin *et al.* [13] that the surface eventually degrades after low-surface-temperature exposures and is regenerated by high-surface-temperature exposures, and the findings of Hoffman [28] that low-surface-temperature exposures result in multiple peaks in thermal desorption spectra while 800°C exposures result in single desorption peaks.

2.5 Analysis of reaction-rate ratio

2.5.1 Relationship between surface coverage and gas-surface reaction rates

Total deuterium coverage is determined by the reaction of gas-phase atomic deuterium with the diamond surface. There are three types of sites on a fully reconstructed (100) surface: fully deuterated dimers, $\mathrm{DC{-}CD^{surf}}$, half-deuterated dimers, $\mathrm{DC{-}C{\cdot}^{surf}}$, and pi-bonded dimers, $\mathrm{{\cdot}C{-}C{\cdot}^{surf}}$. Gas-phase atomic deuterium recombines with surface sites and abstracts deuterium from them.

Recombination :

$$\mathrm{D^{gas} + {\cdot}C{-}CD^{surf}} \xrightarrow{k_{Rh}} \mathrm{DC{-}CD^{surf}} \tag{2.11}$$

$$\mathrm{D^{gas} + {\cdot}C{-}C{\cdot}^{surf}} \xrightarrow{k_{Rp}} \mathrm{DC{-}C{\cdot}^{surf}} \tag{2.12}$$

Abstraction :

$$\mathrm{D^{gas} + DC{-}CD^{surf}} \underset{k_{-Af}}{\overset{k_{Af}}{\rightleftharpoons}} \mathrm{D_2^{gas} + {\cdot}C{-}CD^{surf}} \tag{2.13}$$

$$\mathrm{D^{gas} + DC{-}C{\cdot}^{surf}} \underset{k_{-Ah}}{\overset{k_{Ah}}{\rightleftharpoons}} \mathrm{D_2^{gas} + {\cdot}C{-}C{\cdot}^{surf}} \tag{2.14}$$

In addition, chemisorbed deuterium migrates from surface site to surface site and is thermally desorbed.

Migration :

$$\mathrm{DC{-}CD^{surf} + {\cdot}C{-}CD^{surf}} \underset{k_{-Mfh}}{\overset{k_{Mfh}}{\rightleftharpoons}} \mathrm{DC{-}C{\cdot}^{surf} + DC{-}CD^{surf}} \tag{2.15}$$

$$\mathrm{DC{-}CD^{surf} + {\cdot}C{-}C{\cdot}^{surf}} \underset{k_{-Mfp}}{\overset{k_{Mfp}}{\rightleftharpoons}} \mathrm{DC{-}C{\cdot}^{surf} + DC{-}C{\cdot}^{surf}} \tag{2.16}$$

$$\mathrm{{\cdot}C{-}CD^{surf} + {\cdot}C{-}CD^{surf}} \underset{k_{-Mhh}}{\overset{k_{Mhh}}{\rightleftharpoons}} \mathrm{{\cdot}C{-}C{\cdot}^{surf} + DC{-}CD^{surf}} \tag{2.17}$$

$$\mathrm{{\cdot}C{-}CD^{surf} + {\cdot}C{-}C{\cdot}^{surf}} \underset{k_{-Mhp}}{\overset{k_{Mhp}}{\rightleftharpoons}} \mathrm{{\cdot}C{-}C{\cdot}^{surf} + DC{-}C{\cdot}^{surf}} \tag{2.18}$$

Desorption :

$$\mathrm{DC{-}CD^{surf}} \underset{k_{-Df}}{\overset{k_{Df}}{\rightleftharpoons}} \mathrm{\cdot C{-}C\cdot^{surf}} + \mathrm{D_2^{gas}} \tag{2.19}$$

Summing the rate equations for reactions 2.11 through 2.19, one obtains

$$\begin{aligned} \frac{d\theta_D}{dt} &= \frac{d\theta_{D-D}}{dt} + \frac{1}{2}\left(\frac{d\theta_{D-*}}{dt} + \frac{d\theta_{*-D}}{dt}\right) && (2.20) \\ &= \{k_{Rp}\theta_{*-*} + \frac{1}{2}k_{Rh}\left(\theta_{D-*} + \theta_{*-D}\right)\}\Gamma_{\mathrm{D}} && (2.21) \\ &\quad +\{k_{-Ah}\theta_{*-*} + \frac{1}{2}k_{-Af}\left(\theta_{D-*} + \theta_{*-D}\right)\}\Gamma_{\mathrm{D_2}} \\ &\quad -\{k_{Af}\theta_{D-D} + \frac{1}{2}k_{Ah}\left(\theta_{D-*} + \theta_{*-D}\right)\}\Gamma_{\mathrm{D}} - k_{Df}\theta_{D-D}, \end{aligned}$$

where θ_D is the number of deuterium per surface carbon, θ_{D-D} is the number of fully-deuterated dimers per pair of surface carbons, θ_{D-*} is the number of half-deuterated dimers per pair, θ_{*-*} is the number of pi-bonded dimers per pair of surface carbons, Γ_{D} is the atomic deuterium flux at the sample surface, $\Gamma_{\mathrm{D_2}}$ is the molecular deuterium flux, and k_{xx} is the total reaction cross section, or the rate constant expressed in terms of (1/flux/time).

Note that all surface migration terms have cancelled out of eq. 2.21. Surface migration conserves total deuterium coverage as it redistributes deuterium among the various surface sites. Migration affects overall coverage only indirectly, by determining the balance between θ_{D-D}, θ_{D-*}, and θ_{*-*} and by producing DC−CD$^{\mathrm{surf}}$ sites for thermal desorption. For example, migration tends to convert half-deuterated dimers into pi-bonded dimers, weighting the k_{Rp} term more heavily than the k_{Rh} term in the first line of eq. 2.21. The balance between θ_{D-D}, θ_{D-*}, and θ_{*-*} affects total coverage because the rates of abstraction and recombination are expected to vary with surface site. For example, Dawnkaski *et al.* [58] estimated the probability for recombination with a π-bonded site to be 1.7 times that for recombination with an isolated radical site.[13]

Writing eq. 2.21 in terms of average rate constants and overall coverages,

$$\frac{d\theta_D}{dt} = k_R\theta_*\Gamma_{\mathrm{D}} + k_{-A}\theta_*\Gamma_{\mathrm{D}_2} - k_A\theta_D\Gamma_{\mathrm{D}} - k_{Df}\theta_{D-D}, \tag{2.22}$$

where θ_* is the number of unsaturated bonds per surface carbon and

$$k_R \equiv \frac{k_{Rp}\theta_{*-*} + \frac{1}{2}k_{Rh}\left(\theta_{D-*} + \theta_{*-D}\right)}{\theta_{*-*} + \frac{1}{2}\left(\theta_{D-*} + \theta_{*-D}\right)}, \tag{2.23}$$

$$k_{-A} \equiv \frac{k_{-Ah}\theta_{*-*} + \frac{1}{2}k_{-Af}\left(\theta_{D-*} + \theta_{*-D}\right)}{\theta_{*-*} + \frac{1}{2}\left(\theta_{D-*} + \theta_{*-D}\right)}, \tag{2.24}$$

and

$$k_A \equiv \frac{k_{Af}\theta_{D-D} + \frac{1}{2}k_{Ah}\left(\theta_{D-*} + \theta_{*-D}\right)}{\theta_{D-D} + \frac{1}{2}\left(\theta_{D-*} + \theta_{*-D}\right)}. \tag{2.25}$$

Since no study has detected thermal desorption below a surface temperature of 450°C, the desorption term in eq. 2.22 may be neglected. For a fully-dimerized surface $\theta_* = 1 - \theta_D$. In steady state, the left hand side of eq. 2.22 is zero, and the steady-state coverage, θ_f is

$$\theta_f = \frac{k_R\Gamma_{\mathrm{D}} + k_{-A}\Gamma_{\mathrm{D}_2}}{\left(k_R + k_A\right)\Gamma_{\mathrm{D}} - k_{-A}\Gamma_{\mathrm{D}_2}}. \tag{2.26}$$

As discussed in section 2.5.2, the mole fraction of $\mathrm{D}^{\mathrm{gas}}$ is likely to be large enough

---

[13] These probabilities were calculated at 1527°C, with the surface temperature equal to the gas temperature, from molecular dynamics simulations using the Brenner potential [59].

for $\Gamma_{\mathrm{D}}/\Gamma_{\mathrm{D}_2} \gg k_{-A}/k_R$ (or $\sqrt{m_{D_2}/m_D} \times [D^{gas}]/[D_2] \gg k_{-A}/k_R$). Then eq. 2.26 reduces to

$$\theta_f = \frac{1}{1+\frac{k_A}{k_R}} \tag{2.27}$$

Here k_A and k_R are the steady-state site-averaged abstraction and recombination rate constants. Therefore, the steady-state deuterium coverage, θ_f, gives the ratio of the average abstraction rate constant to the average recombination rate constant, where the averages are weighted over all sites present in the steady state on a fully-dimerized surface with negligible thermal desorption.

Deconvolving individual reaction-rate constants

When the site-averaged reaction rates are constant in time, eq. 2.22 may be integrated to give

$$\theta_D = \theta_f + (\theta_0 - \theta_f)e^{-\alpha t}, \tag{2.28}$$

where θ_0 is the initial coverage and α is the decay constant,

$$\alpha = (k_R + k_A)\,\Gamma_{\mathrm{D}} - k_{-A}\Gamma_{\mathrm{D}_2}. \tag{2.29}$$

$$\theta_f = \frac{k_R\Gamma_{\mathrm{D}} + k_{-A}\Gamma_{\mathrm{D}_2}}{(k_R + k_A)\,\Gamma_{\mathrm{D}} - k_{-A}\Gamma_{\mathrm{D}_2}}. \tag{2.30}$$

Once again, as discussed in section 2.5.2, the mole fraction of $\mathrm{D}^{\mathrm{gas}}$ is likely to be large enough for $\Gamma_{\mathrm{D}}/\Gamma_{\mathrm{D}_2} \gg k_{-A}/k_R$ (or $\sqrt{m_{D_2}/m_D} \times [D^{gas}]/[D_2] \gg k_{-A}/k_R$). Then eqs. 2.29 and 2.30 reduce to

$$\alpha = (k_R + k_A)\,\Gamma_{\mathrm{D}}. \tag{2.31}$$

$$\theta_f = \frac{1}{1+\frac{k_A}{k_R}} \tag{2.32}$$

Therefore, the time-rate-of-change of the coverage gives the sum of the abstraction and recombination rate constants times the deuterium flux via eq. 2.31. Measuring θ_f, α, and Γ_{D} would enable the individual values of the average rate constants to be deconvolved from their ratio *when the site-averaged rates do not vary with time.* However, this has yet to be accomplished due to the difficulty of measuring Γ_{D}, absolute atomic deuterium flux [54, 60].

2.5.2 Negligibility of inverse abstraction rates

The assumption $\Gamma_{\mathrm{D}}/\Gamma_{\mathrm{D}_2} \gg k_{-A}/k_R$ in section 2.5.1 amounts to neglecting the inverse abstraction rate relative to the recombination rate. Goodwin [61] has estimated $[\mathrm{D}^{\mathrm{gas}}]/[\mathrm{D}_2]$ (or $\sqrt{m_D/m_{D_2}} \times \Gamma_{\mathrm{D}}/\Gamma_{\mathrm{D}_2}$) to be $\gg k_{-A}/k_R$ under diamond CVD conditions, where $T_g = T_s$. Since deuterium flux was not calibrated and gas-surface reaction rates have not been measured under UHV conditions, where $T_g > T_s$, the ratios $\Gamma_{\mathrm{D}}/\Gamma_{\mathrm{D}_2}$ and k_{-A}/k_R cannot be accurately calculated under the NRA dosing conditions. In the absence of data, a rough estimate is obtained by comparing to tungsten cracking experiments and molecular-dynamics simulations of gas-surface reaction rates.

Low-pressure tungsten cracking experiments [54, 62] found that atomic and molecular hydrogen desorbed from the filament in a ratio consistent with their equilibrium ratio, where the equilibrium constant is determined by the filament temperature and the incident hydrogen pressure. Therefore, the outgoing flux of atomic and molecular deuterium at the filament, $\Gamma_{\mathrm{D}_{\mathrm{out@fil}}}$ and $\Gamma_{\mathrm{D}_{2\mathrm{out@fil}}}$, respectively, may be estimated as

$$\frac{\Gamma_{\mathrm{D}_{\mathrm{out@fil}}}}{\Gamma_{\mathrm{D}_{2\mathrm{out@fil}}}} = \frac{P_{D_{out}}/\sqrt{2\pi m_D k T_f}}{P_{D_{2out}}/\sqrt{2\pi m_{D_2} k T_f}} \tag{2.33}$$

$$= \sqrt{\frac{m_D}{m_{D_2}} \frac{P_{D_{out}}}{P_{D_{2out}}}} \tag{2.34}$$

$$= \sqrt{\frac{m_D}{m_{D_2}} \frac{X_D}{1-X_D}}. \tag{2.35}$$

Here $P_{D_{out}}$ and $P_{D_{2out}}$ are the partial pressures of the desorbing atomic and molecular deuterium, respectively, m_D and m_{D_2} are the atomic and molecular masses, k is the Boltzmann constant, and X_D is the mole fraction of desorbing atomic deuterium. In equilibrium,

$$X_D = \frac{1}{2}\sqrt{(\frac{P_0}{P}K)^2 + 4(\frac{P_0}{P}K)} - \frac{1}{2}\frac{P_0}{P}K, \tag{2.36}$$

where K is the equilibrium constant at the filament temperature and reference pressure, P_0, and P is the pressure of D_2 incident on the filament (5×10^{-6} torr for the NRA dosing conditions). Substituting eq. 2.36 into eq. 2.35 yields

$$\frac{\Gamma_{\mathrm{D_{out@fil}}}}{\Gamma_{\mathrm{D_{2out@fil}}}} = \sqrt{\frac{m_D}{m_{D_2}}}\frac{\sqrt{1+4\frac{P}{P_0K}}-1}{2\frac{P}{P_0K}-\sqrt{1+4\frac{P}{P_0K}}+1}. \tag{2.37}$$

The smallest $\Gamma_{\mathrm{D_{out@fil}}}/\Gamma_{\mathrm{D_{2out@fil}}}$ occurs at the lowest filament temperature, which in the NRA experiment is 1735°C. Woolley *et al.* [63] calculated the equilibrium constant for deuterium dissociation from spectroscopic data and statistical mechanics. They found K at 1727°C and 760 torr to be 2.227×10^{-6}. Substituting these values into eq. 2.37 yields a $\Gamma_{\mathrm{D_{out@fil}}}/\Gamma_{\mathrm{D_{2out@fil}}}$ of 240. Therefore, only a small fraction of the deuterium desorbs from the filament as molecular deuterium, and the NRA experiment probes mainly atomic deuterium reactions with the diamond surface.

The ratio of atomic to molecular deuterium flux incident on the sample, $\Gamma_{\mathrm{D}}/\Gamma_{\mathrm{D_2}}$, is

$$\frac{\Gamma_{\mathrm{D}}}{\Gamma_{\mathrm{D_2}}} = \frac{\Gamma_{\mathrm{D_{out}}} + \Gamma_{\mathrm{D_{wall}}}}{\Gamma_{\mathrm{D_2out}} + \Gamma_{\mathrm{D_2wall}} + \Gamma_{\mathrm{D_2reflected}}}, \tag{2.38}$$

where $\Gamma_{\mathrm{D_{out}}}$ is the atomic deuterium flux impinging on the sample directly from the filament, $\Gamma_{\mathrm{D_{wall}}}$ is the atomic deuterium flux impinging on the sample from the vacuum chamber walls, $\Gamma_{\mathrm{D_2out}}$ is the molecular deuterium flux impinging on the sample directly from the filament, and $\Gamma_{\mathrm{D_2reflected}}$ is the molecular deuterium flux reflected from the filament (not adsorbed and desorbed). The D_2 which does not strike the tungsten filament is at room temperature. Since Ando *et al.* [64] found diamond powder to be unreactive with D_2 below 400°C and since the temperature of the diamond surface is less than 400°C, the rate of reaction of room-temperature D_2 with the diamond may be neglected. Moreover, the temperature of the D_2 reflected from the tungsten is less than 170°C, assuming a thermal accomodation coefficient of 0.07 [54].[14] Therefore, the reactions of $D_{2_{\text{wall}}}$ and $D_{2_{\text{reflected}}}$ with the diamond surface are neglected, yielding

$$\frac{\Gamma_{\mathrm{D}}}{\Gamma_{\mathrm{D}_2}} = \frac{\Gamma_{\mathrm{D_{out}}} + \Gamma_{\mathrm{D_{wall}}}}{\Gamma_{\mathrm{D_{2out}}}} \geq \frac{\Gamma_{\mathrm{D_{out}}}}{\Gamma_{\mathrm{D_{2out}}}}. \tag{2.39}$$

The Γ_{D} incident on the sample is lower than the amount emitted at the filament by the shape factor describing radiative transfer from one to the other. However, since Γ_{D_2} incident on the sample also decreases by the same amount, shape factor is irrelevant to the ratio of fluxes. Therefore,

$$\frac{\Gamma_{\mathrm{D}}}{\Gamma_{\mathrm{D}_2}} \geq \frac{\Gamma_{\mathrm{D_{out}}}}{\Gamma_{\mathrm{D_{2out}}}} = \frac{\Gamma_{\mathrm{D_{out@fil}}}}{\Gamma_{\mathrm{D_{2out@fil}}}} \geq 240. \tag{2.40}$$

k_{-A}/k_R may be estimated by the molecular-dynamics calculations of Dawnkaski *et al.* [58]. At 1527°C $(k_{-A} \times \Gamma_{\mathrm{H}_2})$ varied between 6.5×10^{-6} and $2.3 \times 10^{-3}/\mu\text{s/site}$ at 0.1 torr partial pressure of H_2, depending on the type of surface site. $(k_R \times \Gamma_{\mathrm{H}})$ varied between 0.023 and $0.039/\mu\text{s/site}$ at 18 torr partial pressure of H. Therefore, the maximum site-specific k_{-A}/k_R is

$$\frac{k_{-A}}{k_R} \approx \frac{2.3 \times 10^{-3}}{0.023} \frac{P_{\mathrm{H}}}{P_{\mathrm{H}_2}} \sqrt{\frac{m_{\mathrm{H}_2}}{m_{\mathrm{H}}}} = 7.6 \times 10^{-4} \tag{2.41}$$

where P_H is 0.1 torr and P_{H_2} is 18 torr. These rate constants were calculated assuming gas temperature equal to surface temperature and so are not directly applicable to the NRA conditions, where $T_g > T_s$. Therefore, these rate constants are merely a qualitative estimate of k_{-A}/k_R.

---

[14] Recently, Eenshuistra *et al.* [65] detected vibrationally-excited $H_2(\nu'')$ effusing from a metal oven containing hot filaments. They attribute the excited molecules to atomic H desorbing from the filament and recombining with wall H in an Eley-Rideal reaction. The NRA dosing pressure was two orders of magnitude lower than Eenshuistra *et al.*'s pressure, and the flux of $D_{\text{out@fil}}$ incident on the walls was many times lower in the NRA case due to the larger vacuum chamber. Therefore, the NRA experiment is likely to produce a significantly lower flux of vibrationally-excited D_2. Although its presence cannot be ruled out, in the absence of spectroscopic data, the reaction of vibrationally-hot D_2 is neglected in the present analysis.

Therefore, the best available estimates for Γ_D/Γ_{D_2} ($\geq$240) and k_{-A}/k_R (7.6×10^{-4}) indicate that the assumption $\Gamma_D/\Gamma_{D_2} \gg k_{-A}/k_R$ is likely to be satisfied under NRA dosing conditions. In other words, the inverse abstraction rate may be neglected relative to the recombination rate.

2.5.3 Comparison to reaction rates on C(111)

The deuterium coverage on C(100) saturates at 0.95±0.04, for exposure at a filament temperature of 1800°C and a surface temperature of 360°C. This saturation coverage agrees with the coverage of 0.95±0.01 implied by Thoms *et al.*'s [10] HREELS data on polycrystalline diamond. However, the saturation coverage disagrees with the value of 0.83 implied by Chin *et al.*'s [12, 13] data for C(111). Chin *et al.* estimated coverage by comparing the rate at which atomic hydrogen replaced chemisorbed deuterium on C(111) to the rate at which atomic hydrogen recombined with clean C(111). Although in the NRA experiment atomic deuterium reacted with diamond, the deviation is unlikely to be an isotopic effect; for Chin states that the rate at which atomic deuterium reacted with the diamond surface was similar to the rate at which atomic hydrogen reacted.

The discrepancy is most likely due to a variation between site-specific reaction rates on C(100) and C(111). Dawnkaski *et al.* [58] recently estimated the recombination and abstraction probabilities for several types of sites on the (100) (2×1) surface and the (111) (1×1):0.75H surface from molecular dynamics calculations using the Brenner potential [59]. At 1527°C their reaction probabilities imply a saturation hydrogen coverage of 0.84 for C(100) and 0.70 for C(111).[15] Since Dawnkaski *et al.* assumed a surface temperature equal to the gas temperature, their results are not directly comparable to the experiments, where surface temperature was $\leq$ 360°C and the gas temperature was 1800°C. Nevertheless, their calculations do imply a variation between site-specific reaction rates on C(100) and C(111), one large enough to

---

[15] These coverages were calculated by eq. 2.27 using Dawnkaski *et al.*'s probability for abstraction from the C(100) (2×1):0.94H surface and for recombination at an isolated radical site on the same surface.

Reference	Surface	T_{surface}	T_{filament}	k_A/k_R	Saturation coverage
			Experiment		
Koleske [11]	poly	500°C	1560°C	0.03 ± 0.01	0.97 ± 0.01 D/surf C
Thoms [10]	poly	80–600	1800	0.05 ± 0.01	0.95 ± 0.01
NRA	(100)	360	1800	0.06 ± 0.04	0.95 ± 0.04
Chin [12, 13]	(111)	25–200	1800	$0.20 \pm$?	$0.83 \pm$? H/surf C
		Molecular Dynamics Simulation			
Dawnkaski [58]	(100)	1527°C	1527°C	0.09/0.46	0.84 H/surf C
Dawnkaski [58]	(111)	1527	1527	0.14/0.32	0.70

Table 2.3: Comparison to reaction-rate ratios obtained by previous experiments. Reaction rates are converted into coverages via eq. 2.27. The experimental uncertainty is not specified in the work of Chin *et al.* [12, 13].

qualitatively explain the difference between the experimental saturation coverages of 0.95 ± 0.04 on C(100) and 0.83 on C(111). Results are summarized in table 2.3.

2.5.4 Comparison to reaction rates in growth models

Thoms *et al.* [10] found k_A/k_R to be independent of surface temperature below 600°C, indicating that at temperatures low enough to neglect migration and thermal desorption, filament temperature controls the net rate of reaction on diamond. Abstraction on Si(100) has also been shown to be independent of surface temperature [66]. Although Koleske *et al.* [11] found a slight surface-temperature dependence in k_A, this dependence has a negligible effect on the extrapolation of NRA data, as shown at the end of this section. Therefore, gas temperature is likely to control the rate of reaction with the diamond surface, and filament temperature is used to extrapolate the NRA data down to diamond growth temperatures.

The NRA reaction-rate ratio of 0.06 at 1800°C is extrapolated down to a growth temperature of 927°C by assuming an activation barrier of 7.3 kcal/mol [29, table I]. The resulting ratio is 0.017 at 927°C, compared to a ratio of 0.59 in thermochemical kinetic models of diamond growth on C(100) [29].[16] These reaction rates may be

---

[16] Since the present work expresses reaction-rate constants on a per C–D basis and the thermochemical model expresses rate constants on a per cluster basis, the thermochemical abstraction rates must be divided by the number of equivalent C–H bonds in the cluster to convert to the conventions of the present work. The resulting k_A is that of reactions a, d, and o in ref. [29], or half of the rate

converted to open-site fraction via eq. 2.27 assuming $\theta_* = 1 - \theta_f$. The NRA ratio implies an open-site fraction of 1.6% ± 1.1% at 927°C, whereas the growth model ratio implies an open-site fraction of 37%. Therefore, the extrapolated NRA data indicate that the thermochemical growth model overpredicts the fraction of surface sites available for growth by a factor of ~20.

Molecular dynamics simulations based on the Brenner potential [59] obtain a k_A/k_R consistent with the extrapolated NRA ratio. Dawnkaski *et al.* [58] determined the abstraction and recombination reaction probabilities at various sites on a slab modeling the C(100) surface. The slab contained 3 rows of 3 dimers on the surface and 7 layers in the bulk. At 927°C the ratio of reaction probabilities on half-deuterated dimers gave a k_A/k_R of 0.041.[17] Reaction-rate ratio is converted to coverage via eq. 2.27, and the coverage is converted to open-site fraction by assuming $\theta_* = 1 - \theta_D$. The molecular-dynamics k_A/k_R implies an open-site fraction of 4.0%, in much better agreement with the NRA fraction of 1.6% ± 1.1% than thermochemical kinetic models.

Due to the distance between the filament and the sample, the velocity of the incoming deuterium in the NRA experiment is more predominantly perpendicular to the surface than that of a Maxwell-Boltzmann distribution. Since the abstraction transition state is collinear with (111) [67, 68], the (100) directionality of the NRA deuterium would tend to slightly decrease k_A. Therefore, it is not surprising that the molecular dynamics calculations obtained a higher k_A for a Maxwell-Boltzmann distribution of incoming H velocities.[18] The higher k_A accounts in part for the larger open-site fraction obtained by molecular dynamics simulations.

Table 2.5.4 summarizes the dependence of open-site fraction on the activation barrier to abstraction, E_A. Chang *et al.* [68] determine E_A for a hydrogen bonded to

---

of reaction A in ref. [29]. Likewise, k_R is the rate of reactions b, e, g, n, p, and r in ref. [29].

[17] Since Dawnkaski *et al.* [58] express reaction probability on a per C–H basis, their reaction-rate ratios may be directly compared to those of the present work.

[18] The magnitude of the directionality effect may be estimated by repeating the molecular-dynamics simulations for the NRA conditions. The velocity distribution of the incoming D may be generated by approximating the filament source as a disk ~0.625 cm in diameter, ~4 cm from the sample and parallel to it.

Experiment	E_A (kcal/mol)	k_A/k_R(1800°C)	θ_*(927°C)
Chang *et al.* [68]	10.61	0.06	0.9%
Dawnkaski *et al.* [58]	7.84–9.69		1.1–1.5%
Harris *et al.* [29]	7.30		1.6%
Krasnoperov *et al.* [69]	6.21–7.15		1.7–2.0%

Table 2.4: Effect of activation barrier on the extrapolation of open-site fraction from NRA filament temperature down to diamond-growth temperature.

Experiment	E_A (kcal/mol)	k_A/k_R(1800°C)	θ_*(927°C)
Chang *et al.* [68]	10.61	0.02–0.10	0.3–1.5%
Dawnkaski *et al.* [58]	7.84–9.69		0.4–2.4%
Harris *et al.* [29]	7.30		0.5–2.7%
Krasnoperov *et al.* [69]	6.21–7.15		0.6–3.2%

Table 2.5: Effect of experimental uncertainty in NRA coverage measurement on extrapolated open-site fraction.

an sp^3 surface carbon from quantum wave packet calculations based on an empirical potential for hydrocarbons [59]. Dawnkaski *et al.* [58] calculate E_A from molecular dynamics simulations on C(100)(2×1) and C(111). Harris *et al.* [29] take E_A from analogous gas-phase data, and Krasnoperov *et al.* [69] measure the reaction of gas-phase hydrogen with polycrystalline diamond at ~2 torr. The resulting activation barriers range from 6.2 to 10.6 kcal/mol. However, the range of activation barriers changes the extrapolated open-site fraction by only a small amount, less than 1%. Although the uncertainty in the NRA value for k_A/k_R has a larger effect on open-site fraction, table 2.5.4 shows that the extrapolated open-site fraction remains one to two orders of magnitude lower than predicted by the thermochemical growth model.

The better agreement between the NRA data and molecular-dynamics simulations indicate that molecular dynamics more accurately simulates surface effects than thermochemical kinetic models. In molecular dynamics, surface effects are approximated by calculating the interaction of the surrounding slab with the gas-phase species and surface sites. On the other hand, thermochemical kinetics models take their surface reaction rates from analogous gas-phase reactions. Surface effects are approximated by taking high-pressure rate constants and accounting for the strain of the surrounding lattice when calculating ΔG to find the reverse rate constants.

Thermochemical models assume that the total reaction cross section per surface site equals the total reaction cross section per equivalent site in an analogous gas-phase reaction [29, 30]. However, the disagreement with the NRA data implies that the two cross sections differ. There are several mechanisms by which a gas-surface reaction cross section differs from an analogous gas-gas reaction cross section. The diamond atoms surrounding the surface site change the reaction cross section by constraining the geometry of the transition state and the angle of approach of the incoming hydrogen. The surface also lacks the kT of translational energy that the analogous gas-phase species would contribute to the reaction. All of these effects are accounted for by the molecular-dynamics simulations and are absent in thermochemical models. Therefore, molecular dynamics rate constants based on well-tested potentials are likely to model diamond growth more accurately than rate constants of analogous gas-phase reactions. These physical reasons and the consistency with the NRA data suggest that molecular-dynamics rate constants be incorporated into diamond growth models to improve reliability.

Extrapolation from dosing temperatures to diamond growth temperature

The quantitative relationship has not yet been determined between reaction rates under dosing conditions, where $\mathrm{T}_g > \mathrm{T}_s$, and rates under CVD conditions, where $\mathrm{T}_g = \mathrm{T}_s$. In the absence of data, the following method is proposed for extrapolating from dosing conditions to diamond growth conditions.

The gas and surface temperature dependence of the ratio k_A/k_R may be expressed as

$$\frac{k_A}{k_R} = \frac{A_{g_A} e^{-E_{g_A}/kT_g} A_{s_A} e^{-E_{s_A}/kT_s}}{A_{g_R} e^{-E_{g_R}/kT_g} A_{s_R} e^{-E_{s_R}/kT_s}}, \tag{2.42}$$

where A_{g_X} is the pre-exponential factor for the gas-phase temperature (T_g) dependence of the rate constant for reaction X, A_{s_X} is the pre-exponential factor for the surface temperature (T_s) dependence, E_{g_X} is the activation barrier associated with the gas-phase temperature, and E_{s_X} is the activation barrier associated with the surface temperature. Eq. 2.42 assumes that the modes are separable into gas and surface, occupied according to the thermal distribution of states at T$_g$ and T$_s$, respectively. Eq. 2.42 holds for a Langmuir-Hinshelwood reaction, where the gas equilibrates with the surface before reacting and $E_s = 0$, and holds for some Eley-Rideal direct reactions, where the gas-phase reactant forms a product immediately upon striking the surface.[19] Experiments performed with T$_g$ = T$_s$ measure activation barrier $E_X = E_{g_X} + E_{s_X}$ and pre-exponential factor $A_X = A_{g_X} \times A_{s_X}$. The effective activation barriers for the ratio k_A/k_R are

$$\frac{k_A}{k_R} = \frac{A_A}{A_R} e^{-(E_{g_A} - E_{g_R})/kT_g} e^{-(E_{s_A} - E_{s_R})/kT_s}. \tag{2.43}$$

The net activation barrier associated with the surface temperature, $E_s \equiv E_{s_A} - E_{s_R}$, is estimated as follows. Koleske *et al.* [11] found a slight surface-temperature dependence for the rate of abstraction from polycrystalline diamond, with an apparent E_{s_A} of 0.8 ± 0.2 kcal/mol. An E_{s_A} of 0.6 kcal/mol falls closer to the range of the data Thoms *et al.* [10], which found k_A/k_R at 600°C to be at most 1.5 times that at 80°C. Dawnkaski *et al.* found the probability of recombination with C(100) and C(111) to decrease between 927°C and 1527°C [58, fig. 3]. Taking A_R to be constant, the decrease implies an E_R between 0.0 and ~-1.5 kcal/mol.[20] The HREELS experiment of Thoms *et al.* [10] found the probability of recombination to differ negligibly at 80°C from 600°C. From the error bars of the HREELS analysis, $|E_{s_R}|$ is less than 0.2 kcal/mol. Therefore, E_{s_R} is taken to be zero. The net surface activation barrier for the ratio k_A/k_R is then $E_s = E_{s_A} - E_{s_R} \approx 0.6$ kcal/mol.

The net activation barrier associated with the gas temperature, $E_g \equiv E_{g_A} - E_{g_R}$, is estimated as follows. As in the preceding paragraph, E_R is estimated to be -1.5 kcal/mol from the recombination probabilities of Dawnkaski *et al.* [58, fig. 3]. Since

---

[19] Reactions with hot precursor mechanisms, where the reactant is trapped on the surface for a time then reacts before fully equilibrating with it, may have several modes not thermalized to either temperature and may not be well-described by eq. 2.42.

[20] The activation barrier, E_R, was calculated by $\frac{p_R(927^\circ C)}{p_R(1527^\circ C)} = \sqrt{\frac{1800}{1200}} \frac{e^{-E_R/(k \cdot 1200K)}}{e^{-E_R/(k \cdot 1800K)}}$, where k is the Boltzmann constant and p_R is the probability of recombination at an isolated radical site on C(100) taken from fig. 3 of ref. [58].

E_{s_R} is small, E_R is taken to be E_{g_R}, or $E_{g_R} \approx -1.5$ kcal/mol. E_{g_A} is taken from experiments performed with $\mathrm{T}_g = \mathrm{T}_s$, which measure $E_A = E_{g_A} + E_{s_A}$. E_{s_A} has not been measured for C(100) or C(111). In the absence of data, E_{s_A} is taken to be 0.6 kcal/mol, as in the preceding paragraph. Therefore, the net gas activation barrier for k_A/k_R is $E_g \simeq (E_A - 0.6) + 1.5 = E_A + 0.9$ kcal/mol, where E_A is the abstraction activation barrier when $\mathrm{T}_g = \mathrm{T}_s$.

The net gas and surface temperature dependence of k_A/k_R is

$$\frac{k_A}{k_R} \simeq \frac{A_{g_A} A_{s_A}}{A_{g_R} A_{s_R}} e^{-\frac{E_A + 0.9\ \mathrm{kcal/mol}}{kT_g}} e^{-\frac{0.6\ \mathrm{kcal/mol}}{kT_s}}, \tag{2.44}$$

where E_A is the abstraction activation barrier when $\mathrm{T}_g = \mathrm{T}_s$. Taking the pre-exponential factors to be temperature-independent, k_A/k_R at NRA dosing temperatures (T_{g1}, T_{s1}) may be extrapolated to k_A/k_R at diamond growth temperatures (T_{g2}, T_{s2}) via

$$\frac{k_A}{k_R}(T_{g2}, T_{s2}) \simeq \frac{k_A}{k_R}(T_{g1}, T_{s1}) e^{-\frac{E_A + 0.9\ \mathrm{kcal/mol}}{k}\left(\frac{1}{T_{g2}} - \frac{1}{T_{g1}}\right)} e^{-\frac{0.6\ \mathrm{kcal/mol}}{k}\left(\frac{1}{T_{s2}} - \frac{1}{T_{s1}}\right)} \tag{2.45}$$

The 0.9 kcal/mol is a correction term to account for the negative barrier to recombination, as well as for the fact that the measured E_A includes not only the gas- but also the surface-temperature dependence of abstraction. Since this correction factor is approximate, and since the 0.6 kcal/mol correction term was chosen from data on polycrystalline diamond, the exact values of the 0.9 and 0.6 correction terms will change as data become available for E_{s_A} on C(100) and C(111), but the magnitudes are expected to remain small.

Since the 0.9 kcal/mol term in eq. 2.45 decreases k_A/k_R and the 0.6 term increases k_A/k_R, the net effect on the extrapolation to diamond growth temperatures is small. Numerical calculation of eq. 2.45 for the activation barriers in table 2.5.4 reveals a negligible change in open-site fraction.

2.6 Conclusions

The absolute deuterium coverage on the diamond (100) surface was measured via NRA, and for the first time absolute coverage was studied as a function of deuterium exposure. The saturation coverage is 0.95 ± 0.04 D per surface C upon exposure to deuterium at 1800°C and a surface temperature of 360°C.

Subsurface deuterium content was estimated to be negligible by comparison to SIMS of microwave plasma-treated C(100) (Appendix A) and to results of previous scattering experiments [9, 51]. The maximum coverages measured by NRA were consistent with negligible diffusion or incorporation into the subsurface region during NRA. Therefore, no deuterium diffusion is expected into the subsurface region.

The coverage was measured for a range of dosing parameters, gas-phase (T_f) and surface (T_s) temperatures. At high filament temperatures *circa* 2000°C coverages up to 1.34 ± 0.09 D per surface C were observed, consistent with the presence of surface dihydrides. A mechanism for dihydride production is suggested: insertion into the dimer bond by hot D from the filament, and a working hypothesis is suggested to explain the surface-temperature dependence of degradation in previous experiments [13]. Despite the high filament temperatures, exposure to elemental tungsten is negligible, and *ex-situ* XPS showed no evidence for the presence of W or Mo (less than 0.1% atomic W) on the sample subsequent to NRA. At low filament temperatures ($\leq$ 1800°C), saturation coverages were close to the expected value of 1 D per surface C. Coverage measurements for the range of T_f and T_s extend the work of Thoms *et al.* [10] and Koleske *et al.* [11], which investigated a single T_f, and the work of Chin *et al.* [12, 13], which measured reaction-rate ratio at a single T_s.

Coverage was studied as a function of anneal temperature subsequent to dosing, and desorption was seen at temperatures above 450°C. Anneals subsequent to the 1800°C exposures gave a thermal desorption barrier of ~3.0 eV assuming first-order desorption with a pre-exponential factor of 10^{13} s^{-1}, consistent with the barriers obtained from TPD by Hoffman *et al.* [27] and Thomas *et al.* [20].

Hydrogen abstraction and recombination with the diamond surface are two of the most important reactions in diamond CVD, as they determine the number of sites available for growth. The NRA results imply that the ratio of recombination rate to abstraction rate on C(100) is 0.06 ± 0.04 at 1800°C. The measured reaction-rate ratio provides a consistency check for the set of reaction parameters used in diamond CVD models. The NRA data are extrapolated down to diamond growth temperatures (927°C) and compared to growth models of C(100) based on analogous gas-phase reactions [29]. Results indicate that thermochemical growth models overpredict the fraction of radical surface sites available for growth by a factor of $\sim$20. Molecular-dynamics simulations [58] are in better agreement with the NRA results, and their reaction parameters are recommended for use in diamond CVD models.

At a filament temperature of 1800°C, the measured ratio of reaction rates, 0.06 ± 0.04, agrees with the HREELS result of Thoms *et al.* [10] and the TOF-SARS measurements of Koleske *et al.* [11]. However, it differs from the value of 0.2 obtained by Chin *et al.* [12, 13] on C(111), possibly due to a variation between site-specific reaction rates on C(100) and C(111), re. Appendix D.

Recommendations for future work

A working hypothesis is suggested to explain the high coverages at high filament temperatures in the present experiment and to explain the surface-temperature dependence of degradation in other experiments [13]. This hypothesis may be tested by dosing the sample in the four different filament and surface temperature regimes and monitoring the coverage.

Further experiments could also be performed to confirm assumptions made here. For example, subsurface deuterium content could be confirmed to be negligible by heating the sample to 1000°C and taking an NRA spectrum to see zero coverage. Negligible contamination by trace elements may be confirmed by performing NRA in a chamber equipped with an X-ray photoelectron spectrometer (XPS). XPS could be performed as a function of sample cooling time without dosing, to eliminate the possibility of contamination during cooling time.

Filament temperatures up to 1800°C are expected to preserve the surface reconstruction, and are recommended for studying reactions with a dimerized surface. However, filament temperature may be raised to $\geq$ 2000°C to investigate the potential process of dimer-bond cracking by hot D emitted from the filament. Low surface temperatures may stabilize dihydrides by precluding D_2 desorption and are recommended for preserving evidence of dimer-bond breakage. Medium surface temperatures may activate D_2 desorption from dihydrides and are recommended for maintaining a dimerized surface. High surface temperatures ($\gtrsim$800°C) activate desorption from monohydrides and may restore a disordered, degraded surface to the (2×1):D reconstruction.

The reaction of *molecular* deuterium with the diamond surface may be studied by keeping the filament temperature low enough to minimize atomic D formation ($\lesssim$ 1000°C). Although room-temperature D_2 and H_2 are unreactive with the diamond surface [13, 16, 20, 25, 41, 64], molecular D_2 reacts with diamond powder above 450°C at atmospheric pressure [64]. In UHV hot D_2 may react with bare diamond by inserting into surface π-bonds. This hypothesis may be tested by exposing a bare sample to D_2 at low filament temperature and investigating coverage as a function of temperature.

On the issue of reaction-rate measurements, future studies of atomic D reactions with diamond could determine not only the value of k_A/k_R but also the activation *barrier*. This could be accomplished by dosing at a series of filament temperatures while keeping the surface fully dimerized. I suggest filament temperatures up to 1800°C, where D cracking of dimer bonds is expected to be negligibly slow, and a surface temperature at or above 360°C, where background gas exposure, prior to dosing, is minimized. However, at filament temperatures below ~1200°C, the hydrogen cracking efficiency is small [70]. Reaction rates of *molecular* hydrogen may be studied at lower filament temperature. To obtain data more directly comparable to diamond CVD conditions (700–1000°C), an UHV-compatible radio-frequency glow discharge oven may be fabricated to produce lower-temperature atomic hydrogen [71].

Finally, future work could extend the NRA experiment by separately determining the individual reaction rates, k_A and k_R, in addition to their ratio, k_A/k_R. These parameters can be measured by calibrating the atomic deuterium flux via a chopped, differentially-pumped mass spectrometer and by performing the analysis described in section 2.5.1. The resulting site-averaged reaction rates may be compared to site-specific rates by modeling site-specific coverages via the kinetic Monte Carlo algorithm of Appendix C. Diamond surface science is one area where neither modeling nor experiment alone can yield all the relevant reaction mechanisms and parameters, but only the two working in concert.

2.7 Acknowledgements

The diamond sample was provided by the California Institute of Technology. I thank Dr. Lou Troilo and Dr. James Butler, for help in plasma treating the sample at the Naval Research Laboratory, and Mr. Robert Rossi, for imaging the sample via AFM at Caltech. I am especially grateful to Dr. John N. Russell, Jr., of the Naval Research Laboratory for many useful discussions throughout the course of the experiment.

The NRA experiment was facilitated by the Surface Modification and Characterization (SMAC) Research Center of Oak Ridge National Laboratory. I gratefully acknowledge the help of Drs. David B. Poker and David M. Zehner, the technical support of Mrs. Gary Ownby, Dale K. Hensley, and Darrell K. Thomas, and the general support of all SMAC members.

The work at ORNL was sponsored by the Division of Materials Sciences, U. S. Department of Energy, under contract DE-AC05-96OR22464 with Lockheed Martin Energy Research Corp. Travel and local transportation were provided through the personal funds of M. Susan Melnik, Dr. Walter L. Melnik, Dr. Ernest N. Prabhaker, Mr. Glenn C. Smith; the hospitality of Dr. Gary Farlow, Dr. Wayne Holland, Dr. Youlian Davidov, Dr. Jay Jellison, and Dr. John Budai; and the general funds of the Engineering and Applied Sciences Division of the California Institute of Technology. Local housing was provided in part by the hospitality of Mrs. and Mr. Katherine and Jonathan Fain. Additional funds were provided by the ARCS Foundation, ONR and NSF.

Bibliography

[1] J. Wei and J. T. Yates, Jr., "Diamond surface chemistry I–A Review." Critical Reviews in Surface Chemisty **5**, 1–71 (1995).

[2] J. C. Angus and C. C. Hayman, "Low pressure metastable growth of diamond and 'diamondlike' phases." Science **241**, 913–921 (1988).

[3] Y. Sato and M. Kamo. In *The Properties of Natural and Synthetic Diamond*, edited by J. E. Field, Academic Press, London (1992), p. 424.

[4] D. G. Goodwin and J. E. Butler, "Theory of diamond chemical vapor deposition." In *Handbook of Industrial Diamond and Diamond Films*, edited by M. Prelas, G. Popovici and L. K. Bigelow, Marcel Dekker, Inc. (in press).

[5] Y. L. Yang, L. M. Struck, L. F. Sutcu and M. P. D'Evelyn, "Chemistry of hydrogen on diamond (100)." Thin Sol. Films **225**, 203–211 (1993).

[6] S. P. Mehandru and A. B. Anderson, "Adsorption of H, CH_3, CH_2 and C_2H_2 on (2×1) restructured diamond (100)—Theoretical study of structures, bonding, and migration." Surf. Sci. **248**, 369–381 (1991).

[7] T. E. Derry, C. C. P. Madiba and J. P. F. Sellschop, "Oxygen and hydrogen on the surface of diamond." Nucl. Instr. Meth. **218**, 559–562 (1983).

[8] H. Yagi, K. Tanida, K. Nishimura, A. Hatta, T. Ito and A. Hiraki, "Elastic recoil detection analysis for hydrogen near the surface of chemical-vapor-deposited diamond." Jpn. J. Appl. Phys. **34**, L577–L579 (1995).

[9] G. Dollinger, A. Bergmaier, C. M. Frey, M. Roesler and H. Verhoeven, "Impurities of light elements in CVD diamond." Diam. Rel. Mat. **4**, 591–595 (1995).

[10] B. D. Thoms, J. N. Russell, Jr., P. E. Pehrsson and J. E. Butler, "Adsorption and abstraction of hydrogen on polycrystalline diamond." J. Chem. Phys. **100**, 8425–8431 (1994).

[11] D. D. Koleske, S. M. Gates, B. D. Thoms, J. N. Russell, Jr. and J. E. Butler, "Hydrogen on polycrystalline diamond films—studies of isothermal desorption and atomic deuterium abstraction." J. Chem. Phys. **102**, 992–1002 (1995).

[12] R. P. Chin, *Nonlinear optical spectroscopy of diamond surfaces*. Ph.D. thesis, University of California, Berkeley, Berkeley, CA (1995). Also available as Lawrence Berkeley Laboratory Report no. LBL-37110.

[13] R. P. Chin, J. Y. Huang, Y. R. Shen, T. J. Chuang and H. Seki, "Interaction of atomic hydrogen with the diamond C(111) surface studied by infrared-visible sum-frequency-generation spectroscopy." Phys. Rev. B **52**, 5985–5995 (1995).

[14] J. B. Marsh and H. E. Farnsworth, "Low-energy electron diffraction studies of (100) and (111) surfaces of semiconducting diamond." Surf. Sci. **1**, 3–21 (1964).

[15] P. G. Lurie and J. M. Wilson, "The diamond surface I. The structure of the clean surface and the interaction with gases and metals." Surf. Sci. **65**, 453–475 (1977).

[16] B. B. Pate, "The diamond surface: Atomic and electronic structure." Surf. Sci. **165**, 83–142 (1986).

[17] S.-T. Lee and G. Apai, "Surface phonons and CH vibrational modes of diamond C(110) and C(111) surfaces." Phys. Rev. B **48**, 2684–2693 (1993).

[18] A. V. Hamza, G. D. Kubiak and R. H. Stulen, "Hydrogen chemisorption and the structure of the diamond C(100)-(2x1) surface." Surf. Sci. **237**, 35–52 (1990).

[19] B. D. Thoms and J. E. Butler, "HREELS and LEED of H/C(100): the 2×1 monohydride dimer row reconstruction." Surf. Sci. **328**, 291–301 (1995).

[20] R. E. Thomas, R. A. Rudder and R. J. Markunas, "Thermal desorption from hydrogenated and oxygenated diamond (100) surfaces." J. Vac. Sci. Technol. A **10**, 2451–2457 (1992).

[21] H. Ibach and D. L. Mills, *Electron Energy Loss Spectroscopy and Surface Vibrations*. Academic Press, New York (1982).

[22] B. D. Thoms and J. E. Butler, "HREELS scattering mechanism from diamond surfaces." Phys. Rev. B **50**, 17450–17455 (1994).

[23] T. Aizawa, T. Ando, M. Kamo and Y. Sato, "High-resolution electron-enegry-loss spectroscopic study of epitaxially grown diamond (111) and (100) surfaces." Phys. Rev. B **48**, 18,348–18,351 (1993).

[24] B. Sun, X. Zhang, Q. Zhang and Z. Lin, "Investigation of the grown diamond (100) surface using high resolution electron energy loss spectroscopy." Mat. Res. Bull. **28**, 131–135 (1993).

[25] J. E. Butler, B. D. Thoms, M. McGonigal, J. N. Russell, Jr. and P. E. Pehrsson, "Hydrogen chemistry on diamond surfaces." In *Wide Band Gap Electronic Materials*, edited by M. A. Prelas *et al.*, Kluwer Academic Publishers, the Netherlands (1995), pp. 105–114.

[26] C. A. Fox, S. Hagstrom, M. T. Schulberg and G. D. Kubiak, "Hydrogen desorption kinetics from low-index diamond surfaces." Extended Abstracts of the 183rd Electrochemical Society Meeting **93–1**, 601 (1993).

[27] A. Hoffman, K. Bobrov, B. Fisgeer, H. Shechter and M. Folman, "Effects of deuterium adsorption–desorption on the state of diamond: surface degradation and stabilization of sp^3 bonded carbon." Diam. Rel. Mat. **5**, 977–983 (1996).

[28] A. Hoffman, "Deuterium interaction with the diamond (111) surface studied by TPD, EELS and LEED." In *Topics in Diamond and c-BN Research: Proceedings of The 4th NIRIM International Symposium on Advanced Materials (ISAM '97)*,

edited by Y. Sato, I. Kusunoki, H. Kawarada, M. Akaishi, T. Ando, M. Kamo, H. Kanda, S. Matsumoto, K. Kojima and M. Kobayashi, National Institute for Research in Inorganic Materials, Tsukuba-shi, Ibaraki-ken, Japan (1997), pp. 83–90.

[29] S. J. Harris and D. G. Goodwin, "Growth on the reconstructed diamond (100) surface." J. Phys. Chem. **97**, 23–28 (1993).

[30] D. N. Belton and S. J. Harris, "A mechanism for growth on diamond (110) from acetylene." J. Chem. Phys. **96**, 2371–2377 (1992).

[31] S. J. Harris, "Mechanism for diamond growth from methyl radicals." Appl. Phys. Lett. **56**, 2298–2300 (1990).

[32] M. T. Schulberg, G. D. Kubiak and R. H. Stulen, "Temperature programmed desorption of hydrogen and deuterium from CVD diamond samples." Mat. Res. Soc. Symp. Proc. **207**, 401–406 (1992).

[33] K. Sinniah, M. G. Sherman, L. B. Lewis, W. H. Weinberg, J. T. Yates, Jr. and K. C. Janda, "Hydrogen desorption from the monohydride phase on Si(100)." J. Chem. Phys. **92**, 5700–5711 (1990).

[34] B. D. Thoms, M. S. Owens, J. E. Butler and C. Spiro, "Production and characterization of smooth, hydrogen-terminated diamond C(100)." Appl. Phys. Lett. **65**, 2957–2959 (1994).

[35] D. R. Lide, ed., *CRC Handbook of Chemistry and Physics*. CRC Press, Inc., Boca Raton (1990).

[36] J. N. Smith, Jr. and W. L. Fite, "Reflection and dissociation of H_2 on tungsten." J. Chem. Phys. **37**, 898–904 (1962). See especially pp. 898 and 903–904.

[37] D. A. King, T. E. Madey and J. T. Yates, Jr., "Interaction of oxygen with polycrystalline tungsten. I. Sticking probabilities and desorption spectra." J. Chem. Phys. **55**, 3236–3246 (1971). Note especially figs. 13–15.

[38] F. Rosebury, *Handbook of electron tube and vacuum techniques*. American Vacuum Society classics, American Institute of Physics (1993). pp. 405–407. Originally published in 1964.

[39] J. W. Mayer and E. Rimini, eds., *Ion Beam Handbook for Material Analysis*. Academic Press, Inc., New York (1977). Since the laboratory scattering angle is between 120° and 160°, the proton energy is $\sim$13 MeV.

[40] V. S. Smentkowski, H. Jänsch, M. A. Henderson and J. T. Yates, Jr., "Deuterium atom interaction with diamond (100) studied by X-ray photoelectron spectroscopy." Surf. Sci. **330**, 207–226 (1995).

[41] B. D. Thoms, P. E. Pehrsson and J. E. Butler, "A vibrational study of the adsorption and desorption of hydrogen on polycrystalline diamond." J. Appl. Phys. **75**, 1804–1810 (1994).

[42] J. N. Russell, Jr. (1997). Private communication.

[43] T. Sakuri and H. D. Hagstrum, "Interplay of the monohydride phase and a newly discovered dihydride phase in chemisorption of H on Si(100)2×1)." Phys. Rev. B **14**, 1593–1596 (1976).

[44] K. Oura, J. Yamane, K. Umezawa, M. Naitoh, F. Shoji and T. Hanawa, "Hydrogen adsorption on Si(100)-2×1 surfaces studied by elastic recoil detection analysis." Phys. Rev. B **41**, 1200–1203 (1990).

[45] S. M. Gates, R. R. Kunz and C. M. Greenlief, "Silicon hydride etch products from the reaction of atomic hydrogen with Si(100)." Surf. Sci. **207**, 364–384 (1989).

[46] E. Best and I. Hinze, "Mo supplement volume A3: Metal chemical reactions." In *Gmelin Handbook of Inorganic Chemistry*, edited by E. F. Linde, J. F. Rounsaville, R. C. Sangster and K. Swars, Springer-Verlag, Berlin (1983), pp. 23–43, 75–77.

[47] D. B. Poker and C. F. Walters (1997). Private communication.

[48] H. Jehn, D. Schneider and F. Schröder, "W wolfram erganzungsband BI: Die systeme mit edelgasen, wasserstoff und sauerstoff." In *Gmelin Handbook of Inorganic Chemistry*, edited by L. Berg, H. Hein and H. Katscher, Springer-Verlag, Berlin (1978), pp. 82–88 (for H), 89–130 (for O).

[49] L. Foster, G. Vizkelethy, M. Lee, J. R. Tesmer and M. Nastasi, "Particle-particle nuclear reaction cross sections." In *Handbook of Modern Ion Beam Materials Analysis*, edited by J. R. Tesmer and M. Nastasi, Materials Research Society, Pittsburgh, PA (1995), pp. 549–568.

[50] J. F. Zeigler, "Helium stopping powers and ranges in all elements." In *The Stopping Powers and Ranges of Ions in Matter*, Pergamon Press, New York (1977), volume 4. See p. 30 for conversion between ^{3}He and ^{4}He stopping powers.

[51] J. P. F. Sellschop, S. H. Connell, C. C. P. Madiba, E. Sideras-Haddad, M. Stemmet, K. Bharuth-Ram, H. Appel, W. Kundig, B. Patterson and E. Holzschuh, "Hydrogen in and on natural and synthetic diamond." Nucl. Instr. Meth. B **68**, 133–140 (1992).

[52] G. Faure, *Principles of Isotope Geology*. John Wiley & Sons, New York (1977). See p. 324 for the isotopic abundance of ^{2}H. See pp. 379 and 387 for the isotopic abundance of ^{13}C in natural colorless diamond.

[53] W. A. Gray and R. Müller, *Engineering Calculations in Radiative Heat Transfer*. Pergamon Press, Oxford (1974).

[54] J. N. Smith, Jr. and W. L. Fite, "Reflection and dissociation of H_2 on tungsten." J. Chem. Phys. **37**, 898–904 (1962).

[55] T. W. Hickmott. J. Chem. Phys. **32**, 810 (1960).

[56] J. F. O'Hanlon, *A User's Guide to Vacuum Technology*. John Wiley & Sons, New York (1989).

[57] B. Sun, X. Zhang, Q. Zhang and Z. Lin, "Effect of atomic hydrogen and oxygen on diamond growth." J. Appl. Phys. **73**, 4614–4617 (1993).

[58] E. J. Dawnkaski, D. Srivastava and B. J. Garrison, "Time dependent Monte Carlo simulations of H reactions on the diamond $\{001\}(2\times1)$ surface under chemical vapor deposition conditions." J. Chem. Phys. **102**, 9401–9411 (1995).

[59] D. W. Brenner, "Empirical potential for hydrocarbons for use in simulating the chemical vapor-deposition of diamond films." Phys. Rev. B **42**, 9458–9471 (1990).

[60] G. Ehrlich, "Molecular dissociation and reconstitution on solids." J. Chem. Phys. **31**, 1111–1126 (1959).

[61] D. G. Goodwin, "Scaling laws for diamond chemical-vapor deposition. II. Atomic hydrogen transport." J. Appl. Phys. **74**, 6895–6906 (1993).

[62] D. Brennan and P. C. Fletcher, "The atomization of hydrogen on tungsten." Proc. Roy. Soc. London A **250**, 389–408 (1959).

[63] H. W. Woolley, R. B. Scott and F. G. Brickwedde, "Compilation of thermal properties of hydrogen in its various isotopic and ortho-para modifications." J. of Res. of the Nat. Bureau of Standards **41**, 379–475 (1948). See especially p. 393.

[64] T. Ando, M. Ishii, M. Kamo and Y. Sato, "H–D exchange reaction on diamond surfaces studied by diffuse reflectance Fourier transform IR spectroscopy." Diam. and Rel. Materials **4**, 607–611 (1995).

[65] P. J. Eenshuistra, J. H. M. Bonnie, J. Los and H. J. Hopman, "Observation of exceptionally high vibrational excitation of hydrogen molecules formed by wall recombination." Phys. Rev. Lett. **60**, 341–344 (1988).

[66] C. C. Cheng, S. R. Lucas, H. Gutleben, W. J. Choyke and J. T. Yates, Jr., "Atomic hydrogen driven halogen extraction from Si(100) —Eley–Rideal surface kinetics." J. Am. Chem. Soc. **114**, 1249 (1992).

[67] D. W. Brenner, D. H. Robertson, R. Carty, D. Srivastava and B. J. Garrison. Mat. Res. Soc. Symp. Proc. **278**, 255 (1992).

[68] X. Y. Chang, M. Perry, J. Peploski, D. L. Thompson and L. M. Raff, "Theoretical studies of hydrogen-abstraction reactions from diamond and diamond-like surfaces." J. Chem. Phys. **99**, 4748–4758 (1993).

[69] L. N. Krasnoperov, I. J. Kalinovski, H.-N. Chu and D. Gutman, "Heterogeneous reaction of H atoms and CH_3 racicals with a diamond surface in the 300–1133 K temperature range." J. Phys. Chem. **97**, 11787–11796 (1993).

[70] T. Sakurai, M. J. Cardillo and H. D. Hagstrum, "Kinetics of the generation of atomic hydrogen and its adsorption on Si(110)." J. Vac. Sci. Tech. **14**, 397–399 (1977).

[71] J. B. Hodgson and A. A. Haasz, "Compact radio-frequency glow-discharge atomic hydrogen beam source." Rev. Sci. Instrum. **62**, 96–99 (1991).

Chapter 3 Migration on the C(110) Surface: *Ab-initio* Computations

3.1 Introduction

Mobile surface adsorbates play a key role in surface processes of semiconductors such as silicon and gallium arsenide. However, before this work was first published [1] diamond surface science studies had generally assumed mobility to be low [2], and diamond chemical-vapor deposition (CVD) studies had not established the competitiveness of surface migration with gas-surface reactions. In diamond surface science, the thermal desorption of H_2 from C(100) was found to obey first-order rate kinetics [3, 4]. Desorption from Si(100) was also first-order, and a pre-pairing mechanism had been proposed to explain why the two-body desorption was not second-order [5]. However, the possibility of pre-pairing on diamond had not been investigated, and a mobility mechanism to produce the pre-pairing had not been established. In diamond chemical-vapor deposition studies, activation barriers to migration of surface CH_2 and CH_3 [6] had been calculated, yet the competitiveness of these migration rates with gas-surface reaction rates had not been demonstrated. One particular step in an acetylene growth mechanism, two-center ring closure, had been proposed to proceed via a concerted reaction involving hydrogen transfer [7]. However, Chang *et al.* [8] later performed a thorough search of the potential energy surface about the transition state and found that ring closure was more likely to proceed via gas-phase hydrogen abstraction than surface migration. Thus, diamond surface models had yet to establish a mobility mechanism to produce pre-pairing, and diamond CVD models had concentrated on gas-surface reactions [9, 10] and gas-phase dynamics [11] rather than surface migrations.

Diffusion of chemisorbed species can occur on the diamond surface by insertion into a C-H bond or migration to a neighboring radical site. We restrict attention to the latter. Migration was considered to be negligible under typical CVD conditions because the majority of diamond surface sites have neighbors which are terminated by hydrogen, which blocks migration pathways. In CVD environments containing halogens [12], a fraction of the surface sites may also be terminated by fluorine or chlorine. Nevertheless, during growth some fraction of the surface terminator is missing, exposing open surface radical sites. The surface coverage is determined by a balance of abstraction by gas-phase radicals and recombination onto radical sites. Under hydrogen-based CVD conditions, the experiment of chapter 2 suggests that 2% of the surface sites are open, and modeling studies suggest that up to 40% are open [13]. If the surface-terminating species are mobile, then the open radical sites may be regarded as mobile. This would clear pathways for hydrocarbon adsorbate diffusion.

Even when surface coverage limits mobility to short-range diffusion, surface migration may have implications for diamond growth mechanisms. Before this work [1, 14], no proposed growth mechanism had included simple migration of surface terminators[1]. These studies often found pathways which were blocked due to steric hindrance from neighboring terminators, or concluded that the reaction must proceed through a highly strained intermediate. Both of these conclusions could be radically altered by even a small degree of mobility of surface terminators.

To demonstrate mobility and its competitiveness with gas-surface reactions, we calculated the *ab initio* quantum chemical activation barriers to migration of H, F, and Cl on a diamond surface. Attention is restricted to the (110) surface, which has a higher growth rate than either the (100) or (111) surfaces [16]. (110)-type sites also appear at steps on the (100) and (111) surfaces. Our results were summarized in previous publications [14, 17], and more complete details are given here.

---

[1] Huang and Frenklach [15] had calculated a barrier to migration on the (100) (1×1):2H surface by semi-empirical MNDO methods. However, their emphasis had been the calculation of the energetics for several possible reaction steps in diamond growth from addition of methyl, CO, and acetylene; and none of these calculations included migration within the reaction pathway.

3.2 Computational method

3.2.1 Calculation of the electronic wavefunction

The Schrödinger equation was solved for a cluster of atoms modeling each migration using standard *ab-initio* techniques [18]. The nuclear kinetic energy was neglected, and the Hamiltonian included all coulomb interactions and the kinetic energy of the electrons.

$$\mathbf{H} \equiv -\frac{1}{2}\sum_{i}^{n} \nabla_i^2 + \sum_{i}^{n}\sum_{j<i} \frac{1}{|\vec{r}_i - \vec{r}_j|} - \sum_{i}^{n}\sum_{A}^{N} \frac{Z_A}{|\vec{r}_i - \vec{r}_A|} + \sum_{A}^{N}\sum_{B<A} \frac{Z_A Z_B}{|\vec{r}_A - \vec{r}_B|} \qquad (3.1)$$

where $\mathbf{H}$ is the Hamiltonian, E is the total energy, $|\Psi\rangle$ is the electronic wavefunction, n is the number of electrons and N the number of nuclei, and Z is the atomic number. All quantities are expressed in atomic units.

The spatial orbitals, ϕ, were expressed in terms of Gaussian basis functions, χ_μ, centered on the nuclei,

$$\phi_i = \sum_{\mu=1}^{100} c_{i\mu}\chi_\mu.$$

Two basis sets were used in these calculations. A valence triple-zeta (VTZ) set with polarization[2] was included for the two carbons directly involved in the migration. A VTZ basis with polarization[3] was included for the migrating hydrogen. The fluorine and chlorine basis sets were VTZ plus polarization[4]. The Dunning double-zeta contraction[5] was used on all peripheral carbons and hydrogens.

---

[2] The carbon triple-zeta basis set consisted of a diffuse s function, exponent 0.0474, and a diffuse p function, exponent 0.0365, in addition to a double-zeta (9s5p)/[3s2p] contraction from ref. [19]. The carbon polarization function was d-type with an exponent of 0.75.

[3] The exponents for the hydrogen triple-zeta basis set were taken from the (6s) set of Table V of ref. [20]. The four smallest coefficients were also taken from this reference. The coefficients for the two most diffuse functions were 1.0 each. Thus the hydrogen triple-zeta basis set consisted of a (6s)/[3s] contraction. The hydrogen polarization function was p-type with an exponent of 0.6.

[4] The fluorine triple-zeta basis set was the (11s7p)/[5s3p] contraction from ref. [21]. The exponent for the fluorine (1d) polarization function was taken from ref. [22]. The chlorine triple-zeta basis set was the (12s9p)/[6s5p] contraction from ref. [23]. Chlorine polarization was d-type with an exponent of 0.6.

[5] The carbon double-zeta basis set was the (9s5p)/[3s2p] contraction from ref. [19]. The hydrogen double-zeta basis set was the (4s)/[2s] contraction of ref. [19] with scale factor of 1.2.

I approximated each electron as interacting only with the mean field of all other electrons, producing the Hartree-Fock (HF) wavefunction,

$$\left|\Psi^{\mathrm{HF}}\right\rangle = \mathcal{A}\left\{\left|\left(\prod_{i=1}^{m-1} {\phi_i}^2\alpha\beta\right)\phi_m\alpha\right\rangle\right\}, \tag{3.2}$$

where $\mathcal{A}$ is the antisymmetry operator, m is the number of spatial orbitals $(n/2+1)$, and α and β are up and down spin eigenfunctions, respectively.

Next I correlated the electrons directly involved in the reaction at the Generalized-Valence-Bond (GVB) or Complete-Active-Space (CAS) level, where

$$\left|\Psi^{\mathrm{CAS}}\right\rangle = \mathcal{A}\left\{\sum_{f_j+f_k+f_l=n_{active}} C_{jkl}\left|\left(\prod_{i=1}^{m-2} {\phi_i}^2\alpha\beta\right)_{inactive}\left(\phi_{m-1}^{f_j}\phi_m^{f_k}\phi_{m+1}^{f_l}\right)_{active}\right\rangle\right\} \tag{3.3}$$

and n_{active} is the number of active electrons. The GVB-CAS calculation optimizes the configuration coefficients, C_{jkl}, and the orbital coefficients, $c_{i\mu}$. For the hydrogen migrations, the GVB-CAS active space included 3 electrons in 3 orbitals (3 in 3), and the wavefunction has the orbitals optimized for all seven spatial configurations (8 spin eigenfunctions).

An active space was developed for the halogen migrations by testing several cases, including 3 in 3, 5 in 5, and 7 in 7. In all test cases the GVB-CAS determined similar weight distributions for the three most important configurations. In subsequent calculations, 7-in-7 active spaces were generally used, to include 4 of the electrons in the halogen's outer-shell as well as the 2 in the carbon-halogen bonding orbital and the 1 in the carbon radical orbital.

Finally, given the HF or GVB-CAS wavefunction, I included further correlations between electrons by carrying out Configuration-Interaction (CI) calculations in which all single and double excitations were allowed from all non-core occupied to all virtual orbitals. These wavefunctions are denoted as SD-HF and SD-CAS respectively and written as

$$
\begin{aligned}
\left|\Psi^{\mathrm{SD}}\right\rangle = \mathcal{A} \Bigg\{ & \sum_{\substack{\text{single}\\ \text{excitations}}} C_\alpha \left|(\phi)_{core}\,(\phi)^{*}_{inactive}\,(\phi)_{active}\,(\phi)_{virtual}\right\rangle \\
& + \sum_{\substack{\text{single}\\ \text{excitations}}} C_\alpha \left|(\phi)_{core}\,(\phi)_{inactive}\,(\phi)^{*}_{active}\,(\phi)_{virtual}\right\rangle \\
& + \sum_{\substack{\text{double}\\ \text{excitations}}} C_\alpha \left|(\phi)_{core}\,(\phi)^{*}_{inactive}\,(\phi)^{*}_{active}\,(\phi)_{virtual}\right\rangle \\
& + \sum_{\substack{\text{double}\\ \text{excitations}}} C_\alpha \left|(\phi)_{core}\,(\phi)_{inactive}\,(\phi)^{**}_{active}\,(\phi)_{virtual}\right\rangle \\
& + \sum_{\substack{\text{double}\\ \text{excitations}}} C_\alpha \left|(\phi)_{core}\,(\phi)^{**}_{inactive}\,(\phi)_{active}\,(\phi)_{virtual}\right\rangle \Bigg\} . \qquad (3.4)
\end{aligned}
$$

Here $(\phi)_{core}$ are the orbitals of the inner-shell carbon and halogen electrons, and the $*$ superscript represents the excitation of a single electron into a virtual orbital. The SD-HF and SD-CAS calculations fix the orbital coefficients, $c_{i\mu}$, and optimize the CI coefficients, C_α. Thus the major purpose of the HF and GVB-CAS calculations is to obtain optimal orbitals upon which to base the CI calculations. The CI active space included 3 electrons in 3 orbitals for the H migrations and 5 in 5 for the halogen migrations. To include the most important higher-order correlations for the H migrations, the CI calculation was based upon a 3-reference wavefunction where the 3 references were the configurations with the highest weight in the GVB-CAS calculation.

The GVB-CAS calculation often diverged unless it included the halogen's outer-shell s electrons in the active space. To make convergence automatic, most halogen GVB-CAS calculations were performed from the SD-HF CI numbers as the starting wavefunction. These calculations are denoted CAS-CI.

All calculations were performed using a modified version of the MOLECULE/SWEDEN suite of codes [24]. For H migration, I used both SD-HF and SD-CAS wavefunctions. For the halogens, my final results included only SD-HF wavefunctions. The choice of SD-HF or SD-CAS wavefunction is explained in section 3.3.1.

3.2.2 Optimization of cluster geometries

As a model for the (110) surface, we consider constrained clusters in which all surface C-C bonds not involved in the reaction are replaced by C-H bonds. This leads to the clusters shown in figs. 3.1a-3.3a. The internuclear C-C distances were fixed at 1.54 Å, the value for bulk diamond [25]. All C-H bond lengths on the peripheral hydrogens were fixed at 1.10 Å, a value typical for hydrocarbons. In large-scale multireference configuration interaction calculations of (1,2) Cl migration, Engels *et al.* [26] found that variations in the CH bond length had "minor influence on the total energy." The only atom whose coordinates were optimized during our calculation was the migrating X (H, F, or Cl).

The transition-state geometry was determined by placing the migrating atom at several positions along the symmetry axis, for the (1,2) and (1,4) migrations, or symmetry plane, for the (1,3) migration. The position was optimized to give the minimum energy, and the resulting geometries are shown in figs. 3.1b-3.3b. The reactant geometry was determined by placing the migrating atom in a bonded position, at a tetrahedral geometry from one of the primary carbon centers. The active C-H, C-F and C-Cl bond lengths were then optimized for the reactant clusters.[6] The activation energy was the difference between the transition-state energy and the reactant energy.

In several cases the geometry of the transition and reactant states was confirmed by least-squares fitting a parabola to the energies of the four geometries closest to the state. The parabola's minimum was within 0.01 Å of the minimum determined by the single-point calculations. The geometry resolution of the single-point calculations produced an uncertainty in the activation energies of about 0.05 eV.

Since the (1,4) H migration required the largest CI calculations, I optimized its transition-state geometry at the SD-CAS single-reference level and calculated the energy of that geometry at the triple-reference level. I also took the reactant energy to be equal to the SD-HF reactant energy, which makes my estimate for the SD-CAS

---

[6] The active C-F and C-Cl bond lengths were optimized individually for each reactant cluster. The active C-H bond length was optimized for the reactant cluster of the (1,2) migration, and the bond length for the (1,4) and (1,3) H migrations was taken to be the same as that of the (1,2) migration.

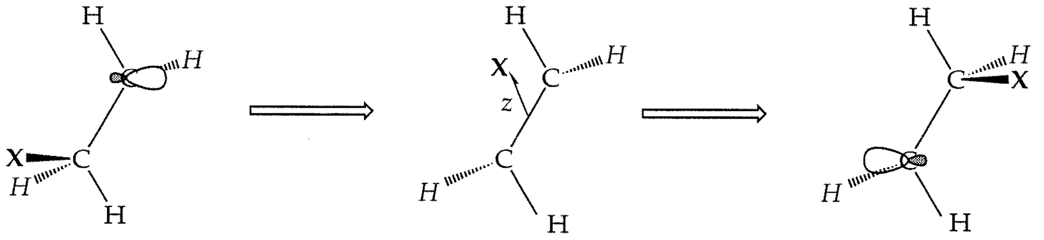

(a) Reactant (b) Transition State (c) Product

Figure 3.1: Cluster for (1,2) migration. X represents H, F, or Cl, and (110) lies in the plane of the paper. The origin bisects the surface C-C bond, and the z axis is perpendicular to the surface (110) plane.

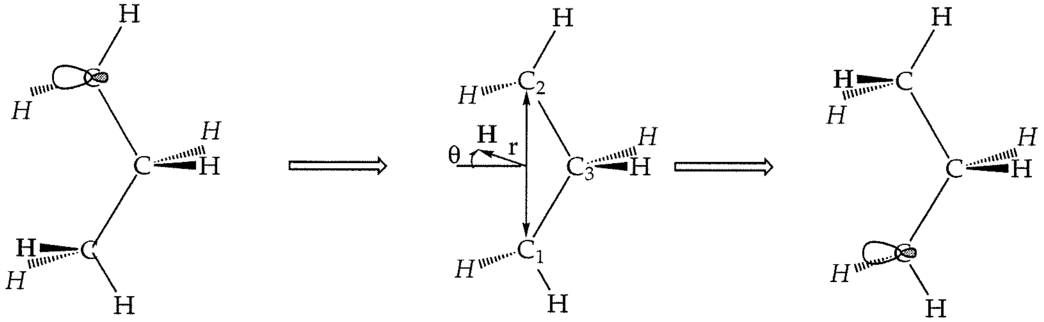

(a) Reactant (b) Transition State (c) Product

Figure 3.2: Cluster for (1,3) migration. (110) lies in the plane of the paper. The midpoint between C_1 and C_2 determines the origin, and θ=0 lies in the $C_1C_2C_3$ plane. The (r, θ) plane is perpendicular to the surface (110) plane.

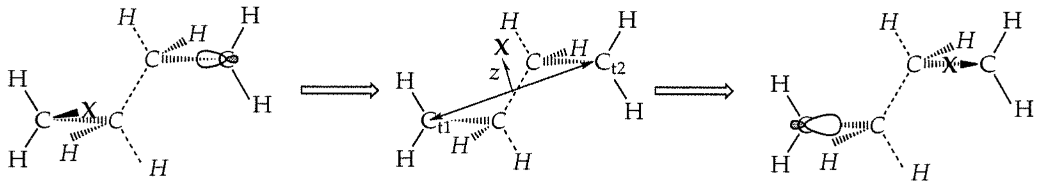

(a) Reactant (b) Transition State (c) Product

Figure 3.3: Cluster for (1,4) migration. X represents H, F, or Cl, and (110) lies in the plane of the paper. The origin is located halfway between C_{t1} and C_{t2}, and the z axis is perpendicular to the surface (110) plane.

activation barrier too low by about 0.1 eV/cluster for (1,4) H migration.

3.3 Results

3.3.1 Comparison of SD-HF to SD-CAS energy

The SD-CAS wavefunction gives an energy closest to the actual activation barrier. Therefore it was used in all cases where computationally feasible. As the H migrations had only 3 electrons directly involved in the reaction, it was straightforward to determine the appropriate orbitals for the active space of the GVB-CAS wavefunction. In this case the calculated energies behaved as expected: the calculated activation barrier at the HF level was higher than that at the GVB-CAS level which was in turn higher than that at the SD-CAS level, the best level of approximation.

However, the outer-shell electrons of F and Cl participated in their migrations, making it difficult to design an active space that was large enough to be physically reasonable and small enough to be computationally feasible. Figs. 3.4 and 3.5 show that in a few cases SD-CAS energies were actually *higher* than SD-HF energies. Here the SD-CAS calculations were based upon a single-reference wavefunction, the dominant configuration of the 5-in-5 GVB-CAS. A multi-reference CI would have more effectively included interactions with the halogen outer-shell electrons, and multi-reference SD-CAS energies are expected to be lower than SD-HF energies. However, since multi-reference CIs were computationally impractical for the halogen migrations, these reactions were calculated at the SD-HF level.

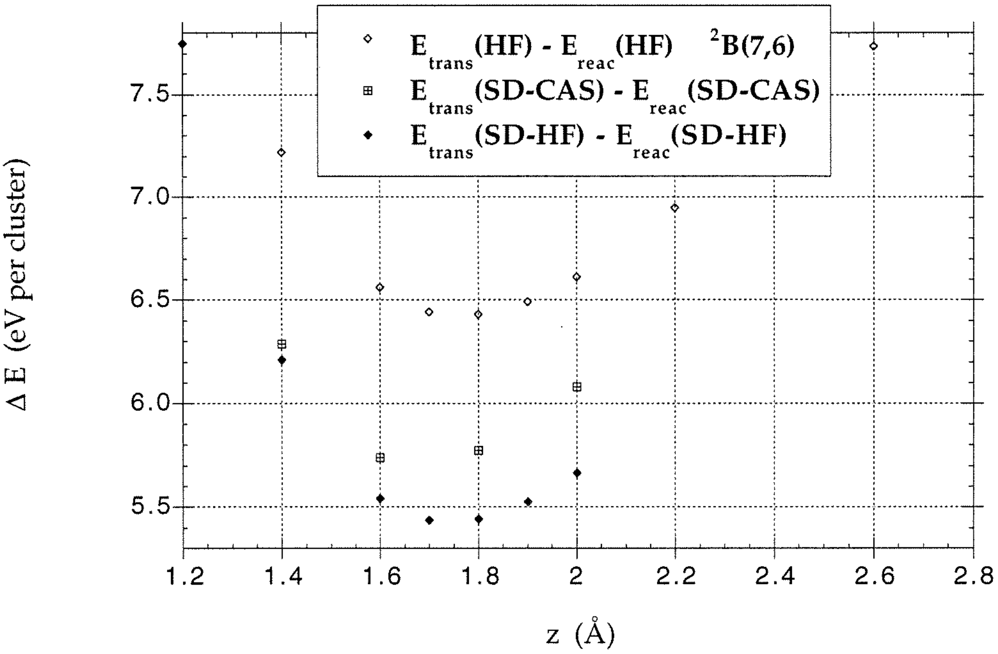

Figure 3.4: Computed potentials of an excited transition state for (1,2) F migration. The HF configuration was $^2B(7,6)$, and the active space of the GVB-CAS and SD calculations included 5 electrons in 5 orbitals. The z axis is defined in fig. 3.1 .

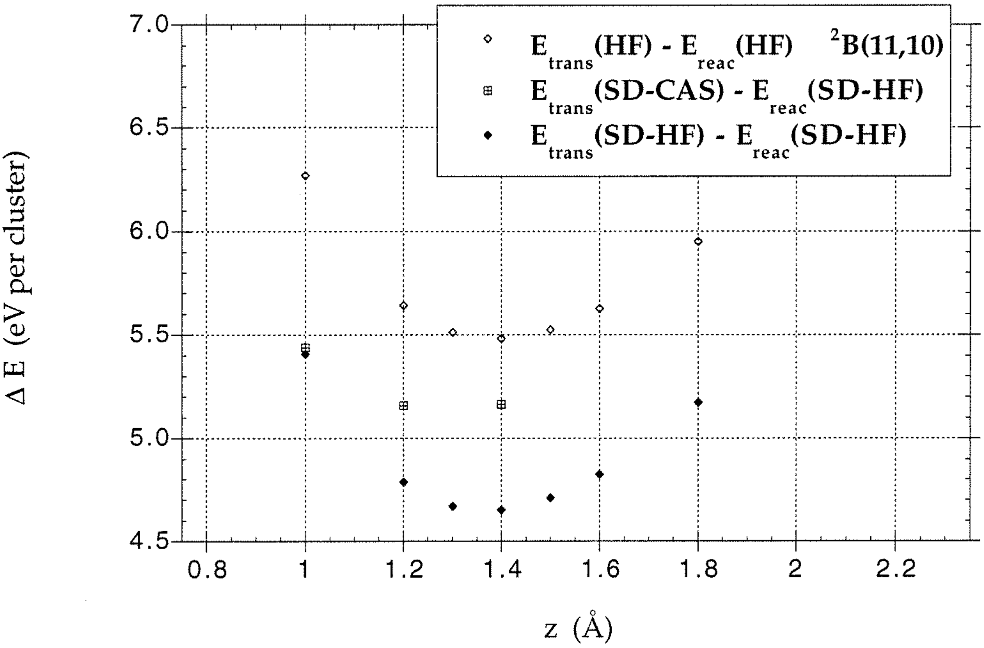

Figure 3.5: Computed potentials of an excited transition state for (1,4) F migration. The HF configuration was $^2B(11,10)$, and the active space of the GVB-CAS and SD calculations included 5 electrons in 5 orbitals. The z axis is defined in fig. 3.3 .

3.3.2 Determination of ground and excited transition states

Although physical considerations narrow the field, one cannot determine the ground electronic configuration *a priori*. I calculated the energies of several configurations closest to the expected ground state for the halogen migrations, where outer-shell electrons complicate the reaction. Results are summarized in table 3.1, and details are given at the end of the chapter in figs. 3.8 to 3.30. The calculations were guided by GVB-CAS results, which determine whether nearby configurations of the same symmetry type are more stable. To assure reliability, all symmetry types were computed, and both the ground and excited transition states were identified. Here a transition state is an energy minimum along the z axis, and the ground transition state is the state with the lowest energy minimum.

As table 3.1 indicates, several halogen-migration configurations did not lead to transition states but gave potentials that were purely repulsive in the region of calculation. In general, lack of identification of a transition state does not necessarily mean lack of existence. Rather it could simply mean that the transition state is not located within the computational subspace searched. However, my configurational search was sufficiently broad to identify two transition states for each halogen migration.

The configurations for the ground transition states are listed in tables 3.3.2 and 3.3.2. The unpaired electron's orbital could have been either symmetric or antisymmetric with respect to rotation about the z axis. Both cases were calculated, and the ground configuration was determined to be ^2A for the F migrations and Cl (1,2) migration and ^2B for the Cl (1,4) migration.

The H migrations were electronically simpler, as H contains no lone pairs. Only ^2B and $^2A''$ configurations were considered, and results are shown in tables 3.2 through 3.3.2. The GVB-CAS calculations confirmed that within this symmetry the assumed configurations dominated.

Atom	Migration	HF Configuration	E_a	z_a	Dominant GVB−CAS Configuration
Cl	(1,2)	$^2A(10,7)$	3.71 eV	2.20 Å	√
		$^2A(9,8)$	×	×	$^2A(10,7)$
		$^2B(9,8)$	3.72	2.00	√
		$^2B(10,7)$	×	×	$^2B(9,8)$
F	(1,2)	$^2A(8,5)$	4.68 eV	1.80 Å	√
		$^2A(7,6)$	×	×	$^2A(8,5)$
		$^2B(7,6)$	5.44	1.70	√
		$^2B(8,5)$	×	×	$^2B(8,5)/^2B(7,6)$
Cl	(1,4)	$^2B(13,12)$	2.29 eV	1.70 Å	√ [a]
		$^2B(14,11)$	×	×	div[b]
		$^2A(14,11)$	2.45	1.5	√
F	(1,4)	$^2A(12,9)$	3.41 eV	1.0 Å	√
		$^2B(11,10)$	4.65	1.40	√

[a] Preference of the HF orbital energies. The GVB-CAS calculation was not performed.

[b] The HF calculation preferred the $^2A(14,11)$ state, and the GVB-CAS calculation diverged due to the high HF energy.

Table 3.1: Calculated activation barriers, E_a, and geometries, z_a, for HF configurations near the ground state. √ denotes that the GVB-CAS calculation confirmed that the reference configuration dominated. × denotes that the potentials were purely repulsive in the region of calculation.

Atom	Migration	HF Configuration	E_a	z_a	Dominant GVB−CAS Configuration
H	(1,2)	$^2B(5,4)$	3.24 eV	1.14 Å	√
	(1,3)	$^2A''(8,5)$	3.56 eV	1.11 Å, 44°	√
	(1,4)	$^2B(9,8)$	2.24 eV	0.71 Å	√

Table 3.2: Calculated activation barriers, E_a, and geometries, z_a, for H migrations. The geometry for the (1,3) migration is given in terms of (r, θ) coordinates defined in figure 3.2b. √ denotes that the GVB-CAS calculation confirmed that the reference configuration dominated.

	H Migration		F Migration		Cl Migration	
	Symmetric	Antisymmetric	Symmetric	Antisymmetric	Symmetric	Antisymmetric
ϕ_{core}			F 1s		Cl 1s	
					Cl 2s	
	$C_1 1s + C_2 1s$	$C_1 1s - C_2 1s$	- - -	- - -	- - -	- - -
$\phi_{inactive}$	C_1-H_1 + C_2-H_2	C_1-H_1 − C_2-H_2	- - -	- - -	- - -	- - -
	C_1-H_3 + C_2-H_4	C_1-H_3 − C_2-H_4	- - -	- - -	- - -	- - -
	C_1-C_2		- - -		- - -	
			F 2s			
			F $2p_z$		Cl $2p_z$	Cl $2p_x$
						Cl $2p_y$
					Cl 3s	
					Cl $3p_z$	
ϕ_{active}				F $2p_x$ ↑↓		Cl $3p_x$ ↑↓
	C···H···C ↑↓	C* ↑	C···F···C ↑	F $2p_y$/C* ↑↓	C···Cl···C ↑	Cl $3p_y$/C* ↑↓
Total ϕ	5	4	8	5	10	7

Table 3.3: Ground transition-state configurations for (1,2) migrations, in terms of analogous bond and atomic orbitals. Labels for carbon and hydrogen centers are defined in fig. 3.6a. The core and inactive C-H orbitals are the same for all three cases. In the HF calculations all core and inactive orbitals are doubly-occupied, and the active orbitals denoted ↑↓ are doubly-, and those denoted ↑ are singly-, occupied. ϕ_{active} are active orbitals in the GVB-CAS and SD-CAS calculations of hydrogen migration and in the 5-in-5 SD-HF of halogen migrations.

	H Migration		F Migration		Cl Migration	
	Symmetric	Antisymmetric	Symmetric	Antisymmetric	Symmetric	Antisymmetric
ϕ_{core}			F 1s		Cl 1s	
	$C_{b1}1s + C_{b2}1s$	$C_{b1}1s - C_{b2}1s$	- - -	- - -	- - -	- - -
	$C_{t1}1s + C_{t2}1s$	$C_{t1}1s - C_{t2}1s$	- - -	- - -	- - -	- - -
					Cl 2s	Cl $2p_y$
					Cl $2p_z$	Cl $2p_x$
$\phi_{inactive}$	C_{b1}-H_{b1} + C_{b2}-H_{b2}	C_{b1}-H_{b1} − C_{b1}-H_{b2}	- - -	- - -	- - -	- - -
	C_{b1}-H_{b3} + C_{b2}-H_{b4}	C_{b1}-H_{b3} − C_{b2}-H_{b4}	- - -	- - -	- - -	- - -
	C_{b1}-C_{b2}		- - -		- - -	
	C_{b1}-C_{t1} + C_{b2}-C_{t2}	C_{b1}-C_{t1} − C_{b2}-C_{t2}	- - -	- - -	- - -	- - -
	C_{t1}-H_{t1} + C_{t2}-H_{t2}	C_{t1}-H_{t1} − C_{t1}-H_{t2}	- - -	- - -	- - -	- - -
	C_{t1}-H_{t3} + C_{t2}-H_{t4}	C_{t1}-H_{t3} − C_{t2}-H_{t4}	- - -	- - -	- - -	- - -
			F $2p_z$			
						Cl $3p_x$
						Cl $3p_y$
ϕ_{active}			F 2s ↑↓	F $2p_y$ ↑↓[a]	Cl 3s ↑↓	
	C···H···C ↑↓	C* ↑	C···F···C ↑	C* ↑↓	C···Cl···C ↑↓	C* ↑
Total ϕ	9	8	12	9	13	12

[a] This orbital would be inactive at the 5-in-5 level, but the F (1,4) transition state was calculated at the 7-in-7 SD-HF level.

Table 3.4: Ground transition-state configurations for (1,4) migrations, in terms of analogous bond and atomic orbitals. Labels for carbon and hydrogen centers are defined in fig. 3.6b. The core and inactive C-H orbitals are the same for all three cases. In the HF calculations all core and inactive orbitals are doubly-occupied, and the active orbitals denoted ↑↓ are doubly-, and those denoted ↑ are singly-, occupied. ϕ_{active} are active orbitals in the GVB-CAS and SD-CAS calculations of hydrogen migration and in the 5-in-5 SD-HF of halogen migrations.

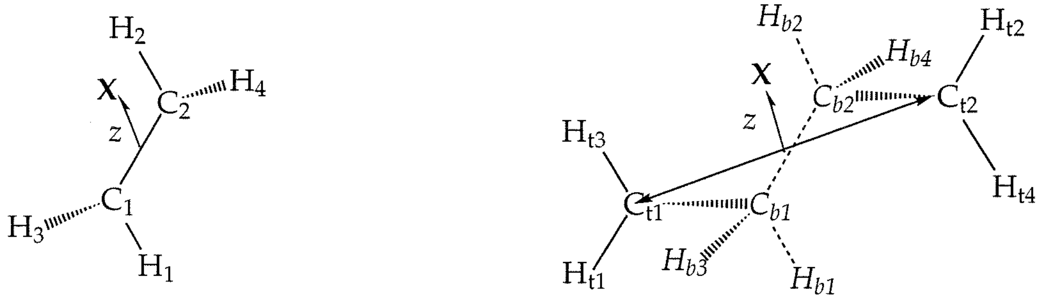

(a) (1,2) migration

(b) (1,4) migration

Figure 3.6: Labels of atomic centers in transition-state clusters for (1,2) and (1,4) migrations. X represents H, F, or Cl, and (110) lies in the plane of the paper. The origin is located at the midpoint between the two surface carbons. The z axis is perpendicular to the surface (110) plane.

3.3.3 Activation energies

The predicted activation energies are shown in table 3.5. The calculated barriers are upper bound to the actual barriers, and the computational precision is about 0.1 eV for the H (1,4) migration and 0.05 eV for all other migrations. The barrier height for (1,4) migrations is at least 1 eV lower than for (1,2) and (1,3) migrations for all three systems. This is consistent with combustion experiments, where (1,4) hydrogen migrations occur while (1,2) and (1,3) migrations remain too slow to be detected [27].

Migration	(1,2)	(1,3)	(1,4)
H	3.24 eV	3.56 eV	2.24 eV
Cl	3.71	—	2.29
F	4.68	—	3.41

Table 3.5: Calculated activation energies for surface migrations. The calculations are performed at the SD-CAS level for hydrogen migrations, and at the SD-HF level for halogen migrations. Barriers to (1,3) migration of Cl and F were not calculated.

Migration	(1,2)	(1,3)	(1,4)
τ_H	3.2 sec	95 sec	180×10^{-6} sec
τ_{Cl}	440	—	340×10^{-6}
τ_F	6×10^6	—	200

Table 3.6: Order-of-magnitude estimates of characteristic times for surface migrations at 900°C.

3.4 Analysis

Since migration reactions are unimolecular and gas-surface reactions are bimolecular, rate comparisons must account for concentration and frequency factors in addition to barrier heights. Accounting for pre-exponential factors and barrier heights, order-of-magnitude estimates were obtained for the characteristic migration times. This was the first study [1] to compare characteristic times directly instead of only barrier heights. Previous studies [2, 28] had obtained "extrordinarily high" barriers to migration and were not able to establish its competitiveness with gas-surface reactions.

3.4.1 Predicted characteristic migration times

The predicted activation barriers are converted to characteristic migration times using the approximate transition-state theory expression

$$\tau^{-1} \simeq \frac{k_B T}{h} e^{-E_a/k_B T}, \tag{3.5}$$

where τ is the characteristic migration time, E_a is the activation energy (from table 3.5), k_B is Boltzmann's constant, T is the temperature (1173 K), and h is Planck's constant. This simple expression for the pre-exponential factor may be in error by a factor of about five. Moreover, the barrier height on a real diamond surface may be lower than our computed E_a due to the cluster approximations and their overly-constrained geometries. Thus these estimates for τ may be in error by an order of magnitude. The predicted migration times are shown in table 3.6.

3.4.2 Comparison of migration times to thermal desorption times

For migration to be significant in diamond surface science, it must compete with thermal desorption. Although the rates of halogen desorptions are unknown, Butler *et al.* [29] have measured the rate of hydrogen desorption from C(110). The corresponding desorption time is calculated from $\tau = 1/k_d$, where $k_d = Ae^{-E_d/kT}$ is the desorption rate constant. Figure 3.7 compares the temperature dependence of the hydrogen (1,4) migration time with that of the surface desorption time. Here the (1,4) migration times are calculated by equation 3.5, which is an order-of-magnitude estimate. The migration times shown in fig. 3.7 are several orders of magnitude faster than desorption times. Therefore the (1,4) migration of hydrogen is sufficiently fast to occur before desorption and sufficiently fast to pre-pair the hydrogens for desorption.

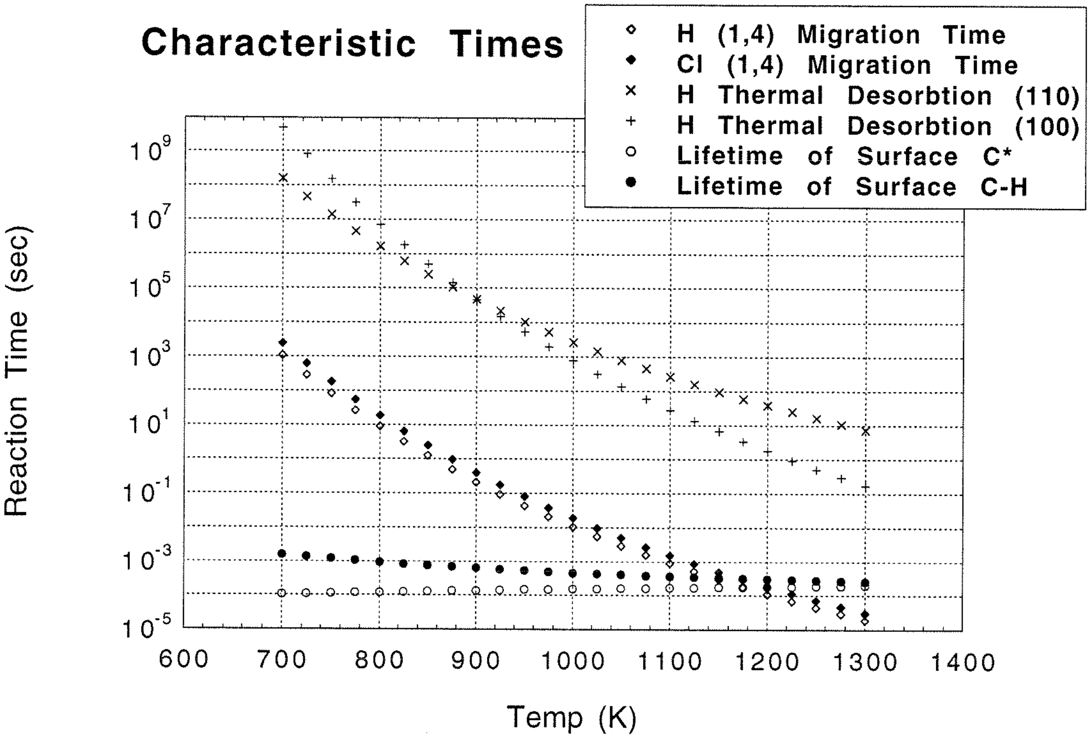

Figure 3.7: Estimated characteristic reaction times.

3.4.3 Comparison of migration times to gas-surface reaction times

For surface migration to be significant during growth, it must compete with gas-surface reactions. Otherwise, a surface hydrogen will be abstracted by gas-phase atomic hydrogen before it has a chance to migrate. Alternatively, a surface radical site will disappear upon recombination with a gas-phase hydrogen atom before a neighboring H can hop into this site. The characteristic lifetimes of surface hydrogen and radical sites are unknown for C(110). However, Belton and Harris [13] have estimated reaction rates for the (110) surface, using rate constants for analogous gas-phase reactions. The corresponding lifetimes are shown in table 3.7. These are order-of-magnitude estimates, calculated using $\tau^{-1} = k_f \times [\mathrm{H}^{\mathrm{gas}}]$, where k_f is the forward rate constant at 900°C (taken from table I, reactions (2) and (3) of ref [13].), and $[\mathrm{H}^{\mathrm{gas}}]$ is the gas-phase concentration of atomic hydrogen just above the surface.

$[\mathrm{H}^{\mathrm{gas}}]$ is taken to be 5.5×10^{-10} mol/cm^3 at 20 torr [30].

Gas-Surface Reaction	τ
$\mathrm{H}^{\mathrm{gas}} + \mathrm{C{-}H}^{\mathrm{surf}} \rightarrow \mathrm{H}_2^{\mathrm{gas}} + \mathrm{C}{*}^{\mathrm{surf}}$	320 μs
$\mathrm{H}^{\mathrm{gas}} + \mathrm{C}{*}^{\mathrm{surf}} \rightarrow \mathrm{C{-}H}^{\mathrm{surf}}$	180 μs

Table 3.7: Order-of-magnitude estimates of characteristic times (τ) per surface site for gas-surface reactions at 900°C [13].

The gas-surface reaction times are four to six orders of magnitude faster than any of the (1,2) or (1,3) migration times. Thus these migrations are too slow to play a role in CVD of diamond. The characteristic time for (1,4) migration of F is also too slow. However, our estimates for the (1,4) migration times of H and Cl are within the uncertainty of the estimated surface site lifetimes. *Thus (1,4) migration of both H and Cl is sufficiently fast to compete with gas-surface reactions and play a role in diamond CVD.*

A sequence of (1,4) migrations down zig-zagged carbon chains yields diffusion in the $[1\bar{1}0]$ direction, whereas a series of (1,2) hops across carbon chains followed by (1,4) hops between chains yields diffusion in the [001] direction. Thus table 3.6 indicates that diffusion occurs at least 10^4 times faster in the $[1\bar{1}0]$ direction than in [001]. Although migration may occur in diamond CVD, we do not expect long-range surface transport. It is interesting to note that if other growth conditions could be found where surface diffusion dominated, this anisotropy would greatly enhance surface transport from terraces to steps with edges parallel to [001]. The [001] steps would then be rough and grow at a much higher rate than the smooth $[1\bar{1}0]$ steps.

Figure 3.7 compares the temperature dependence of the hydrogen (1,4) migration time with that of gas-surface reaction times. Here the (1,4) migration times are estimated by equation 3.5. The gas-surface reaction times are calculated using $\tau = k_f \times [\mathrm{H}^{\mathrm{gas}}]$, with $[\mathrm{H}^{\mathrm{gas}}] = [\mathrm{H}^{\mathrm{gas}}](1173\mathrm{K}) \times 1173/T$ (K) (ideal gas). This is an order-of-magnitude estimate, since it does not account for chemical reactions which may modify the temperature dependence of $[\mathrm{H}^{\mathrm{gas}}]$. Nevertheless, the gas-surface reaction times and migration times shown in fig. 3.7 are comparable only at surface temperatures where diamond grows, i.e. 700°C to 1000°C. This suggests the possibility that the temperature for diamond growth must be sufficiently high for (1,4) migration to be activated. Possible roles of migration include annealing the surface, allowing it to relax from strained structures, and increasing methyl incorporation rate relative to desorption rate by allowing surface hydrogens near the adsorbed methyl to move away and decrease the steric crowding of the methyl.

3.5 Conclusions

Ab initio calculations were carried out to estimate activation energies for the migration of H, F, and Cl on the diamond (110) surface, or (110)-like sites on steps on other surfaces. Accounting for pre-exponential factors and barrier heights, order-of-magnitude estimates were obtained for the characteristic migration times. This was the first study [1] to compare characteristic times directly instead of only barrier heights. The estimated times for (1,4) migration of both H and Cl are of order 10^{-4} s. Under UHV conditions, these characteristic migration times are orders of magnitude faster than characteristic thermal-desorption times. Therefore (1,4) migration is sufficiently fast to pre-pair the surface hydrogen, allowing first-order desorption kinetics. Under diamond CVD conditions, the characteristic times for (1,4) migrations of H and Cl are of the same order of magnitude as estimated surface-site lifetimes. Therefore (1,4) migrations of H and Cl are sufficiently fast relative to gas-surface reactions to play a role in diamond CVD.

After this work was published [31] several groups investigated the potential role of migration in diamond CVD. In the case of growth on the (100) surface, direct-simulation kinetic Monte Carlo studies [32] found that surface migration opened a pathway for pi-bonded sites to grow to bridged sites four to six orders of magnitude faster than the rate at which isolated radical sites grew without migration. Other simulations [33] found migration to be a key step in enabling atomically smooth growth of the (100) surface.

3.6 Acknowledgements

Useful discussions with Jason K. Perry are gratefully acknowledged. This work was supported in part by the Office of Naval Research under contract N00014-90-J-1386. The computer facilities for the studies were supported by grants from the National Science Foundation (CHE 91-00284, GCAG ASC-9217368).

Bibliography

[1] M. S. Melnik, D. G. Goodwin and W. A. Goddard, III, "Hydrogen migration on the diamond (110) surface." In *Adventures in Solid-State Research*, edited by F. Grunthaner, Southern California American Vacuum Society Symposium, Pasadena, CA (1992).

[2] J. P. Lopez and W. H. Fink, "Ab-initio model cluster calculations of hydrogen atom diffusive motion across the (100) face of diamond." J. Phys. Chem. **86**, 2850–2853 (1982).

[3] R. E. Thomas, R. A. Rudder and R. J. Markunas, "Thermal desorption from hydrogenated and oxygenated diamond (100) surfaces." J. Vac. Sci. Technol. A **10**, 2451–2457 (1992).

[4] A. V. Hamza, G. D. Kubiak and R. H. Stulen, "Hydrogen chemisorption and the structure of the diamond C(100)-(2x1) surface." Surf. Sci. **237**, 35–52 (1990).

[5] J. J. Boland, "Evidence of pairing and its role in the recombinative desorption of hydrogen from the Si(100)-2×1 surface." Phys. Rev. Lett. **67**, 1539–1542 (1991).

[6] S. P. Mehandru and A. B. Anderson, "Adsorption of H, CH_3, CH_2 and C_2H_2 on (2×1) restructured diamond (100)—Theoretical study of structures, bonding, and migration." Surf. Sci. **248**, 369–381 (1991).

[7] M. Frenklach and K. E. Spear, "Growth of vapor-deposited diamond." J. Mat. Res. **3**, 133–140 (1988).

[8] X. Y. Chang, D. L. Thompson and L. M. Raff, "Minimum-energy paths for elementary reactions in low-pressure diamond-film formation." J. Phys. Chem. **97**, 10112–10118 (1993).

[9] M. Tsuda, M. Nakajima and S. Oikawa, "Epitaxial growth mechanism of diamond crystal in CH_4-H_2 plasma." J. Am. Chem. Soc. **108**, 5780–5783 (1986).

[10] S. J. Harris, "Mechanism for diamond growth from methyl radicals." Appl. Phys. Lett. **56**, 2298–2300 (1990).

[11] D. G. Goodwin, "Scaling laws for diamond chemical-vapor deposition. II. Atomic hydrogen transport." J. Appl. Phys. **74**, 6895–6906 (1993).

[12] D. E. Patterson, B. J. Bai, C. J. Chu, R. H. Hauge and J. L. Margrave. In *Proc. 2nd Intl. Conf. New Diamond Sci. Tech.*, edited by R. Messier, J. T. Glass, J. E. Butler and R. Roy, Materials Research Society, Pittsburgh, PA (1991), pp. 433–438. Also B. J. Bai, C. J. Chu, D. E. Patterson, R. H. Hauge, and J. L. Margrave, *J. Mat. Res.*, 8: p. 233 (1993).

[13] D. N. Belton and S. J. Harris, "A mechanism for growth on diamond (110) from acetylene." J. Chem. Phys. **96**, 2371–2377 (1992).

[14] M. S. Melnik, D. G. Goodwin and W. A. Goddard, III, "*Ab initio* quantum chemical studies of hydrogen and halogen migration on the diamond (110) surface." Mat. Res. Soc. Symp. Proc. **317**, 349–354 (1994). The hydrogen migration calculations were first published in the 1991 Annual Report of the Materials and Molecular Simulation Center, California Institute of Technology (1992), pp. 163–164.

[15] D. Huang and M. Frenklach, "Energetics of surface reactions on (100) diamond plane." J. Phys. Chem. **96**, 1868–1875 (1992).

[16] M. W. Geis. In *Diamond, Silicon Carbide and Related Wide Bandgap Semiconductors*, edited by J. T. Glass, R. Messier and N. Fujimori, Materials Research Society, Pittsburgh, PA (1990), pp. 15–22. Also C. J. Chu, M. P. D'Evelyn, R. H. Hauge, *J. Appl. Phys.*, 70(3): 1695 (1991).

[17] M. S. Melnik and D. G. Goodwin, "Chlorine and fluorine migration on the diamond (110) surface." Bull. Am. Phys. Soc. **38**, 573 (March 1993).

[18] J. Hinze and C. C. J. Roothaan. Prog. of Theor. Phys. Suppl. **40**, 37–51 (1967).

[19] T. H. Dunning, "Gaussian basis functions for use in molecular calculations. I. Contraction of (9s5p) atomic basis sets for the first-row atoms." J. Phys. Chem. **53**, 2823–2833 (1970).

[20] S. Huzinaga, "Gaussian-type functions for polyatomic systems. I." J. Phys. Chem. **42**, 1293–1302 (1965).

[21] S. Huzinaga and Y. Sakai, "Gaussian-type functions for polyatomic systems. II." J. Phys. Chem. **50**, 1371–1381 (1969).

[22] T. H. Dunning, "Gaussian basis sets for use in correlated molecular calculations. I. The atoms boron through neon and hydrogen." J. Phys. Chem. **90**, 1007–1023 (1989).

[23] A. D. McLean and G. S. Chandler, "Contracted Gaussian basis sets for molecular calculations. I. Second-row atoms, Z=11–18." J. Phys. Chem. **72**, 5639–5648 (1980).

[24] MOLECULE/SWEDEN is a system of electronic structure codes written by J. Almlöf, C. W. Bauschlicher, M. R. A. Blomberg, D. P. Chong, A. Heiberg, S. R. Langhoff, P. A. Malmqvist, A. P. Rendell, B. O. Roos, P. E. M. Siegbahn, P. R. Taylor.

[25] R. C. Weast, M. J. Astle and W. H. Beyer, eds., *CRC Handbook of Chemistry and Physics*. CRC Press, Inc. (66th edition, 1985). See page F–165.

[26] B. Engels, S. D. Peyerimhoff and P. S. Skell, "Theoretical study of the potential energy surface governing the stereochemistry in ClC_2H_4 reactions." J. Phys. Chem. **94**, 1267–1275 (1990).

[27] L. B. Harding, "Ab initio studies of (1,2)-hydrogen migrations in open-shell hydrocarbons: Vinyl radical, ethyl radical, and triplet methylcarbene." J. Am. Chem. Soc. **103**, 7469–7475 (1981).

[28] M. S. Melnik, D. G. Goodwin and W. A. Goddard, III, "H migration on diamond surfaces." In *Materials and Molecular Simulation Center 1991 Annual Report*, edited by W. A. Goddard, III and S. Dasgupta, Pasadena, CA (1992), pp. 163–164.

[29] J. E. Butler, B. D. Thoms, M. McGonigal, J. N. Russell, Jr. and P. E. Pehrsson, "Hydrogen chemistry on diamond surfaces." In *Wide Band Gap Electronic Materials*, edited by M. A. Prelas *et al.*, Kluwer Academic Publishers, the Netherlands (1995), pp. 105–114.

[30] W. L. Hsu, "Mole fractions of H, CH_3, and other species during filament-assisted diamond growth." Appl. Phys. Lett. **59**, 1427–1429 (1991).

[31] M. S. Melnik, D. G. Goodwin and I. Goddard, W. A., "*Ab initio* quantum chemical studies of hydrogen and halogen migration on the diamond (110) surface." Mat. Res. Soc. Symp. Proc. **317**, 349–354 (1994).

[32] E. J. Dawnkaski, D. Srivastava and B. J. Garrison, "Time dependent Monte Carlo simulations of H reactions on the diamond $\{001\}(2\times1)$ surface under chemical vapor deposition conditions." J. Chem. Phys. **102**, 9401–9411 (1995).

[33] S. Skokov, B. Weiner and M. Frenklach, "Elementary reaction mechanism for growth of diamond (100) surfaces from methyl radicals." J. Phys. Chem. **98**, 7073–7082 (1994).

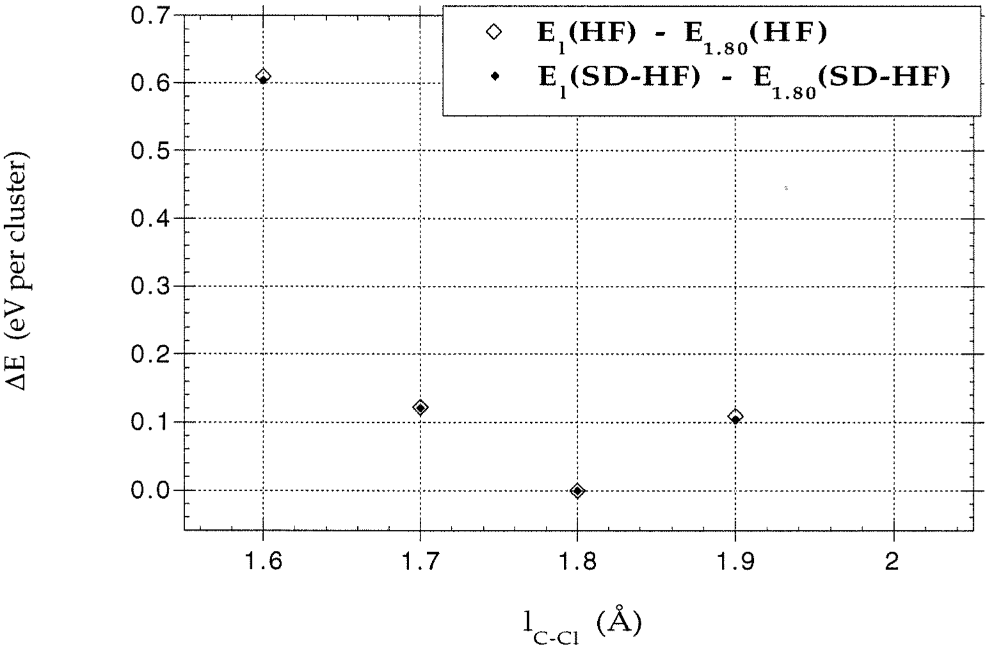

Figure 3.8: Computed potentials of the reactant state for (1,2) Cl migration. The SD-HF was 5-in-5. l_{C-Cl} is the length of the active C-Cl bond.

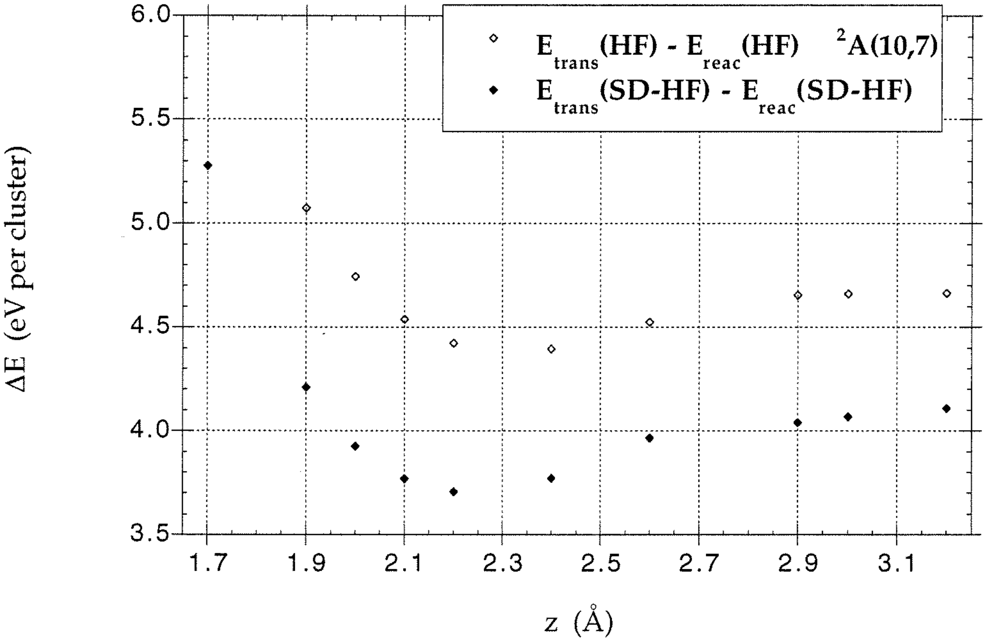

Figure 3.9: Computed potentials of the ground transition state for (1,2) Cl migration. The HF configuration was $^2A(10,7)$, the GVB-CAS calculation was 7-in-7, and the SD-HF was 5-in-5. The z axis is defined in fig. 3.1 .

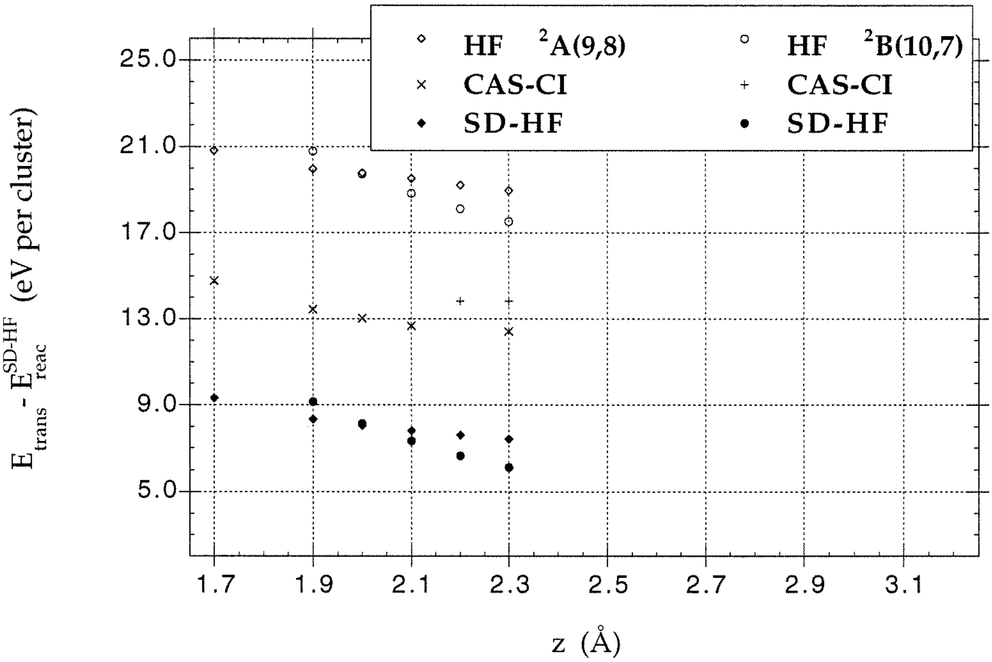

Figure 3.10: Computed potentials of repulsive states for (1,2) Cl migration. The HF configurations were ^2A(9,8) and ^2B(10,7), and the GVB-CAS calculations were 7-in-7, and the SD-HFs were 5-in-5. The z axis is defined in fig. 3.1 .

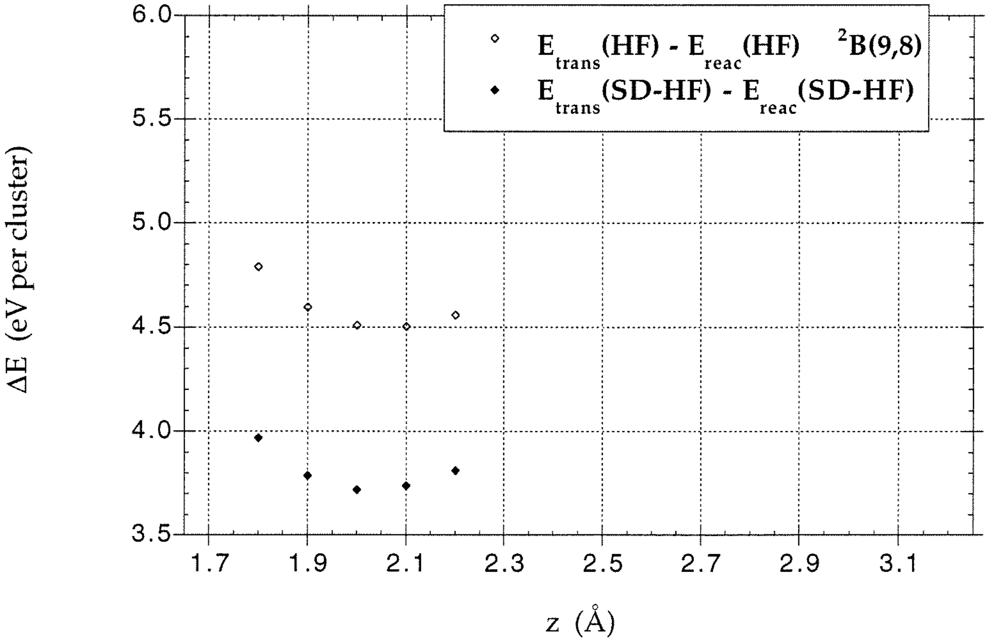

Figure 3.11: Computed potentials of an excited transition state for (1,2) Cl migration. The HF configuration was ^2B(9,8), and the SD-HF was 5-in-5. The z axis is defined in fig. 3.1 .

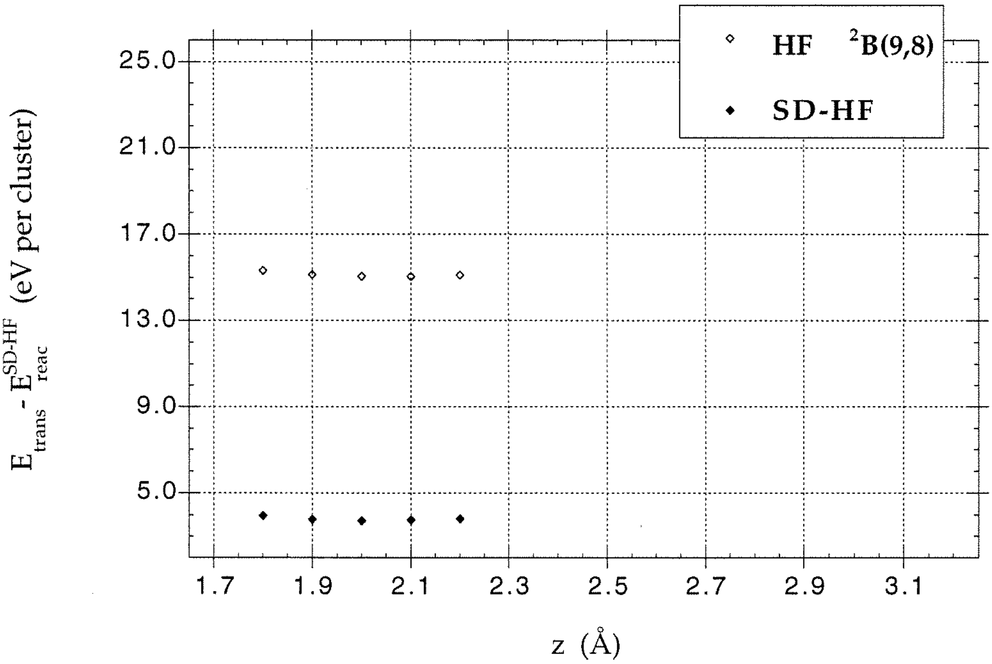

Figure 3.12: Computed potentials of an excited transition state for (1,2) Cl migration. The HF configuration was $^2B(9,8)$, and the SD-HF was 5-in-5. The z axis is defined in fig. 3.1 .

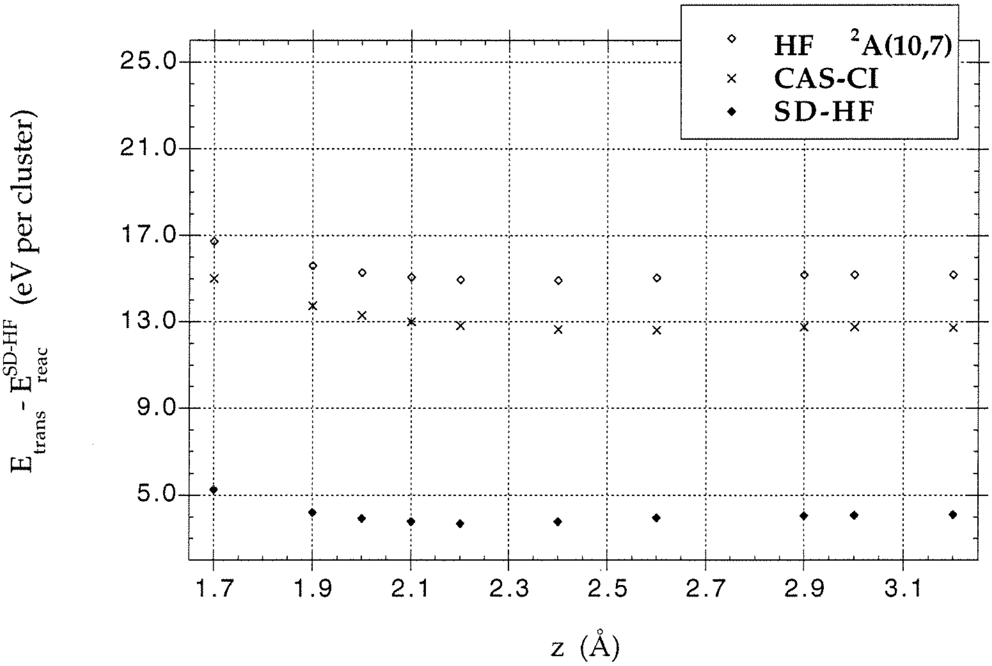

Figure 3.13: Computed potentials of the ground transition state for (1,2) Cl migration. The HF configuration was $^2A(10,7)$, the GVB-CAS calculation was 7-in-7, and the SD-HF was 5-in-5. The z axis is defined in fig. 3.1 .

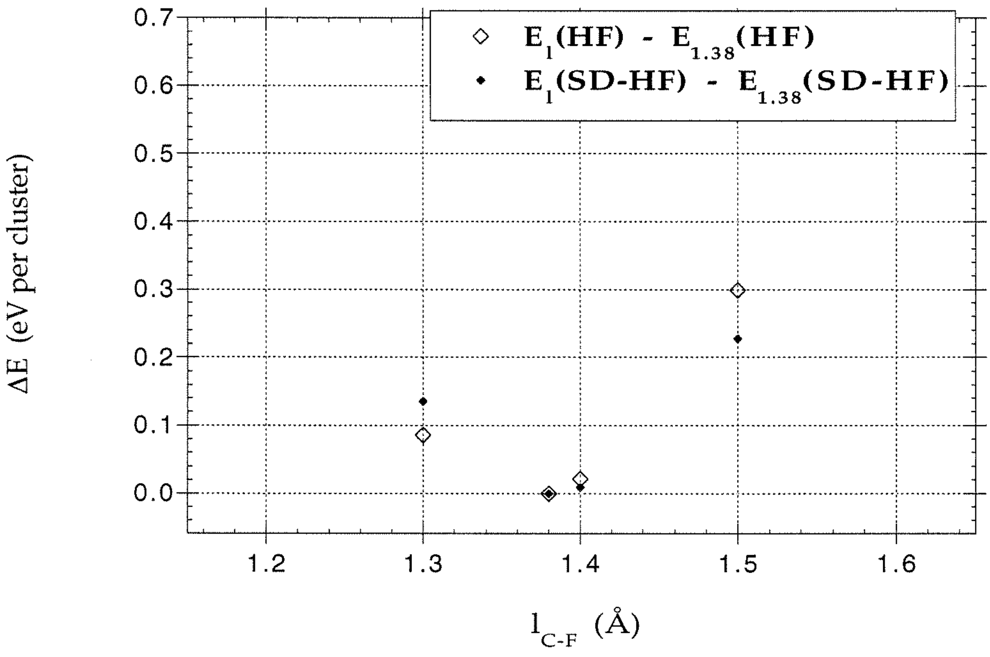

Figure 3.14: Computed potentials of the reactant state for (1,2) F migration. The SD-HF was 5-in-5. l_{C-F} is the length of the active C-F bond.

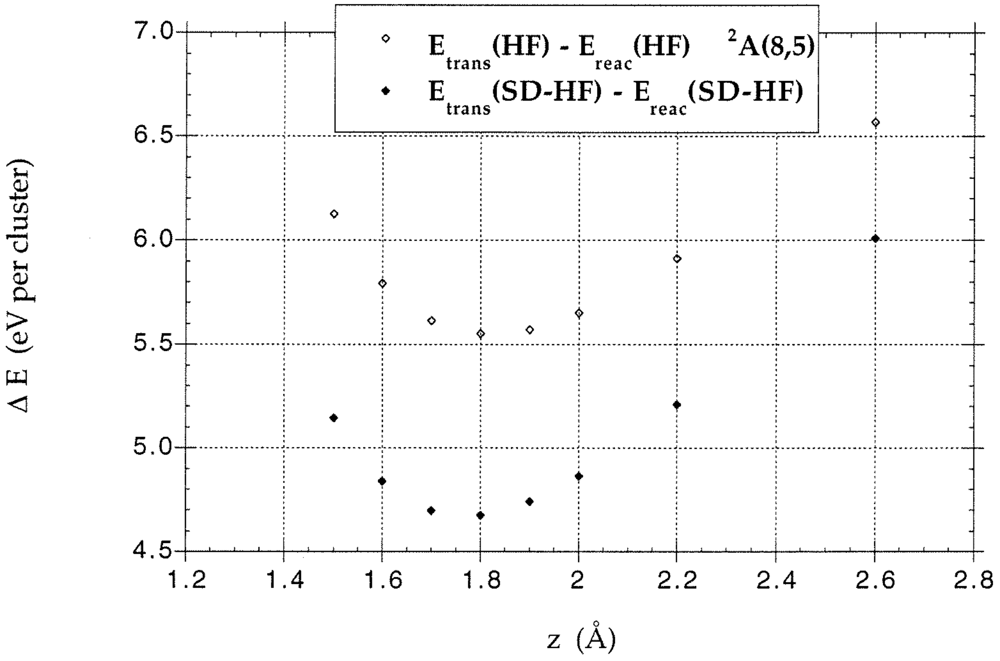

Figure 3.15: Computed potentials of the ground transition state for (1,2) F migration. The HF configuration was $^2A(8,5)$, and the SD-HF was 5-in-5. The z axis is defined in fig. 3.1 .

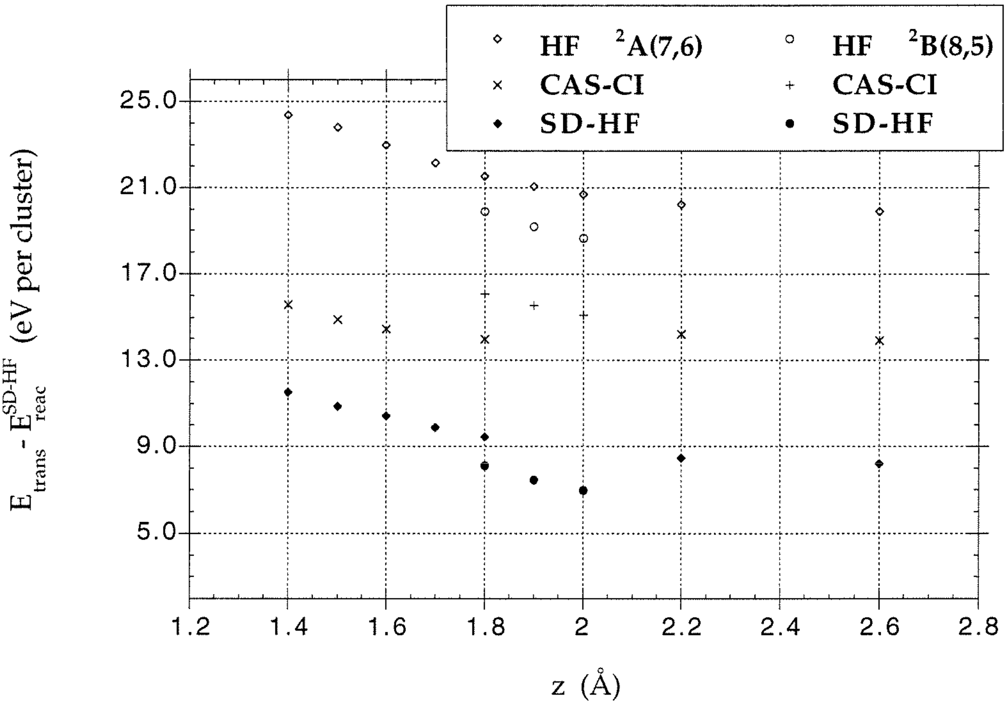

Figure 3.16: Computed potentials of repulsive states for (1,2) F migration. The HF configurations were ^2A(7,6) and ^2B(8,5), the GVB-CAS calculations were 7-in-7, and the SD-HFs were 5-in-5. The z axis is defined in fig. 3.1 .

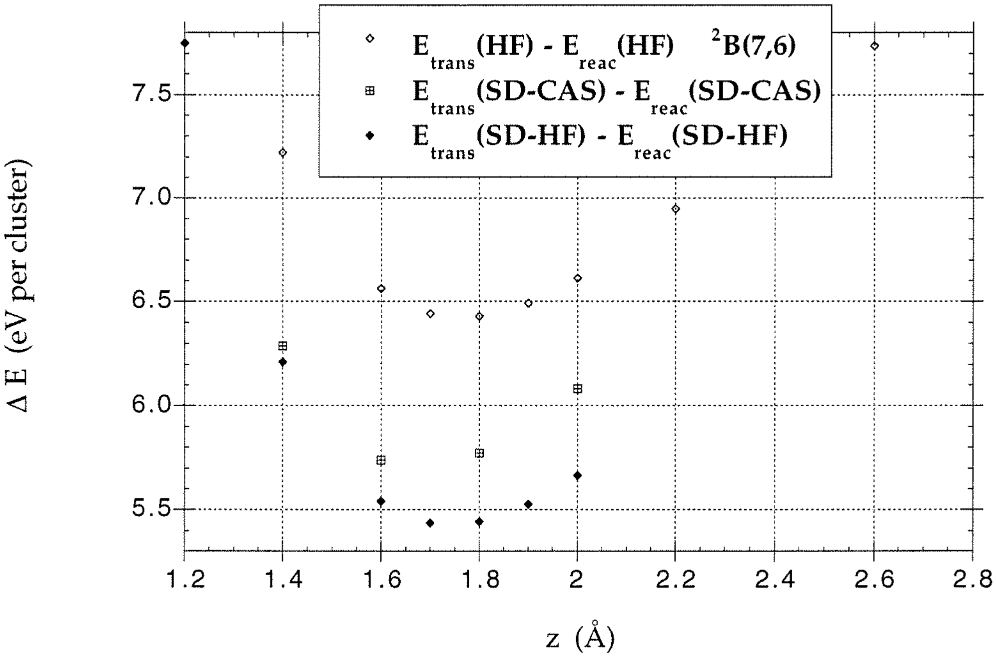

Figure 3.17: Computed potentials of an excited transition state for (1,2) F migration. The HF configuration was $^2B(7,6)$, the GVB-CAS was 5-in-5, and the SDs were 5-in-5. The z axis is defined in fig. 3.1 .

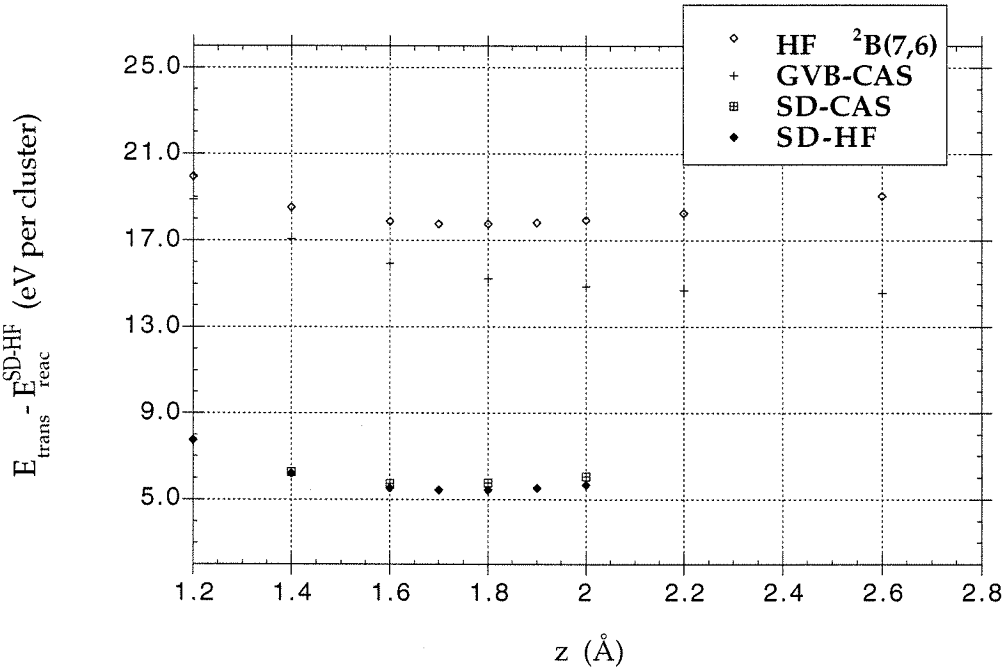

Figure 3.18: Computed potentials of an excited transition state for (1,2) F migration. The HF configuration was $^2B(7,6)$, the GVB-CAS was 5-in-5, and the SDs were 5-in-5. The z axis is defined in fig. 3.1 .

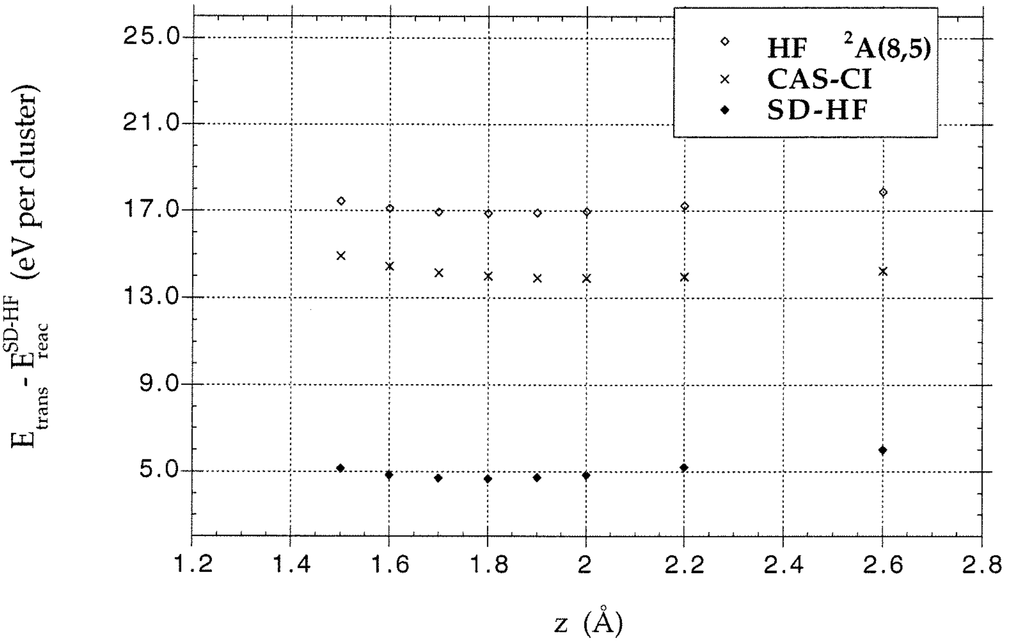

Figure 3.19: Computed potentials of the ground transition state for (1,2) F migration. The HF configuration was $^2A(8,5)$, the CAS-CI was 7-in-7, and the SD-HF was 5-in-5. The z axis is defined in fig. 3.1 .

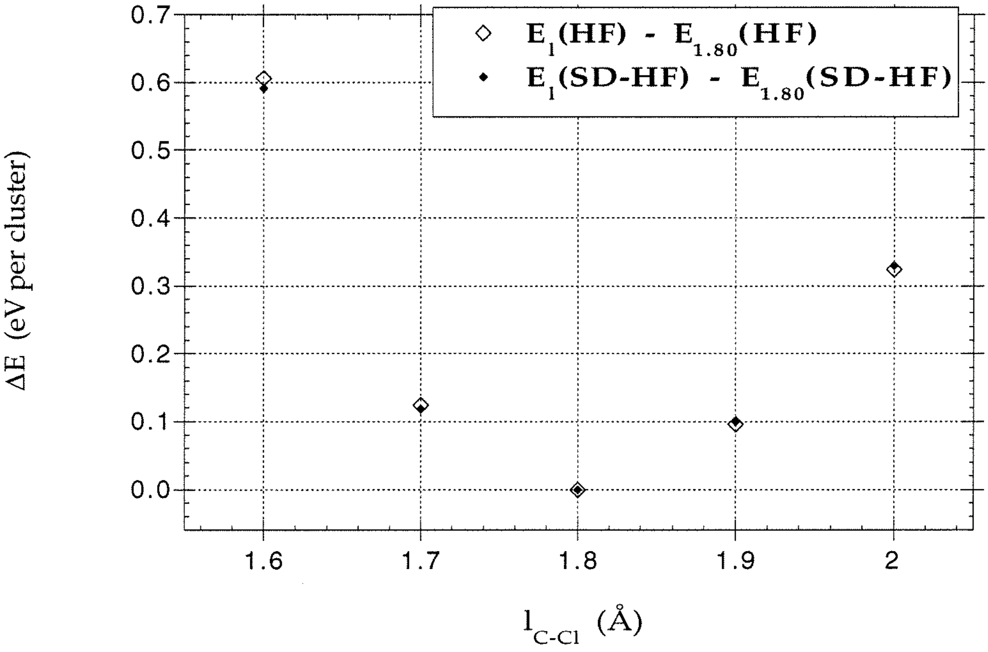

Figure 3.20: Computed potentials of the reactant state for (1,4) Cl migration. The SD-HF was 5-in-5. l_{C-Cl} is the length of the active C-Cl bond. 7-in-5 SD-HF calculations were also performed at $l_{C-Cl} = 1.80$, and the energy was the same as the 5-in-5 energy.

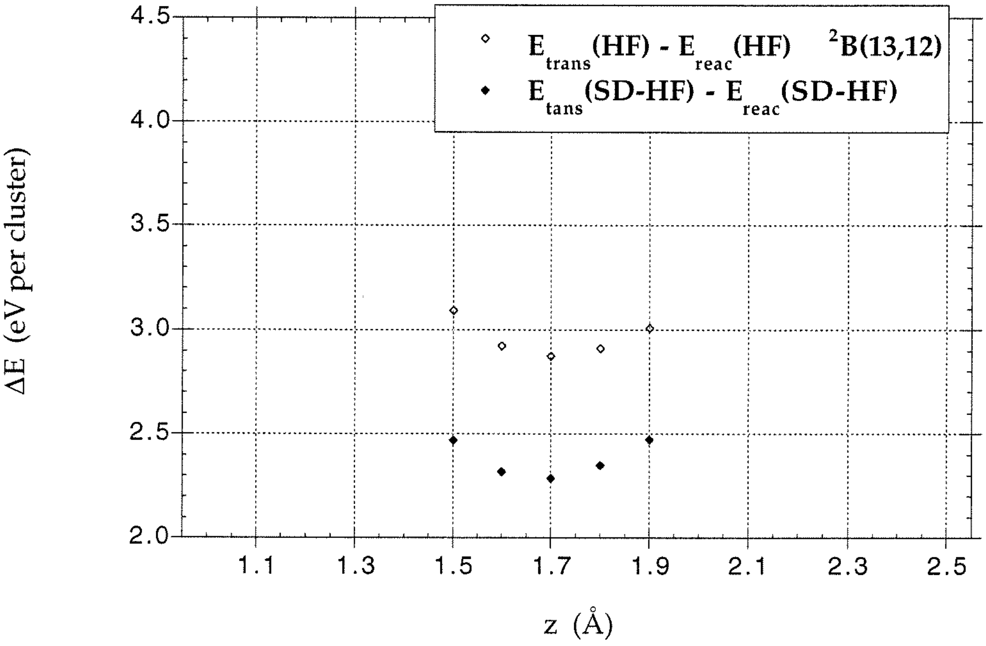

Figure 3.21: Computed potentials of the ground transition state for (1,4) Cl migration. The HF configuration was ^2B(13,12), and the SD-HF was 5-in-5. The z axis is defined in fig. 3.3. 7-in-5 SD-HF calculations were also performed at $z = 1.90$, and the energy was the same as the 5-in-5 energy.

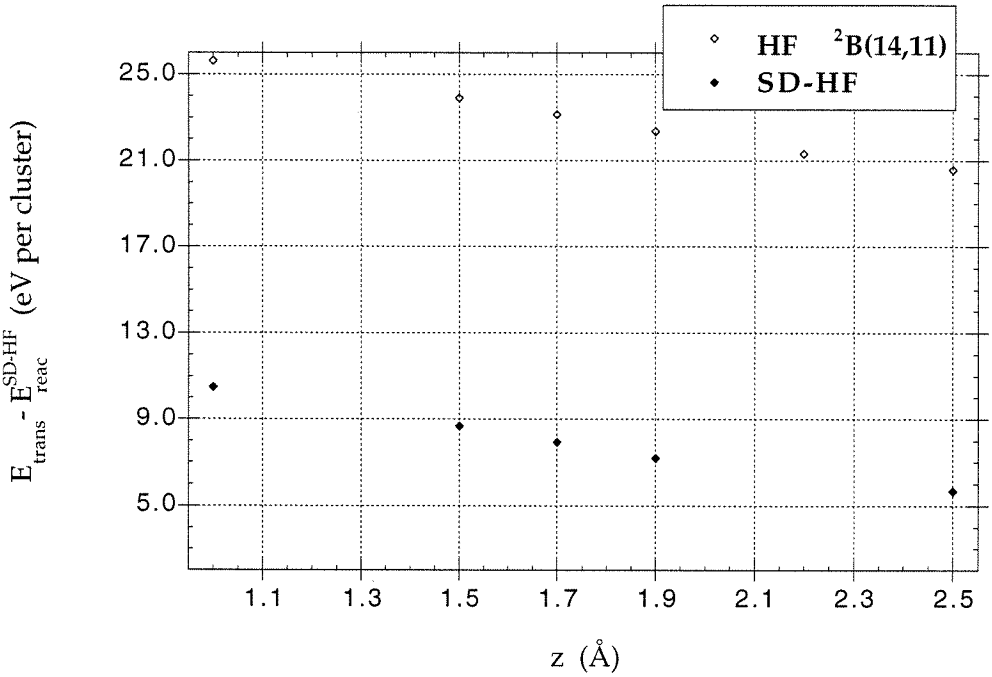

Figure 3.22: Computed potentials of repulsive state for (1,4) Cl migration. The HF configuration was ^2B(14,11), and the SD-HF was 9-in-5. The z axis is defined in fig. 3.3 .

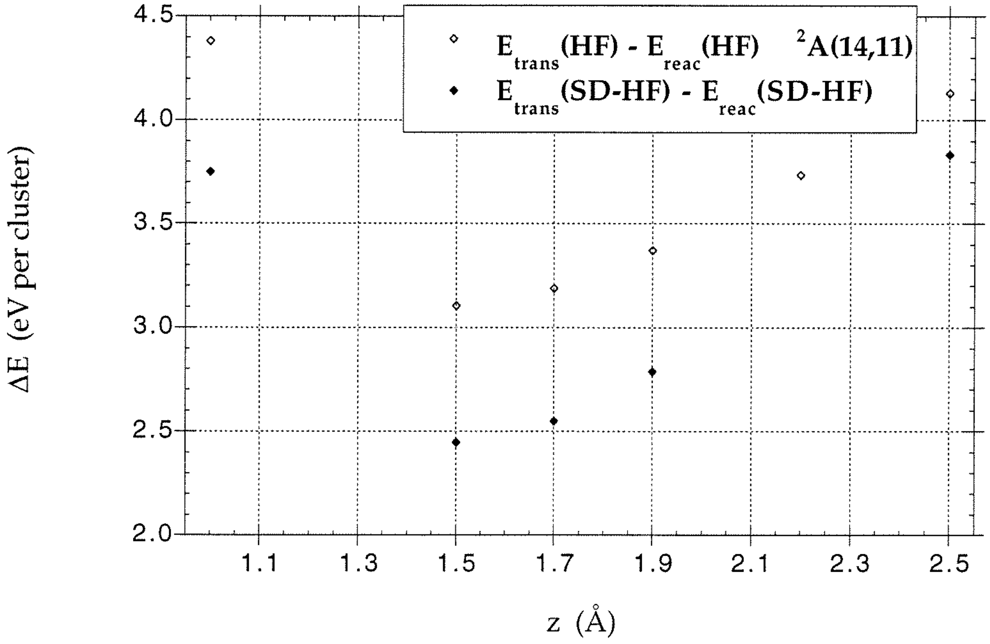

Figure 3.23: Computed potentials of an excited transition state for (1,4) Cl migration. The HF configuration was ^2A(14,11), and the SD-HF was 9-in-5. The z axis is defined in fig. 3.3 .

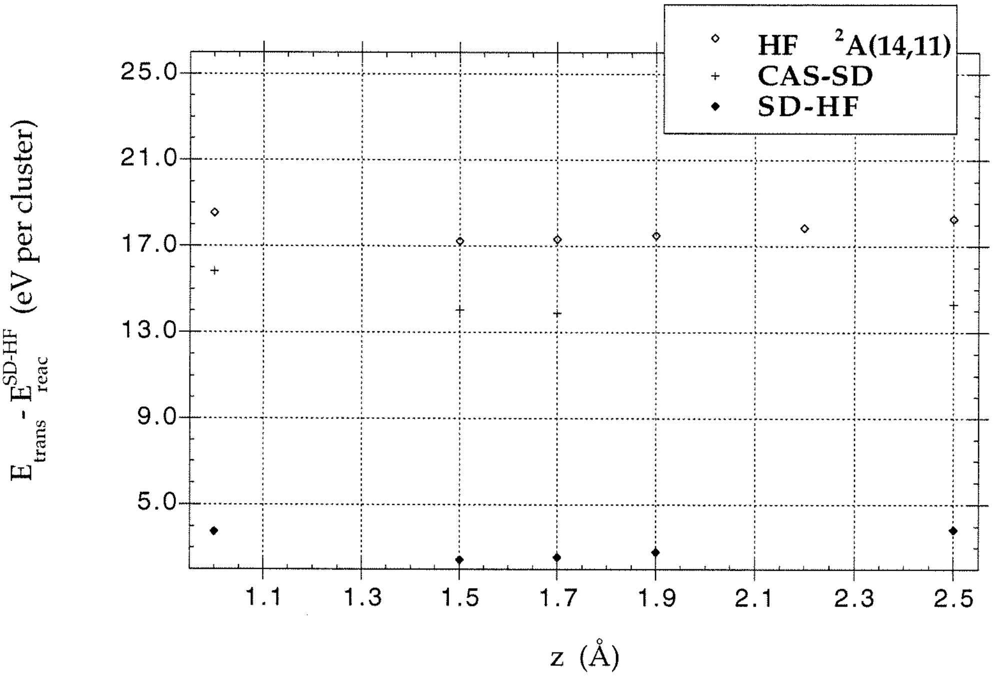

Figure 3.24: Computed potentials of an excited transition state for (1,4) Cl migration. The HF configuration was ^2A(14,11), the CAS-CI was 11-in-11, and the SD-HF was 9-in-5. The z axis is defined in fig. 3.3 .

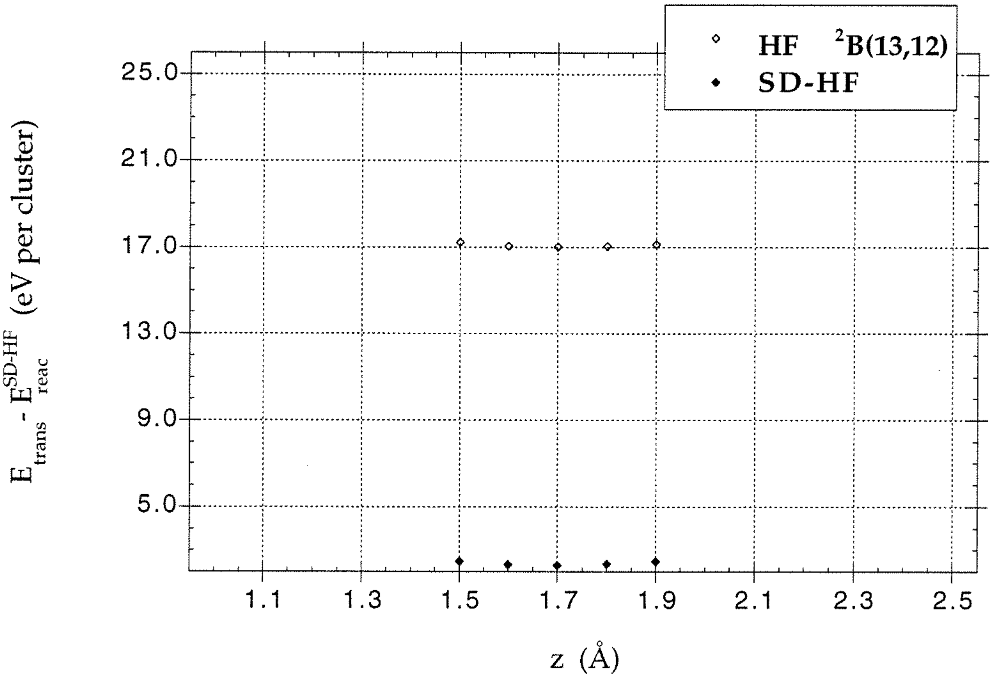

Figure 3.25: Computed potentials of the ground transition state for (1,4) Cl migration. The HF configuration was ^2B(13,12), and the SD-HF was 5-in-5. The z axis is defined in fig. 3.3 .

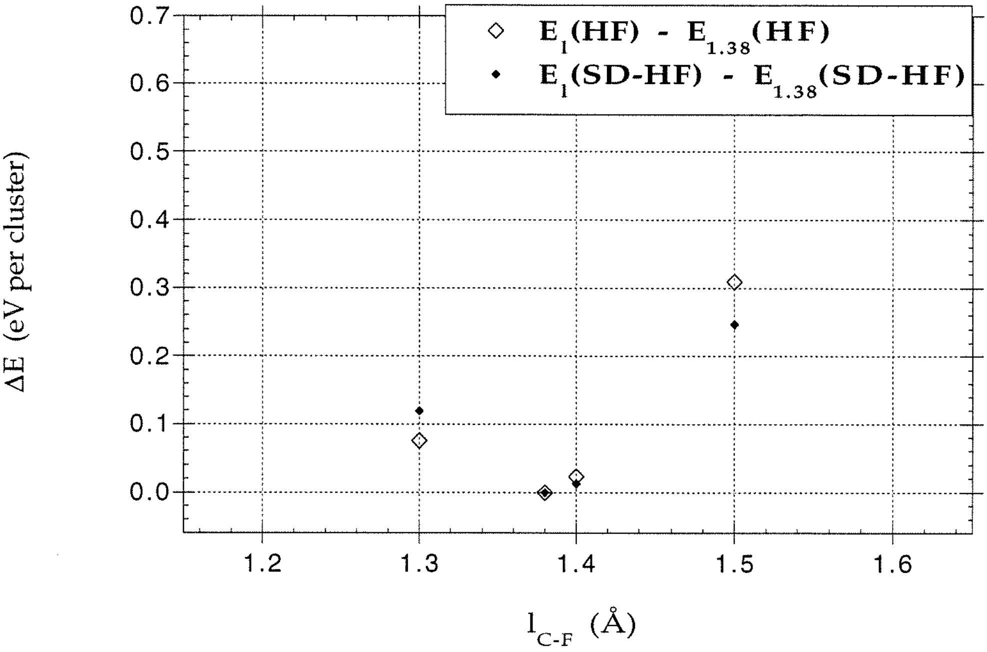

Figure 3.26: Computed potentials of the reactant state for (1,4) F migration. The SD-HF was 5-in-5. l_{C-F} is the length of the active C-F bond.

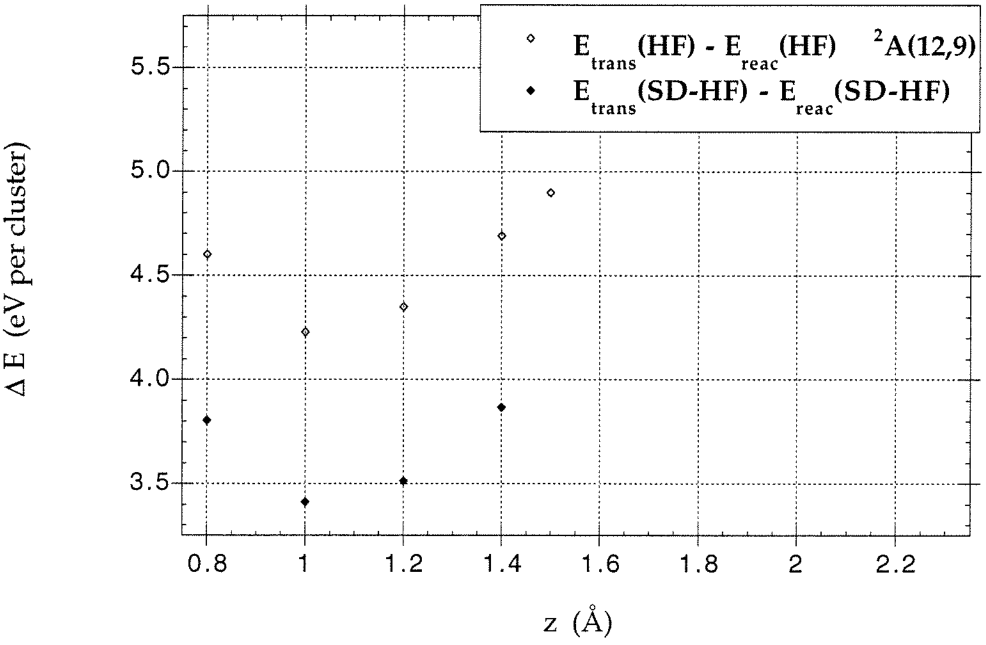

Figure 3.27: Computed potentials of the ground transition state for (1,4) F migration. The HF configuration was $^2A(12,9)$, and the SD-HF was 7-in-7. The z axis is defined in fig. 3.3 .

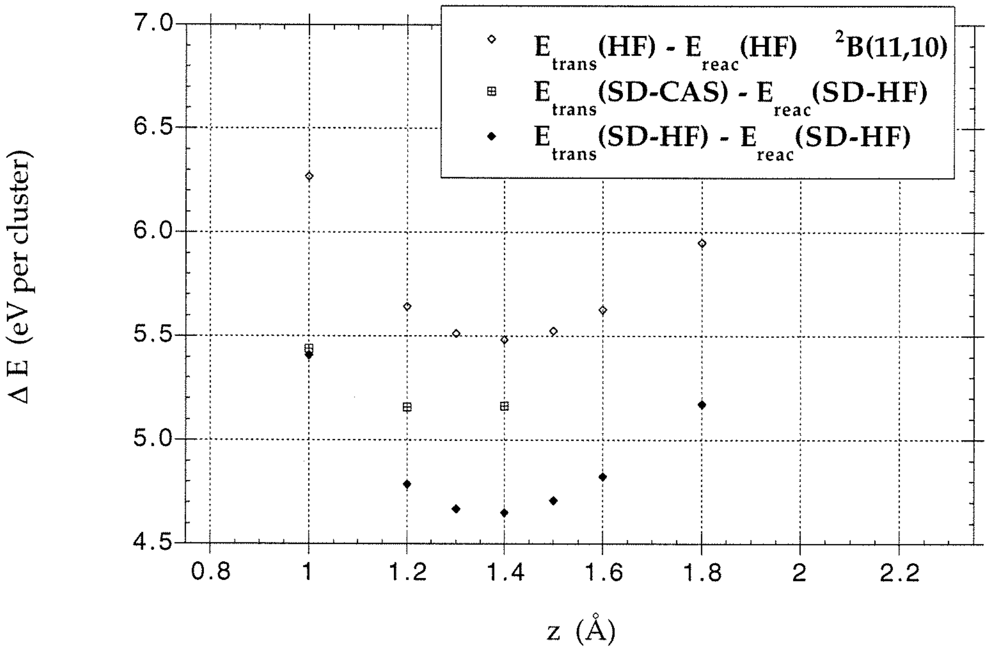

Figure 3.28: Computed potentials of an excited transition state for (1,4) F migration. The HF configuration was $^2B(11,10)$, the GVB-CAS was 5-in-5, and the SDs were 5-in-5. The z axis is defined in fig. 3.3 .

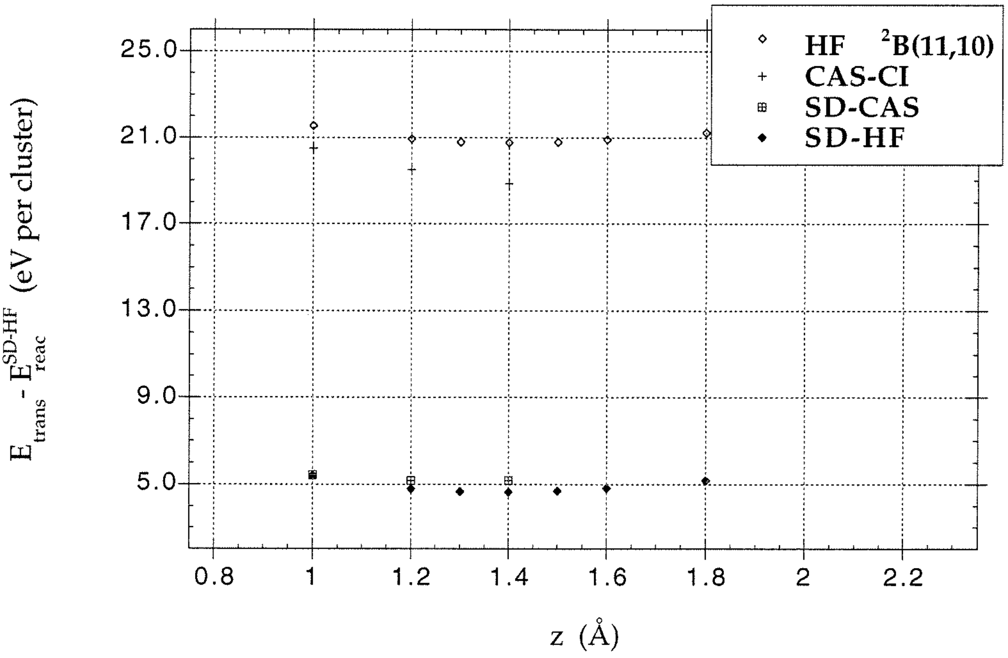

Figure 3.29: Computed potentials of an excited transition state for (1,4) F migration. The HF configuration was $^2B(11,10)$, the GVB-CAS was 5-in-5, and the SDs were 5-in-5. The z axis is defined in fig. 3.3 .

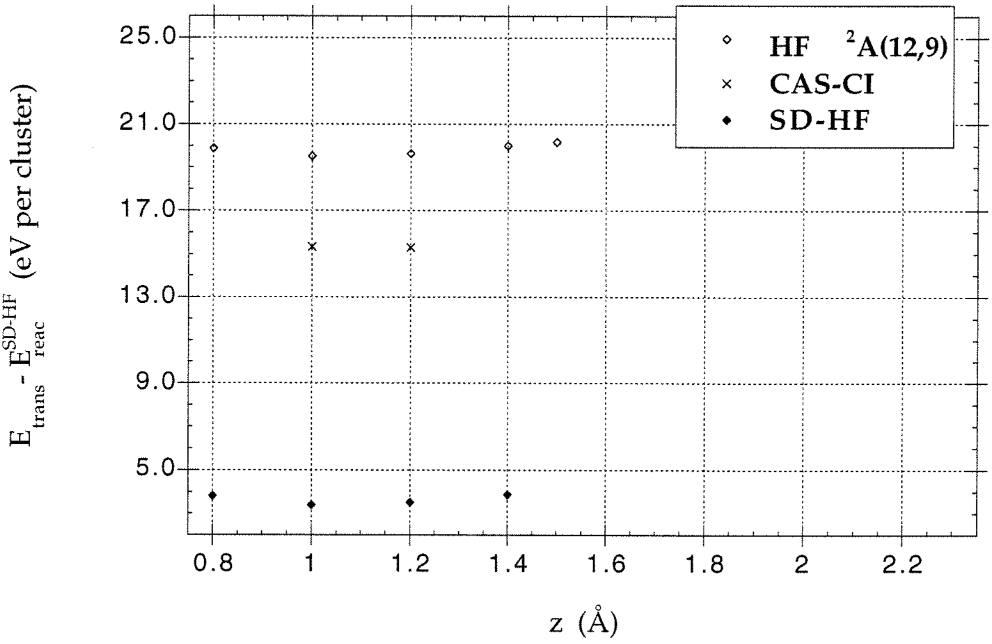

Figure 3.30: Computed potentials of the ground transition state for (1,4) F migration. The HF configuration was ^2A(12,9), the CAS-CI was 13-in-13, and the SD-HF was 7-in-7. The z axis is defined in fig. 3.3 .

Appendix A SIMS profiles of hydrogen and deuterium in diamond

A.1 Introduction

A diamond sample containing layers of various deuterium concentrations was grown by microwave-plasma chemical-vapor deposition. Growing impurities into the diamond allows it to be doped without the lattice damage that accompanies ion-beam doping. Impurity levels were profiled as a function of depth from the diamond surface using Secondary-Ion Mass Spectroscopy (SIMS). Boron doping was necessary to avoid sample charging during SIMS. SIMS confirmed the presence of the layers. The SIMS profile of hydrogen will enable experimentalists to deconvolve surface D from bulk D when performing Nuclear Reaction Analysis (NRA) and surface H from bulk H when performing Elastic-Recoil Spectrometry (ERS).

A.2 Sample synthesis

A B-doped sample was synthesized by microwave-plasma chemical-vapor deposition (MWCVD). The deposition chamber was a Kamo-type reactor, consisting of a quartz tube with diamond-coated quartz substrate holder. The substrate was a natural type IB (100) diamond. First the substrate was deuterium-plasma treated at 925°C and 43 torr for 10 minutes, with a D_2 flow rate of 10 sccm. Secondly the substrate was cooled to 785°C and exposed to a mixture of 10% D_2/89% H_2/1% CH_4 and 2ppm B_2H_6 for 10 minutes. The total flow rate was 100 sccm. Next the mixture was changed to 99% H_2/1%CH_4 and 2ppm B_2H_6 for 2 hours at 100 sccm. Finally, the sample was deuterium-plasma treated at 926°C and 42 torr for 10 minutes, with a flow rate of

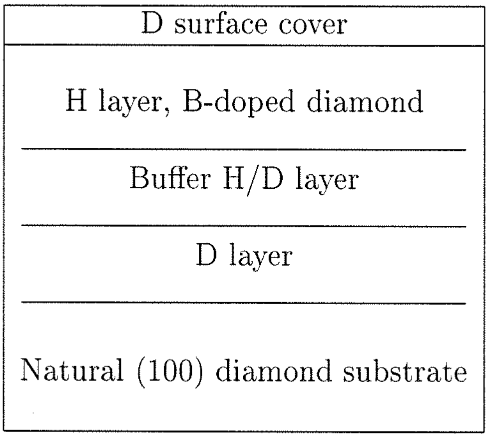

Figure A.1: Impurity layers grown into the diamond sample.

10 sccm. Between each growth or plasma-treatment step, it took several minutes to adjust the pressure and sample temperature, controlled by leak-valve position and microwave power, and re-attain steady state. Growth and treatment times reported omit the adjustment periods. Sample temperature was measured via optical pyrometry, assuming an emissivity of 0.5 due to the polycrystalline diamond coating on the quartz sample holder. The resulting layered structure is shown schematically in fig. A.1.

The "D surface cover" marks the diamond surface so that it can be distinguished from hydrocarbon contamination during SIMS. The B doping increases conductivity, to avoid sample charging during SIMS. The middle D layer is simply a D_2 plasma-treated substrate. The "buffer layer" is a B-doped layer grown with 10% D_2 in the feedgas, to ensure that H does not etch away all the D in the "D layer" during growth.

A.3 Results

Scanning electron microscopy of the sample showed a very smooth surface. There are some small crystallites on the edges and two small regions of polycrystals near the middle, but the rest of the surface looks perfectly smooth on an SEM length scale (>300 nm). SEM indicated the presence of parallel ridges on the surface; however, the ridge height was unresolvable on an SEM length scale. Dektak profilometry showed that the typical peak-to-valley height was about 300 Å.

SIMS profiles are shown in figs. A.2 and A.3. A primary beam of 10 keV Cs^+ was scanned over a 400 μm × 400 μm area. A constant etch rate was assumed in converting the time axis to units of depth. The overall depth of the SIMS trench in the sample was measured by Dektak profilometry. The growth rate of the boron-doped layer was 0.3 μm/hr, assuming it occurred during the 2-hour deposition.

The width of the surface deuterium peak in fig. A.3 is about 300 Å. The majority of the deuterium in this peak is expected to have originated from the surface. One would expect the width of the hydrogen surface peak to be the same as that of deuterium. There is a small surface hydrogen peak in fig. A.2, but it is about one-third narrower than the deuterium peak. Presumably the signal from the background hydrogen in the SIMS chamber is eclipsing the signal from the sample hydrogen. No surface hydrogen peak is evident in fig. A.3, where the slower etch rate decreased the sample H signal to below background hydrogen levels. Therefore, the (background) H signal in fig. A.3 should be taken as an upper bound to the actual hydrogen content in the sample.

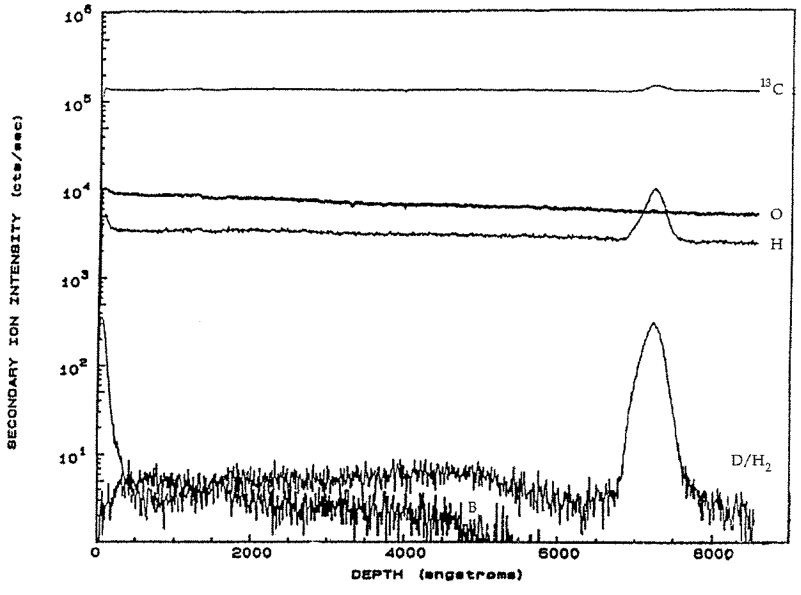

Figure A.2: SIMS profile of subsurface deuterium content.

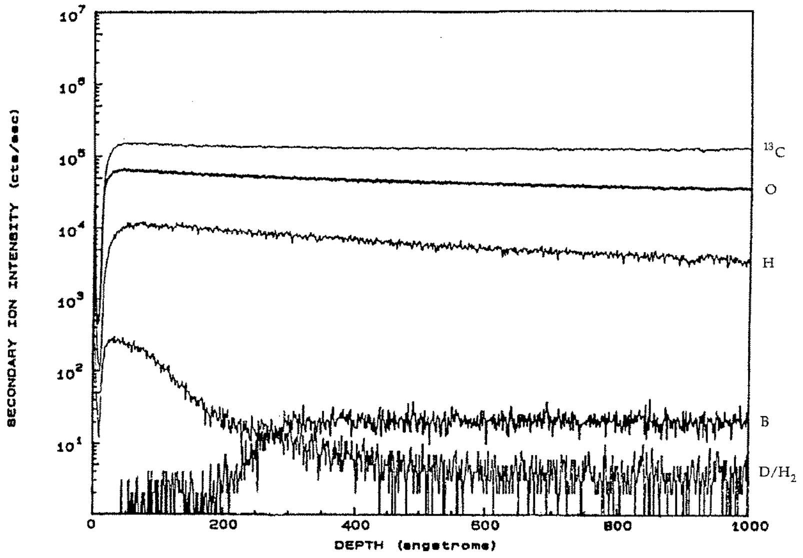

Figure A.3: SIMS profile of near-surface region.

Count rate may be roughly converted to density by

$$\rho_i = \frac{I_i}{I_{C-13}} \frac{RSF_i}{RSF_{C-13}} \times \rho_{C-13}, \tag{A.1}$$

where ρ_i is the impurity atom density, I_i is the secondary ion intensity of the impurity, and RSF is the relative sensitibity factor describing the secondary ionization yield. The RSF depends on the matrix material and incident beam and was not calibrated for the SIMS conditions. In the absence of a calibration for the 10 keV beam, RSF is taken from data for a 14 keV Cs^+ beam incident on a separate diamond [1, p. E-3]. The RSF for ^{13}C is 1.8×10^{23}, for H is 4×10^{23}, and for 0 is 2.3×10^{23}. In fig. A.3, 1.3×10^5 cts/s corresponds to the density of ^{13}C in diamond, which for an isotopic abundance of 1.1% [2, p. 344] [3] is 2×10^{21} particles per cm^3. Therefore, 1.3×10^5 H^- cts/s corresponds to a density of approximately 0.88×10^{21} H/cm^3 taking into account the relative RSF factors. The density of H in the top 500 Å is then $\sim$1.7–3.3×10^{20} H/cm^3.

A bulk density on the order of 10^{20} H/cm^3 is consistent with the bulk hydrogen content found in other experiments. Dollinger *et al.* [4] measured hydrogen content by elastic-recoil detection on polycrystalline diamond grown by MWCVD on a silicon substrate. They found a bulk hydrogen content of of 1.4×10^{20} H/cm^3. Madiba *et al.* [5] used nuclear reaction analysis to measure a bulk density of $8.8 \pm 2.6 \times 10^{19}$ H/cm^3 in a high-pressure synthetic diamond. Although a bulk density of 1.7–3.3×10^{20} H/cm^3 is consistent with hydrogen densities measured in diamond by other techniques, it is only an upper bound to the actual H content in the sample due to the presence of background hydrogen in the SIMS signal.

The depth resolution of ERS profiles is approximately 500 Å in diamond for an 8-μm Al stopper foil and 2.0-MeV incident He$^+$ beam. Integrating the H signal over the top 500 Å and converting cts/s to density as earlier, the H content is 1.3×10^{15} H/cm^2. Therefore, an upper bound to the total subsurface H contribution to ERS profiles is 0.8 H per surface C on the (100) surface.

The density of D at the surface is approximately 6.7×10^{18}/cm^3, assuming the same secondary ionization yield for D as for H. Assuming a linear drop to 3.3×10^{17}/cm^3 at 300 Å and 1.7×10^{17}/cm^3 at 500 Å, the total deuterium content is less than 1.1×10^{13}/cm^2. Therefore, the total contribution of subsurface deuterium to ERS profiles is approximately 7×10^{-3} D per surface C on the (100) surface.

The depth resolution of NRA in diamond is approximately 6750 Å for an 0.7-MeV incident ^{3}He$^+$ beam.[1] Taking density to be constant from 500 Å to 6750 Å, the total contribution of subsurface deuterium to NRA profiles is 0.014 D per surface C.

Figure A.4 gives a better estimate of the sample H signal. The width of the surface H peak is approximately the same as that of the surface D peak, indicating a lower background H level. The spectrum in fig. A.4 was taken with a higher etch rate than, and several hours after, the spectrum of fig. A.3, allowing a lower base pressure in the SIMS chamber and lower background levels in the spectra. Converting the count rate to density as before, the H content in the top 500 Å is 0.30 H per surface C,

---

[1] The NRA depth resolution is determined by the width of the resonance producing the nuclear reaction [6, fig. A11.23, p. 568]. The incident ^{3}He$^+$ energy drops from 0.70 to 0.37 MeV before the nuclear-reaction cross section drops to half its peak value. Taking an average stopping power of 37 eV/(10^{15} atoms/cm^2) [7], the ion travels 6750 Å through the diamond before losing 0.33 MeV. Therefore, in addition to the surface deuterium, the spectra integrate over the top 6750 Å of bulk deuterium.

and the D content is 0.0034 D per surface C. The total deuterium content in the top 6750 Å is 0.0050 D per surface C.

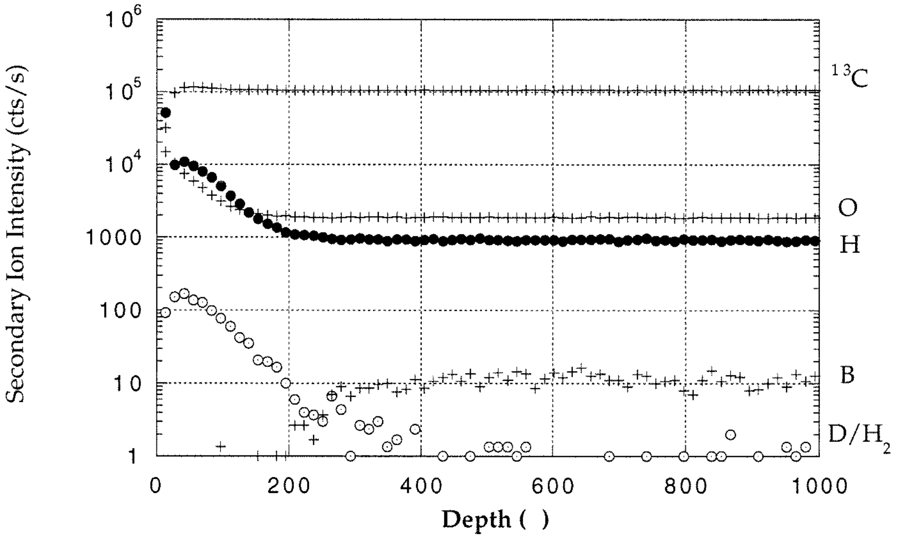

Figure A.4: SIMS profile of near-surface region with lower background hydrogen levels.

In fig. A.5 the boron signal drops to zero unexpectedly soon, about 1000 Å before the H/D buffer layer. The reason for the drop is unknown. It is possible that growth occurred during the 40-minute adjustment period when the D_2 and H_2/D_2 plasmas were hot but had not attained steady state, yielding 1750 Å of growth with no B incorporation. If this is the case, the growth rate in the low-B-density layer was 0.1 μm/hr, and the source of the hydrocarbon was the polycrystalline-diamond-coated sample holder. However, it is unlikely that background hydrocarbons could cause such a high growth rate.

A more plausible explanation for the drop in B density at 6000 Å is the delay time necessary to attain steady-state gas-phase concentrations in the reactor. If the entire region above 7750 Å grew during the 2 hours that the CH_4 was flowing, then the undetectably low B density between 7750 Å and 6000 Å, as well as the slow increase in B concentration between 6000 Å and 3000 Å, may reflect the time it took the reactor gas to attain steady-state concentration of B. A Kamo-type reactor has

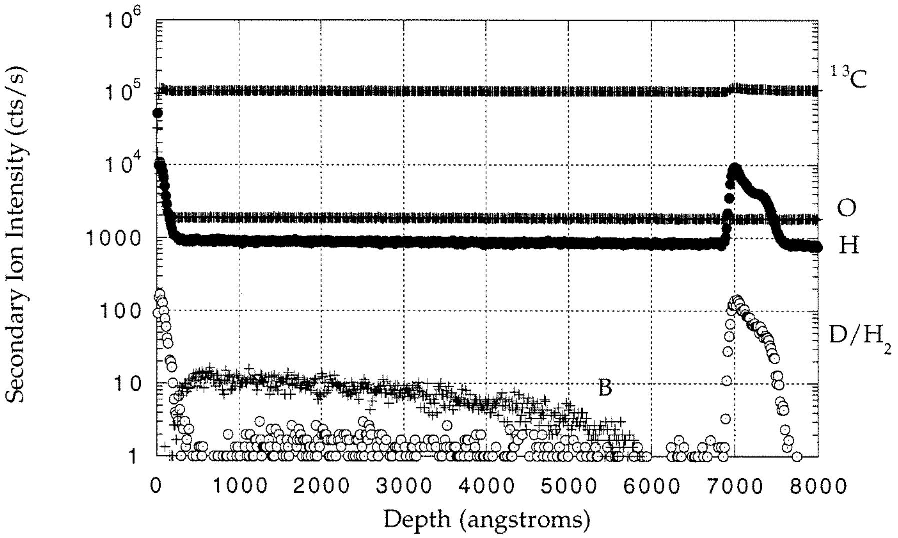

Figure A.5: SIMS profile of film with best background hydrogen levels.

large volume due to a stainless-steel sleeve at the bottom for feedthroughs. The total volume of the reactor was on the order of 55,000 cm^3, and with a flow rate of 100 sccm the order of 50 minutes was required to attain steady-state B concentrations. The average growth rate between 7750 and 3000 Å was then ~0.5μm/hr, and the average growth rate during steady-state B incorporation was ~0.3μm/hr. Locher *et al.* [8] found an approximately linear dependence between the film's boron density and the (steady-state) gas-phase B concentration between 0.2 and 30 ppm. Therefore, the B density likely began to rise at the beginning of growth (presumably 7750 Å), reaching detectable levels at 6000 Å, and attaining steady-state at 3000 Å.

A.4 Conclusions

A diamond sample containing layers of various deuterium concentrations was grown by MWCVD on the C(100) surface. Boron doping avoided the sample charging that usually accompanies SIMS profiling of diamond. SIMS confirmed the presence of the layers. SEM and Dektak profilometry indicated the presence of parallel ridges on the surface averaging about 300 Å in height.

Secondary ion intensities in SIMS profiles were converted to approximate atomic densities using relative sensitivity factors for a 14 keV Cs^+ beam incident on diamond. For use in deconvolving surface hydrogen on the (100) face from bulk hydrogen in ERS spectra, hydrogen density was integrated over the top 500 Å. The total deuterium content in the top 500 Å is approximately 0.003 D per surface C. In initial spectra, the background hydrogen eclipsed the sample's H signal, yielding an upper bound to the hydrogen content in the top 500 Å of 0.8 H per surface C. The final spectrum showed a lower background H signal, and the hydrogen content in the top 500 Å is 0.30 H per surface C. For use in deconvolving surface deuterium on the (100) face from bulk deuterium in NRA spectra, hydrogen densities were integrated over the top 6750 Å. In initial spectra, the total deuterium content is approximately 0.014 D per surface C, and an upper bound for the H content is 7.5 H per surface C. In the spectrum with the lowest background H signal, the total deuterium content in the top 6750 Å is 0.0034 D per surface C, and the total H content is 0.30 H per surface C.

A.5 Acknowledgements

I gratefully acknowledge the Japanese National Institute for Research in Inorganic Materials (NIRIM) for facilitating the project. The work was supported in part by the U.S. National Science Foundation and the Japanese Institute for Science and Technology under the 1995 Summer Institute in Japan for U.S. Graduate Students in Science and Engineering. I gratefully acknowledge Drs. Y. Sato, M. Kamo and M. Nishitani for welcoming me into their lab, I. Sakaguchi for performing SIMS, and T. Ando and S. Koizumi for getting me started on and trusting me with their growth chamber and SEM. I thank all the members of NIRIM's High-Temperature Materials Research Lab and TEM group for their hospitality. Valuable discussions with Dr. Gary R. Huss of Caltech are gratefully acknowledged.

Bibliography

[1] R. G. Wilson, F. A. Stevie and C. W. Magee, *Secondary Ion Mass Spectrometry: A Practical Handbook for Depth Profiling and Bulk Impurity Analysis*. Wiley, New York (1989).

[2] W. K. Chu, J. W. Mayer and M.-A. Nicolet, *Backscattering Spectrometry*. Wiley, New York (1977).

[3] G. Faure, *Principles of Isotope Geology*. John Wiley & Sons, New York (1977). See p. 324 for the isotopic abundance of ^{2}H. See pp. 379 and 387 for the isotopic abundance of ^{13}C in natural colorless diamond.

[4] G. Dollinger, A. Bergmaier, C. M. Frey, M. Roesler and H. Verhoeven, "Impurities of light elements in CVD diamond." Diam. Rel. Mat. **4**, 591–595 (1995).

[5] C. C. P. Madiba, J. P. F. Sellschop, J. A. Van Wyk and H. J. Annegarn, "Light volatiles in synthetic diamond analysed by ion probes." Nucl. Instr. and Meth. B **35**, 442–445 (1988).

[6] L. Foster, G. Vizkelethy, M. Lee, J. R. Tesmer and M. Nastasi, "Particle-particle nuclear reaction cross sections." In *Handbook of Modern Ion Beam Materials Analysis*, edited by J. R. Tesmer and M. Nastasi, Materials Research Society, Pittsburgh, PA (1995), pp. 549–568.

[7] J. F. Zeigler, "Helium stopping powers and ranges in all elements." In *The Stopping Powers and Ranges of Ions in Matter*, Pergamon Press, New York (1977), volume 4. See p. 30 for conversion between ^{3}He and ^{4}He stopping powers.

[8] R. Locher, J. Wagner, F. Fuchs, M. Maier, P. Gonon and P. Koidl, "Optical and electrical characterization of boron-doped diamond films." Diam. and Rel. Mat. **4**, 678–683 (1995).

Appendix B Design of pelletron endstation for Elastic-Recoil Spectrometry

B.1 Motivation

Although kinetics models are powerful tools to understand diamond surface reactions and growth, many of the parameters used in them have yet to be measured experimentally. Here I report the design of an ultrahigh vacuum system to study the kinetics of H reactions with diamond, important processes in diamond chemical-vapor deposition (CVD), and to measure absolute hydrogen coverage, an important parameter in diamond surface models. The system will measure the amount of hydrogen on the C(100) surface by elastic-recoil spectrometry (ERS), an ion-beam scattering method to detect atoms lighter than the incident ion [1, 2, 3]. Relative coverages have previously been measured through electron or photon spectroscopy, but here *absolute* coverage will be measured, to within about 5% of a monolayer. Measuring hydrogen coverage in UHV as a function of temperature tells the absolute saturation coverage of the (100) surface produced by plasma pre-treatment. The system will be designed to heat the sample in order to study surface reactions at diamond growth temperatures (~1000°C). Sample heating will also be necessary to desorb physisorbed contaminants and to prevent sample charging during electron diffraction.

The vacuum system will include a reflection high-energy electron diffraction (RHEED) system to allow hydrogen coverage to be correlated with surface reconstruction. Chin *et al.* [4] recently correlated (111) surface reconstruction with hydrogen coverage via sum-frequency generation and found that adsorption of 0.05 H per surface C was sufficient to revert the (2×1) surface to a (1×1) structure. The experiment reported in chapter 2 investigated deuterium coverage of the C(100) surface via nuclear reaction analysis (NRA). The surface was initially a (2×1) structure, with ~1 D per surface C. However, after exposure to filament-cracked hydrogen at an unusually high filament temperature of 2025°C, coverages up to 1.3 D per surface C were measured. This indicated the possibility of a (3×1) structure, a reconstruction which has been investigated theoretically [5] but not yet observed experimentally. RHEED observations in the ERS endstation will allow further investigations of the (100) surface structure and its evolution upon exposure to gas-phase H. Due to diamond's low conductivity, the sample will be heated to avoid charging during RHEED.

In other diamond experiments, cycling the sample through a series of hydrogen exposures and thermal desorptions degraded the surface LEED pattern. Adsorption/desorption cycling also caused a second peak to arise at lower temperatures in thermal desorption spectra, indicating the possibility of dihydride sites on the surface. RHEED observations coupled with ERS measurements will allow degradation to be quantified, and coverages greater than 1.0 H per surface C would strengthen the argument for the association of degradation with surface dihydrides.

The system is also designed to study reaction kinetics by measuring the hydrogen coverage of diamond upon exposure to atomic H at various gas and surface temperatures. As shown in chapter 2, absolute coverage data allows one to calculate the ratio of the abstraction rate constant to the recombination rate constant, both averaged over all surface sites present. These two reactions control the fraction of surface sites available for growth during diamond CVD. Measuring rate data as a function of temperature extends other experiments [4, 6, 7], which investigated a single filament temperature and low surface temperature, by allowing activation barriers to be obtained.

Measuring rate data as a function of temperature also gains information about the dynamics of reactions on diamond surfaces. For example, at temperatures low enough for migration and desorption to be inactive, the reaction

$$\mathrm{H^{gas}} + \mathrm{HC{-}C\cdot^{surf}} \xrightarrow{k_{Ah}} \mathrm{H_2^{gas}} + \mathrm{\cdot C{-}C\cdot^{surf}} \tag{B.1}$$

is expected to be Eley-Rideal, where the gas-phase reactant provides the energy to surmount the activation barrier and rate depends solely on gas temperature. (Here HC$-$C$\cdot^{\text{surf}}$ denotes a half-hydrogenated dimer on the C(100) (2×1) surface, and $\cdot$C$-$C$\cdot^{\text{surf}}$ denotes a pi-bonded dimer.) However, at higher temperatures, surface-surface reactions participate in the conversion of atomic to molecular hydrogen, and conversion rates are expected to develop a dependence on surface temperature. Above ~600°C desorption becomes active, opening a pathway for reaction B.1 to occur not only through direct abstraction but also through a sequence of recombination and desorption steps,

$$\mathrm{H^{gas} + HC{-}C\cdot^{surf}} \xrightarrow{k_{Rh}} \mathrm{HC{-}CH^{surf}} \tag{B.2}$$

$$\mathrm{HC{-}CH^{surf}} \xrightarrow{k_D} \mathrm{H_2^{gas} + \cdot C{-}C\cdot^{surf}}, \tag{B.3}$$

where k_{Rh} is the recombination rate constant and k_D is the desorption rate constant. Reactions B.2 and B.3 represent a Langmuir-Hinshelwood mechanism, where the gas-phase reactant comes into equilibrium with the surface before reacting (desorbing) and therefore the rate of H_2 formation depends on surface temperature.

The chamber is designed to expose the diamond to atomic hydrogen several times, each at a different surface or filament temperature, and measure the resulting coverage. Desired surface temperatures are 200°C, 500°C, 700°C, and 1000°C, and filament temperatures are 1560°C, 1800°C, and 2100°C. The sample will be cooled before each ERS measurement to avoid light noise in the RBS detector and to keep the hydrogen signal well-separated from the thermal noise peak of the ERS detector.

B.2 Experiment in old endstation

Procedure

The sample was natural type IIA diamond, cut and mechanically polished to a surface plane of (100) ± 3° by Harris Diamond Corporation. The as-received samples were ultrasonic-rinsed in ethanol before attaching to the sample holder. The samples were glued to the holder with household paraffin, and no plasma-treatment was performed.

The ERS set-up is shown in fig. B.1. Hydrogen coverage was measured by collecting H^+ ions forward-recoiled from an incident $^4He^+$ beam. The energy of the incident helium beam was 1.9 MeV, and the current was 5 nA. Forward scattered helium ions were filtered by a 8-μm aluminum foil placed in front of the ERS detector. Spectral area was converted to absolute hydrogen coverage by comparison to a polystyrene standard of 1000 Å $(C_8H_8)_n$ on a Si substrate. RBS and ERS spectra were collected simultaneously, and the ERS spectral area was normalized by the height of the RBS carbon edge, thus eliminating the need to measure beam current incident at the sample. Channel number in the RBS spectrum was converted to energy by comparison to a sample containing three marker layers (Au, Rh, and Co) on top of a Si substrate.

Results

Fig. B.2 shows a spectrum of elastic recoils from an unheated diamond sample in the old endstation. About eight monolayers of hydrogen are present, presumably due to hydrocarbon contamination physisorbed to the surface. The sample must be heated in order to desorb the contamination.

The hydrogen spectrum contains an asymmetric surface peak with a low-energy tail, similar to the ERS spectra obtained by Ingram *et al.* [8] on microwave-plasma CVD diamond. Ingram *et al.* estimated the sum of surface and subsurface H to be 1.5%, or about 7.5 H per surface C. The bulk H content was estimated to be 0.3%. Assuming the subsurface H fraction in the top 500 Å was the same as that of the bulk, the total contribution from subsurface hydrogen in the top 500 Å is 1.5 H per

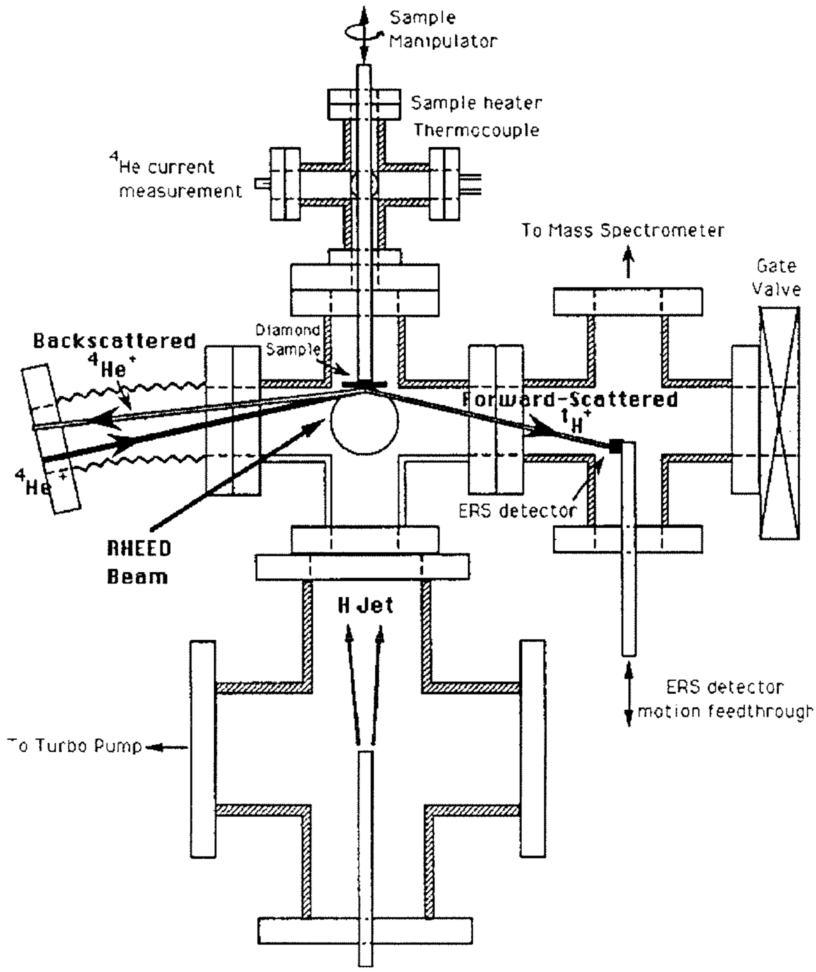

Figure B.1: Schematic of old ERS endstation.

surface C. Therefore, there are approximately 6 H per surface C on the surface of the Ingram sample. Allowing 1–2 monolayers of surface-chemisorbed hydrogen, the remaining 4–5 H per surface C were presumably due to hydrocarbon contamination. The Ingram sample was also unheated.

The ERS results are also consistent with those obtained by Yagi *et al.* [9] on MWCVD homoepitaxial C(100). Yagi *et al.* found 3–4 H per surface C on their samples. The samples were unheated, and therefore presumably contained 2–3 monolayers of hydrocarbon contamination, in addition to 1 monolayer of chemisorbed hydrogen. The working pressure was 8×10^{-9} torr. Yagi *et al.* argue that surface hydrocarbon contamination can be neglected since the area of their H peak did not vary signifi-

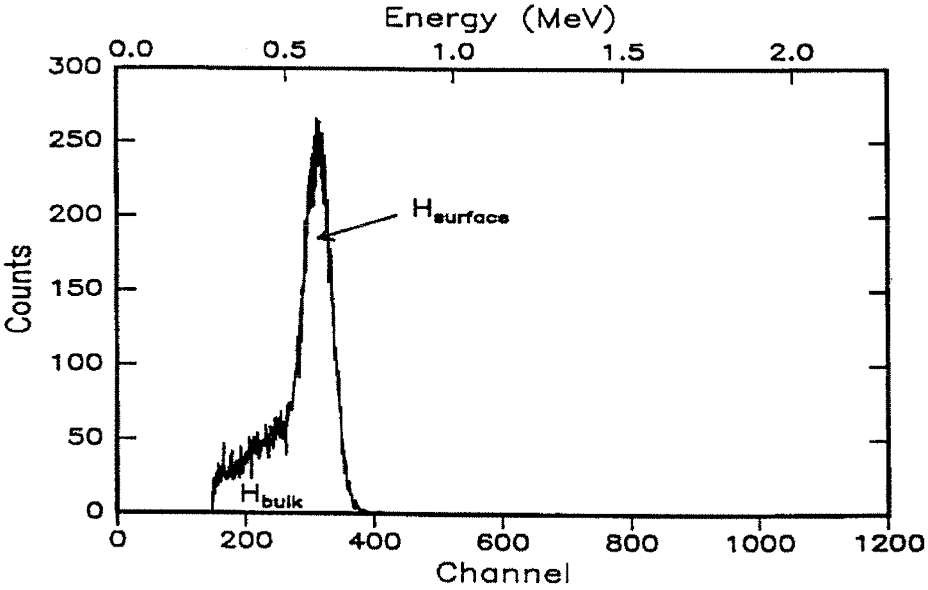

Figure B.2: ERS spectrum of unheated diamond sample obtained in old endstation.

cantly with beam dose between 2×10^{14} and 12×10^{14} ions/cm^2. However, constant coverage may simply indicate that steady-state was attained, i.e., pumping rate was equal to the hydrocarbon condensation rate.

The present results are consistent with those of Ingram *et al.* [8] and Yagi *et al.* [9] and indicate that several monolayers of hydrocarbons are physisorbed on the diamond surface. Sample heating is necessary to desorb the contamination and to measure the true coverage of chemisorbed hydrogen on diamond by ERS.

Fig. B.3 shows the RBS spectrum of the diamond substrate. A carbon edge is clearly resolved at 0.88 MeV. During RBS the beam occasionally oscillated off the sample, and a small signal from the stainless-steel sample holder is evident at 1.69 MeV. However, the ratio of the height of the holder edge to that of the carbon edge indicates that the holder received only ~0.0005 the beam dose of the sample.[1] Assuming the holder contained 10% (atomic) hydrogen, the holder's contribution

---

[1] The small dose received by the holder is consistent with the pattern of radiation damage evident in the sample. Before RBS the sample was clear and colorless, and upon RBS a grey elliptical region appeared in approximately the same location as the beam spot. The grey region was darkest near its center and was located in the center of the sample. No grey was evident on the sample edges, indicating little beam oscillation off the sample.

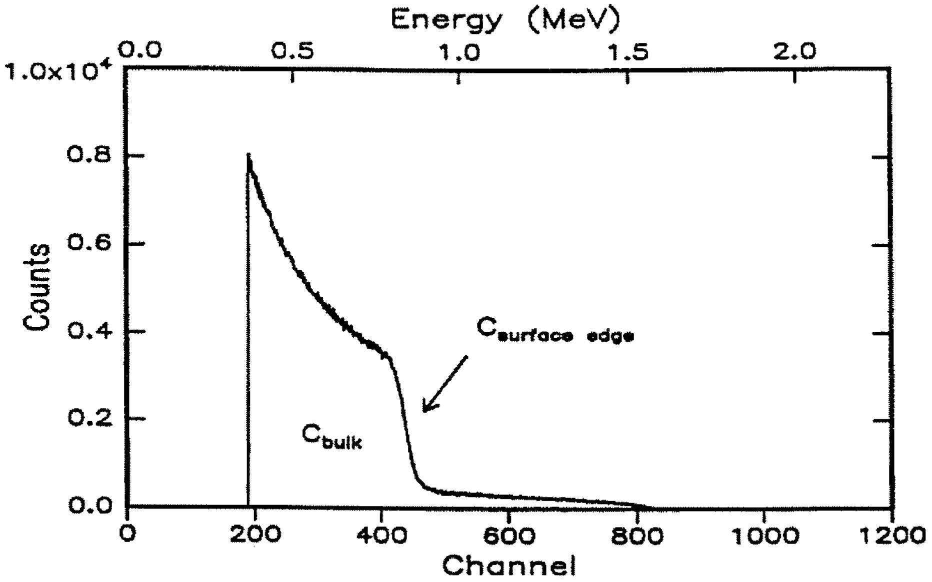

Figure B.3: RBS spectrum of unheated diamond sample obtained in old endstation.

to the spectral area of the surface hydrogen peak is only ~0.002 of the sample's hydrogen contribution. Therefore, the stainless steel's hydrogen was neglected when deconvolving the sample's surface H peak.

Subsurface hydrogen contribution

Low depth resolution is a problem inherent to elastic-recoil spectrometry. Straggling in the aluminum stopper foil reduces the depth resolution to about 500 Å. Therefore the top 500 Å of bulk hydrogen must be subtracted from the spectra to obtain the amount of surface hydrogen. Sellschop *et al.* [10] have measured hydrogen in natural diamond crystals via nuclear reaction analysis (NRA). Although NRA also suffers from poor depth resolution, their results imply an upper bound of about 8.1 monolayers of bulk hydrogen in the top 500 Å, where one monolayer is one H per surface C on the (100) plane. Subsequent experiments on diamond grown by chemical-vapor deposition (CVD) obtained a more exact estimate of subsurface hydrogen content. In the case of homoepitaxial CVD diamond, the experiment of Appendix A estimated the total hydrogen content to be 0.30 H per surface C in the top 500 Å. In initial spectra, the background hydrogen eclipsed the sample hydrogen signal, giving an upper bound of 0.8 H per surface C in the top 500 Å of the sample. In the case of polycrystalline CVD diamond, Dollinger *et al.* [11] detected less than 10^{-3} hydrogen content below the top 10-20 Å. Their hydrogen content was calibrated by comparison to an ion-implanted standard, and the depth resolution was 10 Å. Therefore, I approximate the hydrogen content in the first layers below the surface to be the same as that in the bulk, and I assume that the ERS sample has 10^{-3} bulk hydrogen content. The total subsurface hydrogen content in the top 500 Å of the ERS sample is then approximately 0.6 monolayers.

Even with 0.6 monolayers of subsurface hydrogen and 1 monolayer of surface hydrogen, there were still 6.4 monolayers of hydrogen from physisorbed contamination. The sample must be heated to desorb the contamination.

B.3 Design of new endstation

Due to radiative losses, the old heater was unable to attain temperatures greater than 250°C. Although a higher-temperature heater was available, the old endstation (fig. B.1) was too small to contain the high-temperature heater and holder within its 3.3-cm central cross.[2] Therefore, I custom-designed an entirely new endstation, including a 20.3 cm vacuum chamber and sample holder, along with RHEED and ERS/RBS geometries. The new endstation (fig. B.4) has a simplified geometry, allowing easier bake-out and potentially better vacuum. The new system also locates the ERS detector closer to the sample, yielding shorter data collection times. Previous collection times were typically 30 minutes per coverage measurement. In addition, the atomic hydrogen/ECR port has been moved closer to the sample. The new vacuum chamber hardware is shown in fig. B.5.

The new chamber was designed to fit into the same space as the old endstation. The distance between the new chamber's beam and ERS-detector ports is the same as the distance between the old endstation's beam port and gate valve, plus 1".

---

[2] Moreover, the old heater occupied so much of the volume of the central cross that it caused significant outgassing of the cross walls during heating.

The extra inch allows enough room between the vacuum chamber wall and the ERS detector flange for installing bolts into the flange, while keeping the chamber diameter large enough to support all 3" ports.[3] The similar size of the new chamber to the old endstation not only conserves space but also preserves the alignment of the old endstation with respect to the helium beam during new-chamber installation.[4]

The new design incorporates a high-temperature (1000°C) sample heater and holder. The holder consists completely of molybdenum, to minimize vapor pressure at high temperature. The resistive heater is a thin plate of CVD graphite coated with pyrolytic BN, approx. 1.9 cm × 4.3 cm × 0.3 cm. (The length of 4.3 cm includes space for the electrical leads.) The heater itself consumes about 10 amps at 30 volts, and the hot zone is about 1.7 cm in diameter, ample for the 15 mm × 5 mm sample.

B.4 Conclusions

Hydrogen coverage of the diamond C(100) surface has been measured by elastic-recoil spectrometry. Results show several monolayers of surface contamination, consistent with the measurements of Ingram *et al.* [8] and Yagi *et al.* [9]. Since ERS is a nuclear-sensitive technique, it cannot distinguish between physisorbed contamination and chemisorbed hydrogen. Sample heating is necessary to desorb the contamination and to allow the true coverage of chemisorbed hydrogen on diamond to be measured by ERS.

To decrease contamination, the pelletron endstation has been custom-redesigned to attain better vacuum and higher-temperature sample heating. In addition to des-

---

[3] Space is further conserved by building the support structure for the new endstation upon the cart which housed the old one. The new chamber will be held by clamps at the four 90° ports shown in fig. B.4a, and the clamps will be bolted to a unistrut cage built upon the cart.

[4] The alignment will be preserved as follows. First the cross behind the gate valve of the old endstation (the load-lock cross) will be moved back by 1", to make room for the new chamber, by inserting a one-inch through flange between the gate valve and load-lock cross. The load-lock cross will then be fixed to the unistrut cage before removing the part of the old endstation ahead of the gate valve. Finally, the new endstation will be aligned by bolting to the fixed load-lock cross. (A reducing flange was custom-designed to mate the load-lock cross to the detector port of the new endstation while ensuring proper vertical alignment of the new endstation.)

orbing surface contamination, heating is necessary to avoid sample charging during RHEED and to study diamond surfaces at CVD growth temperatures. The new design allows sample heating to 1000°C as well as RBS, ERS, RHEED, and hydrogen or deuterium exposure studies.

The new endstation will allow the study of abstraction and recombination, key radical-surface reactions in diamond chemical-vapor deposition, and thermal desorption, key reactions in diamond surface science. Studying these reactions as a function of separately-controlled gas and surface temperatures will permit the identification of the regime in which the reactions are Eley-Rideal and the regime in which they are Langmuir-Hinshelwood.

The new endstation will also allow *absolute* hydrogen coverage to be measured on the reconstructed C(100) (2×1) surface. Coverage measurements and RHEED observations will permit the evolution of the surface structure to be investigated as a function of exposure to gas-phase H. Upon repeating the high-temperature dosing conditions which produced coverages of 1.3 D/surface C in chapter 2, RHEED observations can determine whether the (3×1) surface appears. The (3×1) reconstruction has been investigated theoretically [5], but its electron diffraction pattern has not yet observed experimentally. Furthermore, correlating absolute coverage with RHEED patterns will allow surface degradation to be quantified. Coverages greater than 1.0 H per surface C would strengthen the argument for the association of degradation with surface dihydrides, and the relationship between degradation and roughness can be determined by *ex-situ* atomic-force microscopy.

B.5 Acknowledgements

This work was funded in part by ONR and NSF. I would like to acknowledge Profs. Harry A. Atwater and David G. Goodwin, for reviewing preliminary designs, and Prof. Marc A. Nicolet, for his hospitality in the pelletron laboratory. I also thank Dr. Ramana Murty for training me to operate the old endstation, and I thank Dr.

Hyun Lee and Mrs. Michael Easterbrook, Jeffrey Atkinson, Robert Gorris and Roy Andrews for technical advice and design assistance.

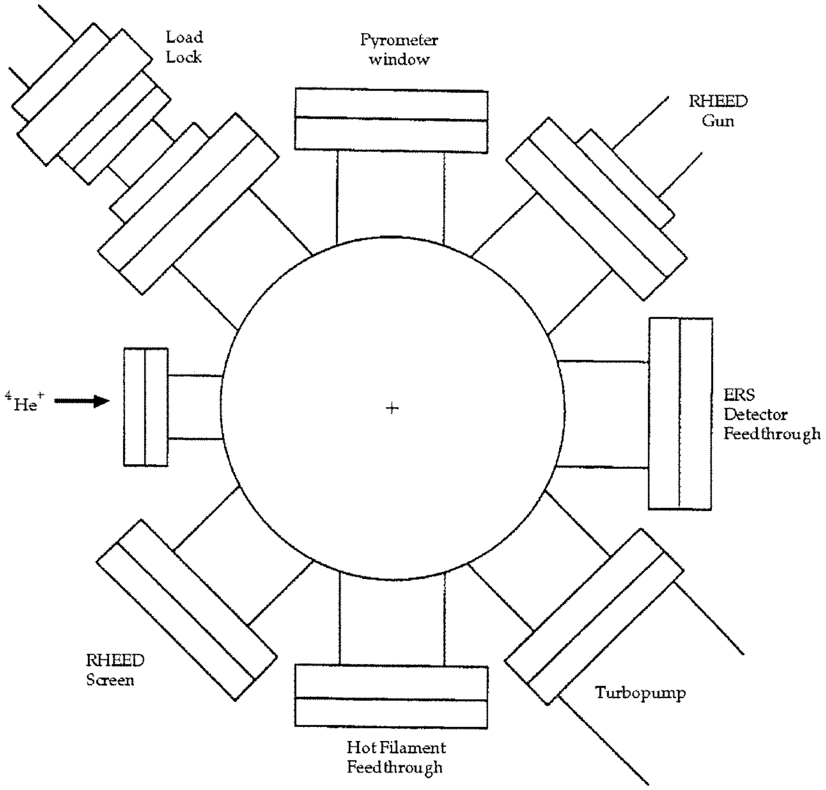

(a) Top view.

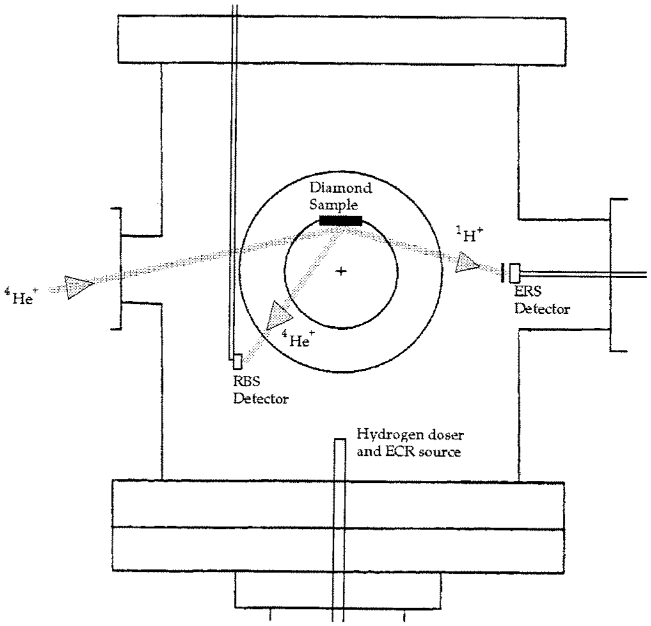

(b) Side view, with 45° ports omitted for clarity.

Figure B.4: Schematic of new endstation.

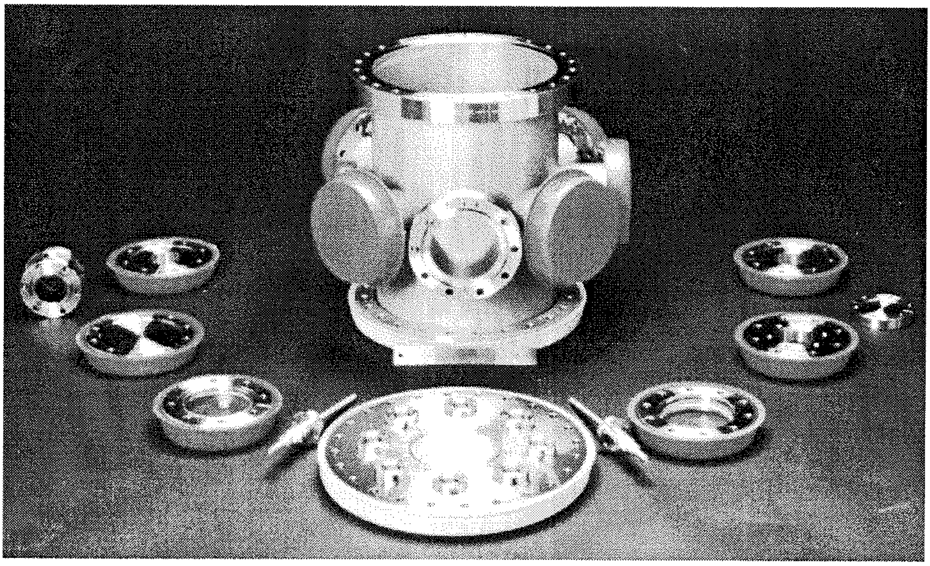

Figure B.5: Custom 8" vacuum chamber and multiport flange for the new ERS endstation, surrounded by standard hardware. The ruler at the base of the flange is six inches long.

Bibliography

[1] J. E. E. Baglin, A. J. Kellock, M. A. Crockett and A. H. Shih, "Absolute cross section for hydrogen forward scattering." Nucl. Instr. and Meth. B **64**, 469–474 (1992).

[2] F. Besenbacher, I. Stensgaard and P. Vase, "Absolute cross section for recoil detection of deuterium." Nucl. Instr. and Meth. B **15**, 459 (1986).

[3] A. Turos and O. Meyer, "Depth profiling of hydrogen by detection of recoiled protons." Nucl. Instr. and Meth. B **232**, 92 (1984).

[4] R. P. Chin, J. Y. Huang, Y. R. Shen, T. J. Chuang and H. Seki, "Interaction of atomic hydrogen with the diamond C(111) surface studied by infrared-visible sum-frequency-generation spectroscopy." Phys. Rev. B **52**, 5985–5995 (1995).

[5] Y. L. Yang and M. P. D'Evelyn, "Theoretical studies of clean and hydrogenated diamond (100) by molecular mechanics." J. Vac. Sci. Technol. A **10**, 978–984 (1992).

[6] B. D. Thoms, J. N. Russell, Jr., P. E. Pehrsson and J. E. Butler, "Adsorption and abstraction of hydrogen on polycrystalline diamond." J. Chem. Phys. **100**, 8425–8431 (1994).

[7] D. D. Koleske, S. M. Gates, B. D. Thoms, J. N. Russell, Jr. and J. E. Butler, "Hydrogen on polycrystalline diamond films—studies of isothermal desorption and atomic deuterium abstraction." J. Chem. Phys. **102**, 992–1002 (1995).

[8] D. C. Ingram, J. C. Keay, C. Tang, M. L. Lake and J. M. Ting, "Trapping of hydrogen in diamond." Diam. Rel. Mat. **2**, 1414–1419 (1993).

[9] H. Yagi, K. Tanida, K. Nishimura, A. Hatta, T. Ito and A. Hiraki, "Elastic recoil detection analysis for hydrogen near the surface of chemical-vapor-deposited diamond." Jpn. J. Appl. Phys. **34**, L577–L579 (1995).

[10] J. P. F. Sellschop, S. H. Connell, C. C. P. Madiba, E. Sideras-Haddad, M. Stemmet, K. Bharuth-Ram, H. Appel, W. Kundig, B. Patterson and E. Holzschuh, "Hydrogen in and on natural and synthetic diamond." Nucl. Instr. Meth. B **68**, 133–140 (1992).

[11] G. Dollinger, A. Bergmaier, C. M. Frey, M. Roesler and H. Verhoeven, "Impurities of light elements in CVD diamond." Diam. Rel. Mat. **4**, 591–595 (1995).

Appendix C Kinetic Monte-Carlo algorithm to simulate deuterium reaction with diamond (100) (2×1)

C.1 Reaction mechanism

The interaction of gas-phase deuterium with the diamond surface is modeled via an abridged version of the reaction mechanism of Dawnkaski *et al.* [1], table C.1. The Dawnkaski mechanism includes only reconstructed terrace sites, and our abridgement excludes the surface methyls. The resulting deuterium coverage, $\theta_D(t, T_{gas}, T_{surf})$, may be calculated via a time-dependent Monte Carlo algorithm. I present an algorithm to rigorously weight the competition between gas-surface reactions and surface migrations within the same iteration step. Addressing migrations in the same iteration as gas-surface reactions cuts in half the number of required iterations.

C.2 Kinetic Monte-Carlo algorithm

The model calculates the deuterium coverage as a function of time. At each time step, a grid of surface sites is cycled through in random order. Each surface site has several possible reactions that can occur. For example, an isolated radical site can undergo gas-surface reactions R1 and -A1 or if neighboring sites are deuterated the deuterium may migrate via reactions M01t, M01T, M11t, or M11T. Each of these 6 reactions is assigned a probability $p_{(dc*)j} = \frac{\delta t}{\tau_{(dc*)j}}$, where δt is the computational timestep and

Reaction	Label
H atom recombination	
With an isolated C radical	R1
With one C atom in a π-bond	R2
H atom desorption	
To form an isolated radical	D1
To form a π-bond	D2
H atom abstraction	
To form an isolated radical	A1
To form a π-bond	A2
H_2 deposition of a H atom	
At an isolated radical	-A1
At one C atom in a π-bond	-A2
H_2 desorption	D0
H_2 adsorption	-D0
H atom hop to a radical site	
Across dimer	M01d
Across trough	M01t
Parallel to trough	M01T
H atom hop to form a π-bond	
Across trough	M11t
Parallel to trough	M11T
H atom hop to break a π-bond	
Across trough	M10t
Parallel to trough	M10T
CH_3 hop to a radical site	
Across dimer	M01dm
Across trough	M01tm
Parallel to trough	M01Tm

Table C.1: Reaction mechanism of Dawnkaski *et al.* [1] for interaction of hydrogen with diamond (100) (2×1). Nomenclature and labels have been changed to correspond to the present text.

$\tau_{(dc*)j}$ is the characteristic time for reaction j on site $(dc*)$. The timestep is chosen so that $\sum_j p_j \leq 1$. The p_j along with the probability of no reaction, $1 - \sum_j p_j$, define bins between 0 and 1. A random number is then generated and the bin into which it falls determines which event occurs. The site, and its neighbors in the case of migration, are updated, and the entire process repeated for the next site.

This algorithm affords the advantage of allowing *all* possible reactions for a given site to compete with each other. The list of sites is cycled through once for each δt, and the migration reactions are treated in the same manner as the gas-surface reactions. This contrasts with the Dawnkaski algorithm, which separates migration events from gas-surface events and cycles through the list of surface sites twice for each δt.

For a given site, the set of all possible reactions is determined not only by the site type but also by the neighboring site types. When a site at time t undergoes a reaction, both it and its neighbors are immediately updated to their states at time $t+\delta t$. As the algorithm continues cycling through the list of sites, it eventually reaches one of the neighboring sites, whose clock was already updated to time $t + \delta t$. It then determines the set of all possible reactions for that site by examining *its* neighbors, some of whose clocks are at time t and some at time $t + \delta t$. However, in the physical system sites interact with their present neighbors, not future neighbors, and all sites are updated simultaneously, not serially. One way to resolve this inconsistency is to choose a computational timestep, $\delta t' \simeq \delta t/N$, so small that only one site of the entire grid is likely to undergo a reaction. However, a faster solution is to pick a surface site at random and allow it to undergo a reaction with large probability, weighted by the reactivity of the site, and then advance all site clocks by $\delta t/N$ and iterate. However under this scenario some sites will never be picked or allowed to react. To ensure that all sites are picked, the list of surface sites is randomized and all sites are cycled through in random order.

To weight the probability that a site reacts by its reactivity, δt is chosen as follows. The relative probability for reaction j to occur on site J is $p_{Jj} = \frac{\delta t}{\tau_{Jj}}$, where τ_{Jj} is the characteristic time for reaction j on site J. This probability is normalized by choosing δt so that the probability for no reaction, $p_{J0} \equiv 1 - \sum_j p_{Jj}$, is positive. We arbitrarily choose $\min_J p_{J0}$ to be $\frac{\delta t}{\max_{Jj} \tau_{Jj}}$. Then

$$1 - \sum_j \frac{\delta t}{\tau_{Jj}} \geq \frac{\delta t}{\max_{Jj} \tau_{Jj}}, \tag{C.1}$$

or

$$\delta t \leq \frac{1}{\sum_j \frac{1}{\tau_{Jj}} + \frac{1}{\max_{Jj} \tau_{Jj}}}. \tag{C.2}$$

To ensure that δt simultaneously normalizes reaction probabilities for all site types,

$$\delta t \leq \frac{1}{\max_J \sum_j \frac{1}{\tau_{Jj}} + \frac{1}{\max_{Jj} \tau_{Jj}}}. \tag{C.3}$$

Thus the normalization, or timestep δt, is determined by the site with the highest reactivity. Using the same timestep for all site types ensures that sites with lower reactivity have proportionately lower probablilities to react.

Since every site type has some probability to undergo no reaction, the algorithm may skip every $s_J = gint(1/p_{J0})$ site of type J and automatically update it as having undergone no reaction. In this case the reaction probabilities for the *un*skipped sites must be divided/renormalized by $1 - 1/s_J$ to account for the fact that they must react.

Bibliography

[1] E. J. Dawnkaski, D. Srivastava and B. J. Garrison, "Time dependent Monte Carlo simulations of H reactions on the diamond {001}(2×1) surface under chemical vapor deposition conditions." J. Chem. Phys. **102**, 9401–9411 (1995).

Appendix D Off-axis potential for hydrogen abstraction from constrained isobutane

D.1 Introduction

Hydrogen abstraction from the diamond surface is a key reaction in chemical-vapor deposition. The abstraction process is sensitive to angle of approach at terrace sites [1, 2], and this sensitivity changes reaction probabilities at steps and overhangs. Analogous gas-phase models do not include the geometric constraint of the surrounding diamond surface and of the surface terminators, such as H, Cl and F. Here sensitivity to angle of approach is demonstrated by calculating the GVB-CAS energy at several off-axis geometries near the transition state. The diamond (111) surface is modelled by constrained isobutane. The transition-state geometry is that of Page and Brenner [1]. To approximate the constraint of the surrounding diamond surface, the isobutane atoms are fixed at their transition-state positions while the abstracting hydrogen is placed at several off-axis positions approaching the transition state. The GVB-CAS energy is calculated for hydrogen displacements up to 0.7 Å along the central axis and ±0.7 Å perpendicular to the axis.

D.2 Off-Axis GVB-CAS potential

The GVB-CAS potential is depicted in fig. D.1, and the energies at the 59 calculated geometries are listed in table D.1. The central z axis lies along the line joining the central carbon to the abstracted H. The origin is at the center of mass, 0.209 Å directly below the central carbon. The surrounding three carbons have C_{3v} symmetry; the yz plane is chosen to contain one of these carbons. The (x,y,z) coordinates given are those of the abstracting hydrogen. All other atoms are located in the transition-state geometry given by Page and Brenner [1].

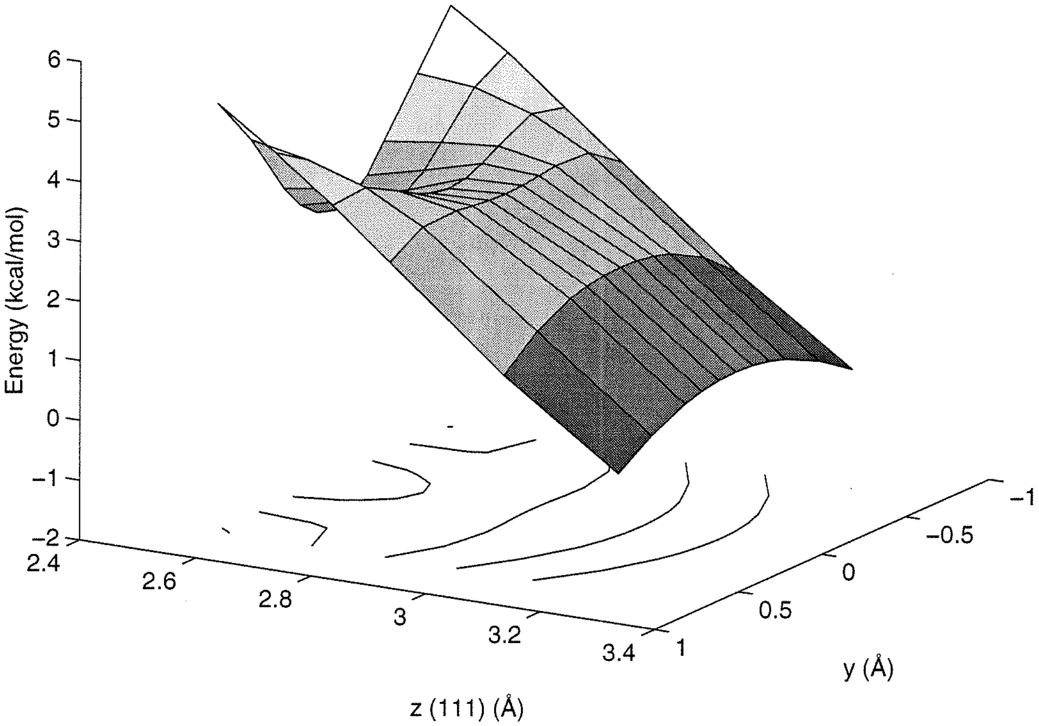

Figure D.1: GVB-CAS potential for H abstraction from constrained isobutane. The CH bond being broken lies along the z-axis at y=0. Energies are plotted relative to the energy at (y=-0.7, z=3.25).

The CH bond which is being broken lies along the z axis at y=0, and the surrounding surface carbons lie behind the potential shown in fig. D.1, at $z < 2.4$ Å. The axis of the potential-energy saddle lies along the z axis, and therefore, incident H atoms with velocities along the z axis require the least increase in energy to reach the barrier. In contrast, H atoms with velocities along [100] (55° to the z axis), and impact parameters with $z \leq 2.8$ Å, must surmount the sides of the saddle to reach the transition state. Therefore, the reaction cross-section is likely to be greater for incident velocities along [111] than for velocities along [100], allowing for a difference between UHV measurements of reaction rate on the (100) and (111) surfaces.

X	Y	Z	CAS-GVB Energy
0.000000	0.000000	2.548904	-157.6745924933
0.000000	0.100000	2.548904	-157.6744589664
0.000000	-0.100000	2.548904	-157.6744596675
0.000000	0.200000	2.548904	-157.6740622211
0.000000	-0.200000	2.548904	-157.6740677456
0.000000	0.300000	2.548904	-157.6734249359
0.000000	0.500000	2.548904	-157.6717219386
0.000000	0.700000	2.548904	-157.6703469720
0.000000	-0.700000	2.548904	-157.6705266513
0.000000	0.000000	2.648904	-157.6741381841
0.000000	0.100000	2.648904	-157.6740209914
0.000000	-0.100000	2.648904	-157.6740214853
0.000000	0.200000	2.648904	-157.6736853620
0.000000	-0.200000	2.648904	-157.6736892235
0.000000	0.300000	2.648904	-157.6731811622
0.000000	0.500000	2.648904	-157.6720266869
0.000000	-0.500000	2.648904	-157.6720790470
0.000000	0.700000	2.648904	-157.6714252572
0.000000	-0.700000	2.648904	-157.6715487308
0.000000	0.000000	2.748904	-157.6735438862
0.000000	0.100000	2.748904	-157.6734736709
0.000000	-0.100000	2.748904	-157.6734740047
0.000000	0.200000	2.748904	-157.6732787122
0.000000	-0.200000	2.748904	-157.6732813511
0.000000	0.300000	2.748904	-157.6730049823
0.000000	-0.300000	2.748904	-157.6730135780
0.000000	0.500000	2.748904	-157.6725120326
0.000000	-0.500000	2.748904	-157.6725477137
0.000000	0.700000	2.748904	-157.6725920540
0.000000	0.000000	2.848904	-157.6734484000
0.000000	0.100000	2.848904	-157.6734245955
0.000000	-0.100000	2.848904	-157.6734248133
0.000000	0.200000	2.848904	-157.6733642455
0.000000	-0.200000	2.848904	-157.6733660187
0.000000	0.300000	2.848904	-157.6732988188
0.000000	-0.300000	2.848904	-157.6733046089

X	Y	Z	CAS-GVB Energy
0.000000	0.500000	2.848904	-157.6733361453
0.000000	-0.500000	2.848904	-157.6733601972
0.000000	0.700000	2.848904	-157.6738652318
0.000000	0.000000	3.048904	-157.6749364064
0.000000	0.100000	3.048904	-157.6749616189
0.000000	-0.100000	3.048904	-157.6749617154
0.000000	0.200000	3.048904	-157.6750396615
0.000000	-0.200000	3.048904	-157.6750404369
0.000000	0.300000	3.048904	-157.6751771024
0.000000	-0.300000	3.048904	-157.6751796428
0.000000	0.500000	3.048904	-157.6756608970
0.000000	-0.500000	3.048904	-157.6756715862
0.000000	0.700000	3.048904	-157.6764379998
0.000000	-0.700000	3.048904	-157.6764637238
0.000000	0.000000	3.248904	-157.6772756745
0.000000	0.100000	3.248904	-157.6773047747
0.000000	-0.100000	3.248904	-157.6773048280
0.000000	0.200000	3.248904	-157.6773916833
0.000000	-0.200000	3.248904	-157.6773920175
0.000000	0.300000	3.248904	-157.6775350743
0.000000	-0.300000	3.248904	-157.6775361464
0.000000	0.500000	3.248904	-157.6779791101
0.000000	-0.500000	3.248904	-157.6779836436
0.000000	0.700000	3.248904	-157.6785929685
0.000000	-0.700000	3.248904	-157.6786040453

Table D.1: Calculated CAS-GVB energies as a function of attacking hydrogen position (x, y, z). Coordinates are in Å; energies are in hartrees.

Bibliography

[1] M. Page and D. W. Brenner, "Hydrogen abstraction from a diamond surface. Ab initio quantum chemical study with constrained isobutane as a model." J. Am. Chem. Soc. **113**, 3270–3274 (1991).

[2] X. Y. Chang, M. Perry, J. Peploski, D. L. Thompson and L. M. Raff, "Theoretical studies of hydrogen-abstraction reactions from diamond and diamond-like surfaces." J. Chem. Phys. **99**, 4748–4758 (1993).